Single-atom catalysts: promotors of highly sensitive and selective sensors

Zehui Li, [ID]†*[abc] Enze Tian, [ID]†[de] Shunli Wang,[f] Meiyin Ye,[f] Shujing Li,[f] Ziyi Wang,[g] Zizhen Ma,[f] Guangya Jiang,[h] Cheng Tang, [ID][i] Kaihui Liu [ID][ad] and Jingkun Jiang [ID]*[b]

Sensors, the underlying technology that supports the Internet of Things, are undergoing multi-disciplinary integration development to constantly improve the efficiency of human production and life. Simultaneously, the application scenarios in emerging fields such as medical diagnosis, environmental monitoring and industrial safety put forward higher requirements for sensing capabilities. Over the last decade, single-atom catalysts (SACs) have attracted tremendous attention in fields such as environment and energy due to their high atom utilization efficiencies, controllable active sites, tailorable coordination environments and structural/chemical stability. These extraordinary characteristics extend the sensitivity and selectivity of sensors beyond their current limitations. Here, we start with the working principles of SAC-based sensors, and summarize the relationship between sensor performance and intrinsic properties of SACs, followed by an overview of the design strategy development. We then review the recent advances in SAC-based sensors in different fields and highlight the future opportunities and challenges in their exciting applications.

1 Introduction

The development of the Internet of Things (IoT) by Kevin Ashton since 1999 has been considered promising by all technological communities and scientific experts.[1] As the foundation of the IoT, sensors have provided significant benefits for studying the environment, climate, human health, food, and water. For instance, medical diagnosis of body health can be carried out using flexible and wearable sensors that can sense breath or subcutaneous tissue;[2] industrial safety and

environmental monitoring systems can be established using gas or water-quality sensors;[3] food freshness and safety can be instantly determined using paper-based sensors.[4] Despite sensors having played significant roles in a variety of scenarios, their sensitivity, selectivity, stability and reliability are still insufficient for expanding demands.[5] For instance, it is difficult for sensors to detect trace analytes with ppb-level or lower concentration and distinguish between two compounds that have similar sensing mechanisms (e.g., methanol from ethanol).[6] Therefore, it is necessary to develop sensors with high sensitivity, strong selectivity, superb reliability and great stability.

One of the most effective approaches is to optimize sensing materials/catalysts. Noble metals (Pt, Pd, Ir, etc.) and metal oxide (ZnO, WO_3, Co_3O_4, etc.) particles are commercial catalysts due to their unoccupied d-electron orbitals.[7,8] However, unsaturated coordination atoms on the surface of particulate catalysts are limited, resulting in low utilization of active sites.[9,10] Reducing the size of metal nanoparticles is considered to be an effective way to increase the number of catalytically exposed atoms, and this naturally changes the surface atomic structure, electronic configuration and surface defects.[11] These changes may have advantageous geometric and electronic effects on the coordination environments, enhancing the catalysts' activity. The most typical example is single-atom catalysts (SACs), in which the active metal sites are isolated on the support or stabilized by coordinated non-metallic atoms, resulting in

[a] State Key Laboratory for Mesoscopic Physics, Frontiers Science Center for Nano-optoelectronics, School of Physics, Peking University, Beijing 100091, China.
E-mail: zehuili@pku.edu.cn
[b] State Key Joint Laboratory of Environment Simulation and Pollution Control, School of Environment, Tsinghua University, Beijing 100084, China.
E-mail: jiangjk@tsinghua.edu.cn
[c] School of Environmental Science and Engineering, Shanghai Jiao Tong University, Shanghai 200240, China
[d] Songshan Lake Materials Laboratory, Dongguan 523808, China
[e] Institute of Physics, Chinese Academy of Sciences, Beijing, 100190, China
[f] School of Environmental and Municipal Engineering, Qingdao University of Technology, Qingdao 266555, China
[g] TC Air Technology Limited Company, Beijing 100084, China
[h] Leiden Institute of Chemistry, Leiden University, Einsteinweg 55, 2333CC Leiden, The Netherlands
[i] Beijing Key Laboratory of Green Chemical Reaction Engineering and Technology, Department of Chemical Engineering, Tsinghua University, Beijing 100084, China
† These authors contributed equally to this work.

maximized atom utilization efficiency and catalytic activity.[12–14] In 2011, Zhang and colleagues first proposed the conception of SACs and presented isolated Pt single atoms (SAs) supported on the surface of iron oxide nanocrystallites as a catalyst in CO oxidation processes.[15,16] Subsequently, thousands of SACs have been developed and identified through synthetic methods such as thermal migration induced by high temperature, atomic layer deposition (ALD), and space confinement effects.[17–19] With the progress of precision instruments and detection methods, the electronic and structural properties of SACs are further confirmed by advanced characterization techniques such as scanning transmission electron microscopy (STEM), scanning tunneling electron microscopy (STM), Fourier transform infrared (FT-IR) and X-ray absorption spectroscopy (XAS).[20–22]

SACs have been confirmed to significantly improve the catalytic activity and selectivity in electrocatalysis, thermal

catalysis, photocatalysis, enzyme catalysis, *etc.*[23] Based on these working principles, various sensing methods have been developed, including electrochemical, chemiresistive, colourimetric and luminescence methods. Compared to the catalysts made of nanoparticles, nanoclusters and bulks, SACs have the following advantages. (1) Maximize the number of catalytic sites to improve sensitivity and significantly reduce the use of catalytic metals.[24,25] For instance, Pt SAs implanted porous Ag–LaFeO$_3$@ZnO core–shell spheres as sensing materials show 6.69 times higher sensitivity to methanol than those without Pt.[26] (2) SACs often exhibit unexpected stability and selectivity compared to noble metal particle catalysts due to their tailorable coordination environments.[27] For example, SACs with NiN$_4$ coordination environments exhibit highly stable and selective H$_2$S sensing in the living mouse brain, demonstrating considerable practical utility and application prospects.[28] (3) Well-defined coordination environments for mechanism studies.[29] Although the development of SACs for sensing is still in its early stage, dramatically growing efforts have been made since 2016 and it has enormous potential (Fig. 1a).

This review comprehensively demonstrates the advanced applications of SACs in atmospheric, aquatic and biological sensing *via* thermo/electric/photocatalysis (Fig. 1b). We begin with a concise and comprehensive introduction to the working mechanism of SAC-based sensors, followed by the investigation of influencing factors of SACs for sensing. Then application-oriented synthesis strategies of SACs, including high single-atom (SA) loading, universal synthesis and large-scale preparation, are introduced. After that, diverse emerging sensing applications of SACs in atmospheric, aquatic and biological sensors are summarized. Finally, the challenges of SACs are discussed for the prospective high-sensitivity and -selectivity sensing applications. This review will provide better knowledge of synthesis methods, sensing mechanisms and applications of SAC-based sensors, further exploring the activity

Zehui Li is currently an Assistant Professor at Shanghai Jiao Tong University. He received his PhD degree from Tsinghua University (2020) under the supervision of Prof. Jingkun Jiang and Prof. Ning Duan. Then he worked as a postdoctoral fellow (2020–2023) and Research Associate Professor (2022–2023) in Prof. Kaihui Liu's group at Peking University. His research focuses on manufacturing and modulation of atomic materials and their applications in environmental sensing and catalysis. He is also promoting the industrialization of sensors and building sensor networks for tracing the source of atmospheric pollutants.

Zehui Li

Enze Tian is currently a postdoctoral fellow in Prof. Kaihui Liu's group at the Songshan Lake Materials Laboratory, and the Institute of Physics, Chinese Academy of Sciences (IOPCAS). She received her PhD degree in 2021 from Tsinghua University under the supervision of Prof. Jinhan Mo. She was a joint PhD student at the Department of Nuclear Science and Engineering at Massachusetts Institute of Technology (MIT) under the supervision of Prof. Ju Li. Her research focuses on air quality and energy conservation in built environments, aiming to detect and remove airborne pollutants with minimal energy cost.

Enze Tian

Jingkun Jiang is currently a Professor and the Deputy Dean at the School of Environment, Tsinghua University. Dr Jiang received his PhD from Washington University in St. Louis and then worked as a postdoctoral research associate at the University of Minnesota. His research interests encompass science and technologies in environmental monitoring and aerosol fields, with a specific focus on measurement of atmospheric aerosols and gaseous pollutants via sensors, electrical mobility technologies, and mass spectrometry.
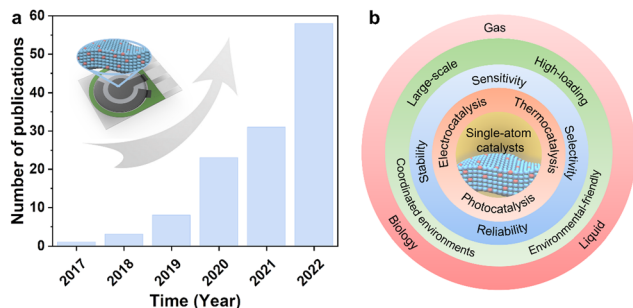
Jingkun Jiang

Fig. 1 (a) Number of yearly publications about SAC-based sensors. Updated until December 31, 2022. (b) Schematic illustration of SAC-based sensing.

origin, and exposing the reaction pathways of the target sensing substance.

2 Methods and mechanisms of SAC-based sensing

SACs with maximum atomic utilization and unique electronic structures provide strong interactions with analytes, which is essential for the effectiveness of sensing signals.[30] To date, SACs have been extensively studied in electrocatalysis, thermal catalysis and photocatalysis.[23] Based on these principles, various sensing methods have been developed, including electrochemical, chemiresistive, colourimetric, luminescence methods, and others. Hundreds of SACs for sensing have been explored utilizing these methods (Fig. 2).

2.1 Electrochemical SAC-based sensing

Electrochemical SAC-based sensing is one of the most widely used technologies due to its simplicity and low cost.[31] An electrochemical sensor is an extension of the electrochemical cell system, which is usually composed of two electrodes (working electrode and counter electrode) or three electrodes (working electrode, counter electrode and reference electrode).[32] Electrochemical sensing techniques can be divided into potentiometry, conductivity, impedance and amperometry/voltammetry. In practical applications, the amperometry/voltammetry method (current-based Faraday sensing) is quite acceptable.[33] Chemical signals from
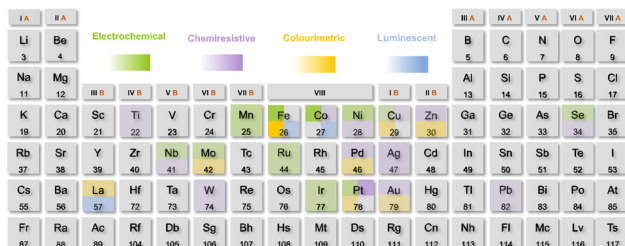

Fig. 2 Reported SACs for sensing to date. Different colours represent various sensing methods and the depth of colours corresponds to the number of reports.
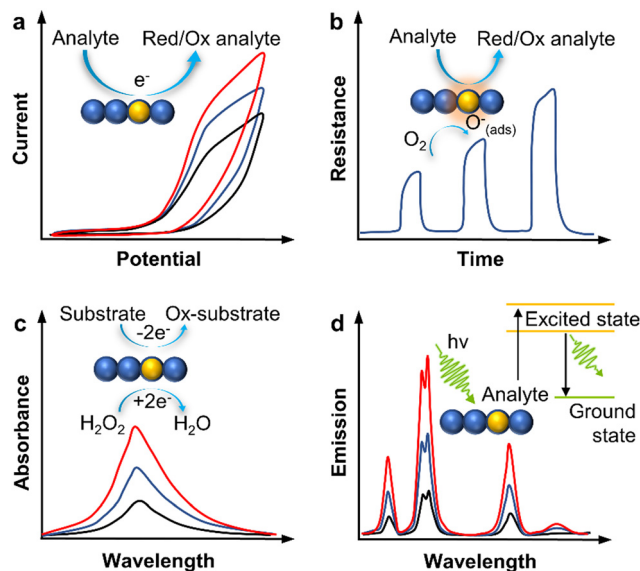

Fig. 3 Mechanism and typical sensing data of (a) electrochemical, (b) chemiresistive, (c) colourimetric and (d) luminescent SAC-based sensors.

electrocatalytic redox reactions on the surface of SACs (working electrodes) can be converted into qualitative or quantitative data signals *via* electrochemical sensing (Fig. 3a).[34]

The moieties of SACs (*e.g.*, metal-N_x) can be applied as a redox mediator to amplify the signals and regulate the reaction pathways.[35] One advantage is the coordination between SAs and substrates. For example, Au SAs have a strong interaction with CeO_2 with a higher density of vacancies. Au SAs introduce more oxygen vacancies for the adsorption and reaction of analytes such as H_2O_2, resulting in a faster electron transfer rate and larger electrochemical active surface area for H_2O_2 sensing.[36] Another advantage is affecting the electrocatalytic reaction energy barrier to control the reaction. Mao's group constructed a NO electrochemical sensor with Ni SAs anchored on N-doped hollow carbon spheres.[37] The Gibbs free energy required by Ni SACs to activate NO is greatly reduced. This can be attributed to the occupation of 3d and 4p orbitals of Ni atoms (electronic configuration of $3d^84s^2$) by the four ligands.

The electrochemical SAC-based sensors have selective oxidation or reduction reactions of the target analytes due to tailorable coordination environments.[38] For example, N-doped carbon decorated with Fe single sites exhibits an excellent sensing performance for Hg^{2+}.[39] The N atom on Fe–N–C can specifically recognize Hg^{2+} through chelation between Hg^{2+} and N atoms, while the SAs act as a signal amplifier.

2.2 Chemiresistive SAC-based sensing

Chemiresistive sensors with relatively simple configurations have been widely explored in gas sensing.[40,41] Different from electrochemical sensors, the typical chemiresistive sensor device consists of only a couple of interdigitated electrodes and semiconductor metal oxide (SMO) materials without electrolyte and reference electrodes. The resistance or direct

current of the sensors is usually measured by galvanostatic or constant biasing voltage (*i.e.*, conductometry) methods.

The mechanism of a chemiresistive SAC-based sensor is an electron/hole/resistance-induced signal change *via* physical/chemical adsorption/desorption of analytes of the SACs (Fig. 3b).[42,43] The suitable conductivity is needed due to the ohmic behaviour of the chemiresistive sensor. Otherwise, no measurable current or voltage drop will occur in the sensor.[44] For instance, Pd SAs on TiO_2 show p-type nature, and active oxygen species (*e.g.*, O^{2-}) are produced from adsorbed oxygen, resulting in a high conductivity state.[45] When reductive analyte CO molecules are adsorbed onto SACs, they are oxidized and release free electrons into p-type SACs to deplete their hole carriers, resulting in their low conductivity state. After gaseous CO_2 molecules are removed, oxygen molecules readsorb onto SACs and restore their high conductivity state.

Traditional SMO-based (*e.g.*, ZnO, TiO_2 and WO_3) gas sensors with wide band gaps usually have high operating temperatures ($\sim$200–400 °C), which increase energy consumption and limit their application. SACs have advantages in chemiresistive sensing owing to abundant active sites and outstanding oxygen adsorption energy, which can improve the catalytic spillover effect,[46,47] and thus improve the sensitivity and selectivity while decreasing operating temperature (<100 °C or even room temperature). In addition, the substrates of SACs are usually porous and regular structures with high specific surface areas (SSAs), which can provide a transmission channel for molecules/ions and improve the adsorption capacity to broaden the range of resistance.

2.3 Colourimetric SAC-based sensing

Colour perception is one of the first abilities that humans acquired. We learn to discern different tones and colour intensities from a young age. In 1838, W. A. Lampadius reported the first quantitative colourimetric determination to compare and quantify the percentages of nickel and iron in cobalt-ore. Then in 1853, Müller proposed a quantitative colourimetric analytical optical device. Over the last two decades, the popularity of miniaturization concepts, such as paper analysis equipment and image capture instruments, has increased the use of colourimetric devices and the demand for qualitative analysis of a wide range of analytes.[48] The working principle of colourimetric biosensing is detecting the colour changes caused by chromogenic substrates (Fig. 3c).[49] According to the Michaelis–Menten model and ping-pong mechanism, chromogenic substrates such as 3,3′,5,5′-tetramethylbenzidine (TMB) and 2,2′-azino-bis(3-ethylbenzothiazoline-6-sulfonic acid (ABTS) can be oxidized to dark colours such as blue and green in the presence of oxidants (H_2O_2 or O_2) produced by the enzyme.[50]

Compared with expensive and delicate natural enzymes, nanozymes have the advantages of low price, easy mass production and high stability (excellent resistance to extreme conditions such as high temperature, acid, alkali and organic solvents).[51] Since the peroxidase activity of Fe_3O_4 nanoparticles was reported in 2007,[52] hundreds of nanomaterials with similar

enzyme activity have been developed.[53,54] However, due to crystalline nanostructures and various surface configurations, conventional nanozymes usually exhibit low activity and poor stability.[55] To regulate and control the biocatalytic sites of nanozymes, SACs were applied as nanozymes (also called single-atom nanozymes, SAzymes). The isolated metal atoms are firmly anchored in the framework of the support, and the strong interaction between the metal and the support confers superior stability to SACs compared to other enzymes.[56] As a result, SACs are regarded as ideal nanozymes since they avoid several of nanozyme's intrinsic limitations, such as limited activity. For instance, Pd SACs have significantly higher catalytic efficiency than horseradish peroxidase, with a catalytic rate constant and catalytic efficiency values that are more than 625 and 4837 times higher, respectively.[57]

2.4. Luminescent SAC-based sensing

SACs as nanozymes have attracted great attention in the fields of biosensors, biomedicine and medical diagnosis. In addition to colourimetric sensing, SACs have also showed an advantage in luminescence sensing due to their higher sensitivity, low cost and easy operation.[58] Bioluminescence sensing and imaging is an effective method for clinical disease diagnosis, especially for early diagnosis of cancer.[59] Until now, various luminophores (quantum dots, conjugated polymers, rare-earth-doped upconversion nanoparticles, metal–organic frameworks, carbon dots and metal nanoclusters) have been reported for luminescent sensing.[60] The biggest advantage of SACs over other luminophores is their ability to have tunable sites and tailorable coordination environments.

The working principle of SAC-based luminescent sensing involves exciting luminophores by absorbing energy to generate in-band transitions (sp $\leftarrow$ sp) and interband transitions (sp $\leftarrow$ d) of electrons that emit characteristic luminescence (Fig. 3d).[61] Specifically, the luminescence mechanisms of various SACs can be divided into the luminescence of metal SAs, the luminescence of coordination environments, and the luminescence of electron transfer. For luminescent metal SAs, rare-earth materials like lanthanide (Ln) SACs exhibit distinctive properties resulting from lanthanide ion 4f–4f transitions, such as large Stokes shifts, long decay times, and high luminescence efficiency with narrow emission bands.[62] The optical emissions properties of Eu SAs are due to the $^5D_0 \rightarrow {}^7F_J$ transitions (J = 0–4). With moderate adsorption energies, these emissions are quenched after 10 seconds of exposure to volatile organic compounds such as acetone and cyclohexane, indicating their high luminescence sensing performance. In luminescence of coordination environments, the ligand absorbs photons, causing the electron to transition from the ground state S_0 to the singlet excited state S_1 or the triplet state T_1, and then the energy is released in the form of fluorescence or phosphorescence during the electron transition back to the ground state S_0.[63,64] For the luminescence of electron transfer, luminol has received a lot of attention due to its high emission quantum yield, low toxicity, and oxidation potential. In a luminol-based luminescence system, SACs can efficiently catalyse hydrogen

peroxide (H_2O_2) to generate reactive oxygen species (ROS) to promote luminol oxidation, thereby enhancing the luminescence signal and improving sensing sensitivity.[65]

2.5 Other SAC-based sensing methods

In addition to the single principle of the SACs-based sensing method, a variety of complex methods, such as photochemistry and electrochemiluminescence (ECL), have also been developed and showed potential in various fields such as clinical diagnosis, environmental investigation, forensic medicine and drug analysis.

Photochemical sensing technology involves the conversion of photons into electrical signals due to the excitation of electrons in photoactive materials caused by photon absorption. The excitation of light leads to the transfer and separation of charges, resulting in photocurrent.[66] SA injection can significantly alter the electronic and energy band structure of the catalysts for photochemical reactions, improving optical adsorption, separation, and transfer of optical catalysts, increasing the density of charge carriers moving around the Fermi level, and thus improving the photochemical activity. Simultaneously, numerous photocatalytic reactions have demonstrated that SACs frequently exhibit excellent stability and long life. Furthermore, the synergistic effect of unsaturated SAs promotes reactant adsorption and activation.[67] Zhang *et al.* took advantage of Co SACs by anchoring Co(II) SAs on graphitic carbon nitride (g-C_3N_4).[68] Using the confinement effect of SAs and substrates, the Co(II) sites can be distributed uniformly and atomically on the surface of g-C_3N_4. As a result, these Co SACs exhibit remarkable photochemical CO_2-to-CO conversion catalytic performance, with CO evolution rates as high as 464.1 μmol g^{-1} h^{-1}, which is 3 and 222 times higher than when bulky Co in metal organic frameworks (MOFs) and $CoCl_2$ are utilized as cobalt sources, respectively.

ECL combines the advantage of electrochemical and luminescence sensing.[65] The mechanism is that O_2 molecules adsorbed on the active sites of luminophores are catalytically reduced to reactive oxygen or luminol species *via* an oxidation–reduction reaction. The colour change induced by the generation of radicals, therefore, enhances the emission of light to facilitate the detection of analytes. SACs as luminophores can improve the signal of the luminol–O_2 system.[69] For example, Fe–N–C SACs with FeN_4 coordination environments can efficiently produce reactive oxygen species from dissolved oxygen, which subsequently engage in a reaction with the luminol anion radical, considerably enhancing the luminol ECL emission and realizing the linear detection of Trolox from 0.8 μM to 1.0 mM.

Although great progress has been made in understanding SAC-based sensing methods and principles, there are still challenges to be solved in the practical applications. For instance, the electronic properties and catalytic performance of a single metal atom largely depend on the metal carrier interaction, so it is a challenge for SACs to precisely construct active sites on the nano- or sub-nano-scale by regulating the coordination environments. Therefore, it is necessary to deeply study the preparation methods, the relationships between

structure and performance, the regulation strategies and the device development of SACs.

3 Relationship between sensor performance and intrinsic properties of SACs

It is expected that SACs will provide the next-generation sensors with high performance (known as 3S: high sensitivity, strong selectivity and superb stability).[70] To satisfy the 3S requirement, it is critical to thoroughly grasp the internal relationship between sensor performance and SAC intrinsic properties (metal SA species, loading amount and coordination environments of SACs). Based on the discussion of the sensing mechanisms of various types of SAC-based sensors in the previous section, the main rules for analyte sensing on the surface of SACs can be concluded as follows: (1) analytes are transported to the surface of SACs through mesopores or macropores on the substrates; (2) analytes undergo selective adsorption or catalytic process on the SA surface or its coordination environments, or indirectly through cascade reaction; (3) photons or electrons are transferred from the SA sites or substrates and accepted by the receivers, whose concentrations are related to the analytes. These physical/chemical/biological signals are amplified due to the 100% atom utilization of SACs. As a result, in this section, we will explore the implications of intrinsic properties of SACs under 3S requirements, paving the way for the development of SACs for sensing applications.

3.1 Sensitivity

In principle, an ideal SAC-based sensor should be quite sensitive, which usually also owns a low limit of detection (LOD) and an extended linear range. The classical interpretation explains that sensitivity is the slope of a curve representing a change in an electrically measured parameter (resistance or voltage) *vs.* analyte concentration. This indicates that the sensitivity of a sensor reflects how much does the sensor's output varies as the detected amount of analyte concentration changes.[71]

Compared to bulk catalysts, SACs with the discrete quantum states of the metal SAs, coordination environments, high surface-to-bulk ratio and strong metal–support interactions possess high specific/mass activity, making them naturally advantageous in terms of sensitivity. Guo *et al.* compared the photocatalytic performance of Pd nanoparticles and Pd SAs on TiO_2 (PdNPs/TiO_2 and PdSA/TiO_2) with a similar loading amount. PdSA/TiO_2 exhibited *ca.* five-fold photocatalytic activity (10 mol g^{-1} h^{-1}) for hydrogen evolution reactions compared to PdNPs/TiO_2, allowing for competitive chlorpyrifos photocatalytic sensitivity with a LOD of only 0.01 ng mL^{-1}. This is remarkably lower than the maximum residual limit (10 ppb) authorized by the United States Environmental Protection Agency (EPA).[72] Similarly, the sensitivity of the Co SAC (11.44 μA ppb^{-1}) for electrochemical sensing of As(III) is 8 times higher than that of Co NPs and 54 times higher than that of N–C (Fig. 4a).[73] The lower As 3d X-ray photoelectron
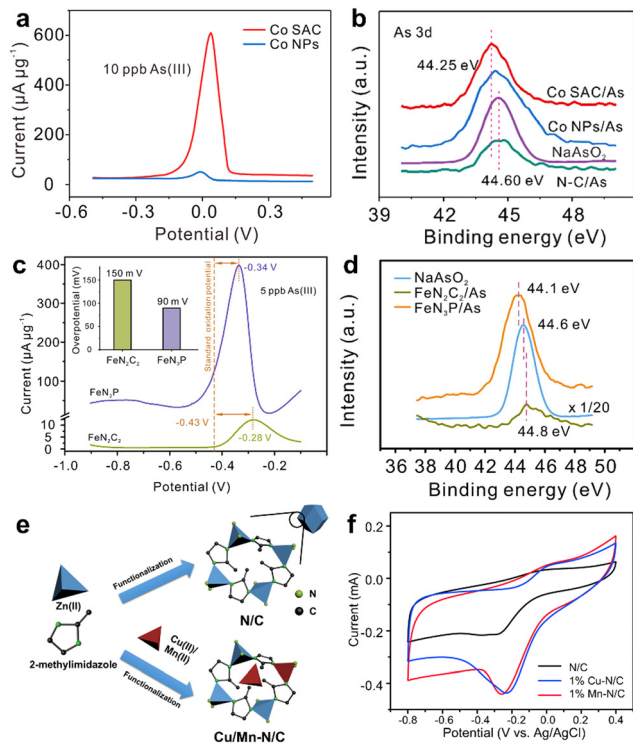
Fig. 4 (a) Square wave anodic stripping voltammetry (SWASV) response signals of the Co SAC and Co NPs to 10 ppb As(III). (b) As 3d XPS spectra of Co SAC/As, Co NPs/As, N–C/As and NaAsO$_2$. Reproduced from ref. 76 with permission from American Chemical Society, copyright 2020. (c) SWASV curves of FeN$_2$C$_2$ and FeN$_3$P to 5 ppb As(III). (d) As 3d XPS spectra of FeN$_2$C$_2$/As, FeN$_3$P/As and NaAsO$_2$. Reproduced from ref. 77 with permission from Elsevier B.V., copyright 2022. (e) Scheme of Cu, Mn atoms doped three-dimensional nitrogen-doped carbon frameworks. (f) Cyclic voltammetry (CV) curves of 1% Cu, Mn atoms doped and purified three-dimensional nitrogen-doped carbon frameworks. Reproduced from ref. 78 with permission from The Royal Society of Chemistry, copyright 2018.

spectroscopy (XPS) peak in Co SAC/As indicates a stronger interaction between Co SAC and H$_3$AsO$_3$ (Fig. 4b). Thus, the hybridization bond Co–O is the key to improving the sensitivity.

The active site density of SAs plays a key role in sensitivity. Koga revealed that 5 wt% loading amount of Pd SAs on Co$_3$O$_4$ NPs shows higher sensitivity ($\sim$85%) to 1000 ppm H$_2$ than 1 wt% and 3 wt% Pd SAs.[74] The regulation of the Pd SAs can affect electron transfer and amplify the electrical signal.[75] The content of SAs can be characterized using technologies such as thermo gravimetric analyzer, XPS, energy dispersive X-ray spectroscopy (EDS) and inductively coupled plasma-mass spectrometry, which is typically stated as a weight percentage (wt%) or atomic percentage (at%). The followings are the derivations and conversions between wt% and at%.

$$\text{at\% SAs} = \frac{(\text{Number of SAs})}{(\text{Total atomic number of the compound})} \times 100\%$$

$$= \frac{(\text{SA wt\%/SA atomic weight})}{\sum (\text{Each atomic wt\%/Each atomic weight})} \times 100\%$$

$$(1)$$

$$\text{wt\% SAs} = \frac{(\text{Mass weight of SAs})}{(\text{Total mass weight of the compound})} \times 100\%$$

$$= \frac{(\text{SA at\%} \times \text{SA atomic weight})}{\sum (\text{Each atomic at\%} \times \text{Each atomic weight})} \times 100\%$$

$$(2)$$

where wt% of SAs is the ratio of mass weight of the SAs to all atoms of the compound, whereas at% of SAs is the ratio of the number of SAs to all atoms of the compound.

The coordination environments of SACs also have a strong influence on sensitivity. The metal atoms and their surrounding coordination atoms (N, O, *etc.*) form catalytically active sites (also called coordination environments). The typical coordination environments of SACs include M–N$_x$ (M = iron, zinc, copper, nickel, *etc.*) ($x = \sim$2–5), similar to metalloproteinases. Huang and colleagues developed two kinds of Fe SACs with different coordination structures of FeN$_2$C$_2$ and FeN$_3$P. FeN$_3$P achieved a higher sensitivity (3.90 μA ppb^{-1}, 16 times higher than that of FeN$_2$C$_2$) toward As(III), completely avoiding Cu(II)-interference (Fig. 4c).[77] Compared with FeN$_2$C$_2$, Fe–P in FeN$_3$P has stronger affinity to O atoms and can break the As–O bond of H$_3$AsO$_3$, reducing the valence state of As(III). Here, the local chemical coordination environments (FeN$_3$P) also have a lower reaction energy barrier and faster reaction rate to reduce As(III), thereby enhancing the sensitivity to As(III) (Fig. 4d). Surface unsaturated atoms in low-coordination environments can contribute to the specific effective components of the catalytic process.[56] Cui and colleagues discovered that among Fe–N$_3$, Fe–N$_4$ and Fe–N$_5$, Fe–N$_3$ has the highest chemical reactivity towards the O$_2$ molecule, with an adsorption energy of 2.77 eV, indicating a high potential for the oxidase-like reaction.[79] Furthermore, among Ni–N$_3$, Co–N$_3$, Fe–N$_4$ and Fe–N$_3$, Fe–N$_3$ exhibited the highest oxidase-like activity and can be used as a viable colourimetric platform for glutathione detection.

The choice of substrate also has an influence on the sensitivity. Especially, the morphology, structure, conductivity and thermal stability are essential for heterogeneous catalysis.[80] One-dimensional (*e.g.*, nanorods, nanowires and nanotubes), two-dimensional (2D, *e.g.*, nanosheets, graphene, metal dichalcogenides) and three-dimensional (*e.g.*, MOFs, covalent organic frameworks, hydrogen-bonded organic frameworks and core–shell spheres) substrates have been developed for loading SAs to improve sensitivity. Wang's group loaded Pd SAs onto SnO$_2$ nanorods and SiC nanosheets to build a multi-heterojunction, which showed highly enhanced ppb-level ethanol gas sensing performance (much higher response than Pd NPs loaded on the same substrates).[81] One-dimensional SnO$_2$ nanorods have an adjustable band gap, while 2D SiC nanosheets have a large surface area, allowing for faster electron transfer and more sensing sites. Our group dispersed transition metal (Cu and Mn) atoms on ZIF-8 and carbonized as three-dimensional carbon frameworks (Fig. 4e).[78] When the loading amount of Cu and Mn was 1%, they showed enhanced current and lower resistance to H$_2$O$_2$ electrochemical reduction than 5% and 10% loading amounts (Fig. 4f). Further experiments proved that

partial metals are dispersed and embedded in three-dimensional frameworks through spatial confinement effects, while the other part forms metal–nitrogen binding states through strong coordination with nitrogen in organic ligands. As a result, three-dimensional frameworks can disperse SAs and have better electron/ion transfer capability with abundant defects and pores, improving sensitivity of H_2O_2 sensing.

Some unusual structures may also exhibit high sensitivity. Our group developed SACs with atomic Co–N_x–C sites anchored on a neuronal-like carbon support. Compared with Co SACs without neuronal-like carbon, these SACs showed higher sensitivity to H_2O_2 detection. Characterization revealed that the introduction of the carbon substrate can protect the loss of oxygen and nitrogen content, which is helpful for the formation of more Co–N_x–C sites. Wu and colleagues developed yolk–shell Pd_1@Fe_1 DACs with Fe_1 sites in an N-doped carbon shell and Pd_1 sites in a yolk.[82] To form the yolk, Zr_6-based UiO-66-NH$_2$ was chosen as the host to encapsulate $PdCl_2$ *via* the stable $PdCl_2$/NH$_2$ coordination configuration. To form the shell, an inert SiO_2 layer was coated on the yolk and the Fe–TiPP (TiPP, 5,10,15,20-tetra(4-(imidazol-1-yl)phenyl)porphyrindine) polymerization was subsequently conducted *via* a quaternization mechanism. The as-obtained $PdCl_2$/UiO-66-NH$_2$@SiO_2@Fe–TiPP was subjected to pyrolysis to reduce Pd and Fe cations into separate Pd_1 and Fe_1 sites. Finally, the SiO_2 template was removed using NaOH to yield a yolk–shell structural DACs. The DACs showed excellent conversion ($\geq$99%) and selectivity (85%) to the epoxidation reaction of styrene. Although various substrates can bring abundant pore structures, defects, and electronic structures to SACs, forming more abundant active sites and improving sensitivity, the relationship between structure of substrates and catalytic activity still needs to be further studied to provide guidance for SAC development in sensors.

Multi-atom catalysts (MACs) are another intriguing method that can boost intrinsic catalytic activity beyond SACs.[83] Compared to SACs, MACs with synergistic interaction of nearby metal atoms and tunable electronic environments can stimulate higher sensitivity. Our group developed a MAC with Co/Ni dual SAs. The CoNi MAC has higher catalytic activity for oxygen redox reactions than Co SACs and commercial Pt/C catalysts.[84] Fan and colleagues synthesized MACs with W–Mo dual SAs.[83] W–Mo dual atoms coordinate with oxygen atoms to form a W–O–Mo–O–C configuration, which has strong covalent interactions and enhanced intrinsic activity to hydrogen evolution reaction.

3.2 Selectivity and reliability

The accuracy of the sensor is reflected in two aspects: whether it can accurately measure analyte concentrations and whether it can selectively measure the target analyte in a changing and complex environment. As a result, selectivity (or anti-interference) is another important parameter to consider when evaluating the reliability of a sensor.

The adsorption–desorption intensity of analytes on SAs or substrates is important for selectivity because it is the initial stage in the sensing response. Mori *et al.* doped luminescent
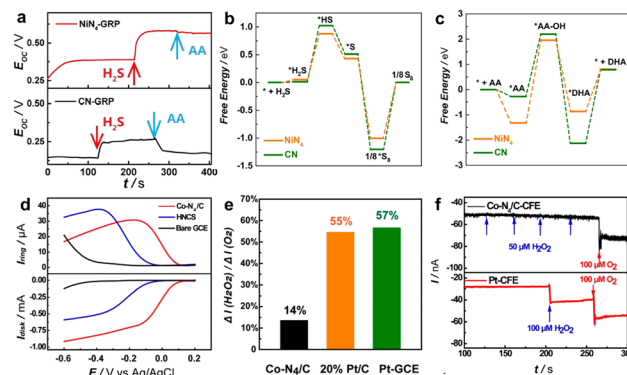

Fig. 5 (a) Response of NiN_4 SAC and CN substrates towards H_2S and AA. (b and c) DFT-calculated free energies of H_2S and AA oxidation steps on NiN_4 SACs and CN substrates. Reproduced from ref. 28 with permission from American Chemical Society, copyright 2022. (d) The rotating ring-disk electrode polarization curves of Co–N_4/C SACs, HNCS and bare glassy carbon electrode (GCE). (e) Current ratios of H_2O_2 to O_2 to quantitatively compare the H_2O_2 tolerance of Co–N_4/C SACs, Pt/C and Pt. (f) Amperometric response of H_2O_2 and O_2 at Co–N_4/C SACs and Pt. Reproduced from ref. 86 with permission from American Chemical Society, copyright 2020.

Eu^{3+} SAs into exfoliated g-C_3N_4 nanosheets for selective adsorption of acetone and cyclohexane.[85] Photoluminescence (PL) spectra exhibit Eu^{3+} emission characteristics due to the $^5D_0 \rightarrow {}^7F_J$ transitions (J = 0–4). These emissions are quenched within 10 s on exposure to acetone and cyclohexane instead of benzene due to moderate adsorption energies. Mao's group identified that NiN_4 SACs can promote electrocatalytic oxidation of H_2S at a very low potential.[28] When the electrode works under open-circuit conditions, the bias-free potentiometric sensing can decrease the sulfur deposition on the surface, improving stability and sensitivity, and it has anti-interference ability against other analytes such as ascorbic acid (AA) (Fig. 5a). Density functional theory (DFT) calculations reveal that the Ni–N_4 SACs need less energy at the rate-determining step ($H_2S^* \rightarrow SH^* + H + e^{+-}$) and the product desorption step ($1/8S_8^* \rightarrow 1/8S_8 + *$) compared to the nitrogen-doped carbon sphere (CN) substrate (Fig. 5b). Conversely, it takes higher energy at the first electron-transfer step ($AA^* + H_2O \rightarrow *AA–OH + H + e^{+-}$) of AA oxidation on Ni–$N_4$ SACs than the CN substrate (Fig. 5c).

Tailoring SA coordination environments can influence the reaction pathway, thereby improving reaction selectivity in addition to enhancing sensitivity. Mao and Li *et al.* reported a Co–N_4 SAC with highly selective O_2 sensing with improved response to H_2O_2 interference.[86] Electrochemical kinetic analysis and DFT calculations confirmed that Co–N_4 catalytic sites on hollow N-doped carbon spheres (HNCSs) dominantly promote the direct four-electron pathway of oxygen reduction reaction (ORR) rather than two sequential two-electron reduction pathways of H_2O_2 reduction reaction (Fig. 5d–f). In addition to the weak adsorption of H_2O_2 on the porphyrin-like Co centres, the coordination number also determines the catalytic performance. He's group synthesized a series of

Pt_1/N–C SACs by a ''precursor-atomization strategy'', and the coordination number of Pt–N was successfully controlled by changing the calcination atmosphere and times.[87] Catalytic tests reveal that decreasing the Pt–N coordination number (from $Pt–N_5$ to $Pt–N_3$) improves the catalytic performance by up to 550 times with highly selective hydrogenation of 3-nitrophenylacetylene, successfully breaking the selectivity–activity seesaw. Tang et al. prepared Mo SACs with different coordination numbers of S and O.[88] The introduction of S atoms can improve the adsorption of OOH* by Mo SAs, wherein $Mo–S_4–C$ and $Mo–O_3S–C$ have stronger $2e^-$ selectivity toward the oxygen reduction reaction than $Mo–O_4–C$.

Based on the different coordination environments, sensor arrays with diverse SACs and pattern recognition strategies bring a charming prospect for the detection and categorization of a wide range of volatile organic compounds (VOCs) in complicated situations. Ma and Ding et al. developed a sensor array by decorating a series of SA sites (Pt, Co, and Ru) on 2D supports (metallic graphene, n-type MoS_2, and p-type WSe_2) for selective VOC detection at room temperature.[89] Using the properties of adsorption heights, metal charge, and charge transfer between adsorbed VOCs and SA sites, the sensing data were trained to develop machine learning (ML) models for predicting adsorption energies and sensing performance.

3.3 Stability

Although SAs can improve sensor sensitivity and selectivity, stability is a significant barrier for SACs in practical applications. The aging of SAC-based sensors may have issues like zero drift and decreased responsiveness, resulting in low long-term stability and dependability. For example, Pt SAs tend to cluster in an H_2 atmosphere due to the gathering or poisoning of SACs. A particularly high SA density may lead to neighboring atoms clustering together, reducing long-term stability. Koga revealed that when the loading quantity of Pd SAs on Co_3O_4 NPs exceeds 5 wt%, Pd SAs form Pd oxide clusters, lowering the sensitivity.[74] Therefore, revealing the morphology change, electronic structure regulation and reaction pathway of SAs under reaction conditions is significant for designing catalysts with high stability.

Over the past decade, an increasing number of in situ/operando methods (the in situ TEM, XAS, Raman and FT-IR) have been conducted on SACs in various applications, including thermochemical, electrochemical, and photochemical reactions.[90] These methods allow tracking of the dynamic changes in the local solid geometry and electronic structure of the catalyst, which are key to reactions.[91] Li's group recorded the competing sintering and atomization processes from noble metal nanoparticles (Pd, Pt and Au) to thermally stable SAs (e.g., $Pd–N_4$) over 900 °C in an inert atmosphere by in situ environmental TEM.[92] This finding challenges the conventional understanding that noble metal SAs and ultrafine metal cluster catalysts tend to sinter into aggregated particles driven by the reduction of free energy on the metal surface at high temperatures.

Similarly, the in situ/operando characterization of SACs during the reaction process is beneficial to reveal the stability of SACs and understand the reaction mechanism. Liu and colleagues first evaluated the dynamic stability of Cu SAs using a constant-potential hybrid-solvation dynamic model.[93] Results showed that some Cu SAs on the surface of nitrogen-doped graphene can be reduced to Cu clusters by strong adsorption of hydrogen under the negative potential, which can promote the CO_2 reduction reaction. Simultaneously, Cu clusters can also return to the initial Cu SAs with hydrogen radicals when changing to the positive potential. Wang and colleagues observed that the as-synthesized $Cu–N_4$ SAs can be restructured to ∼5 nm nanoparticles during the electrochemical reduction of nitrate to ammonia by combining electron microscopy with operando XAS.[94] After electrochemical reduction, the Cu nanoparticles transform to $Cu–N_4$ SAs when exposed to an ambient atmosphere. During electrocatalytic processes, SAs play the role of active species or promoters, while restricted clusters/nanoparticles are occasionally the actual active sites. Huang and colleagues observed two intermediate structures of Ni SAs in different electrolytes by in situ XAS.[95] Ni SAs on MoS_2 reduce to Ni_0 species to be the active sites of the hydrogen evaluation reaction under acid conditions, and they undergo reconstruction to form NiS_xO_y species and reversibly formed Ni_0 as active sites under alkaline conditions. This demonstrates that Ni SAs are active species and promoters under varied conditions.

The interaction of SAs with substrates has a significant impact on stability. In theory, the embedded/inserted single atoms are stable on supports.[96] Both ionic bonding and covalent bonding are responsible for the strong interaction between SAs and the support, known as covalent metal–support interaction.[97] Our group doped Cr atoms into 2D Pd metallene (Cr-Pdene) with a few atomic layers for formaldehyde sensing via formaldehyde electrooxidation.[98] An in situ FT-IR spectroscopic analysis reveals that peak intensity of oxidation products CO_2 and the adsorption of CO intermediates (both bridged CO and threefold hollow CO) of formaldehyde on Cr-Pdene are higher than those without Cr atoms (Fig. 6). DFT calculation reveals that the d-band centre of Cr-Pdene downshifts of 0.08 eV relative to that without Cr atoms, suggesting that Cr atoms can successfully improve the electronic structure of Pd metallene and diminish the interaction between Pd and CO, providing an anti-poisoning approach to favour CO_2 generation and suppress CO adsorption. As a result, the sensor has a strong anti-CO poisoning capability.

The SACs with multi-metal atoms can not only optimize the activity and selectivity but also the stability through tuning metal species. The strong chemical interactions between neighbouring atom–atom can efficiently stabilize the individual species and prevent agglomeration, thereby creating highly stable coordination environments. Huang's group fabricated a MAC with Fe/Bi dual SAs for cascade catalysis and peroxymonosulfate activation.[99] The introduction of Fe SAs can not only improve the activity of the SACs, but also expand the distance between neighbouring Bi SAs, preventing the agglomeration of atoms.
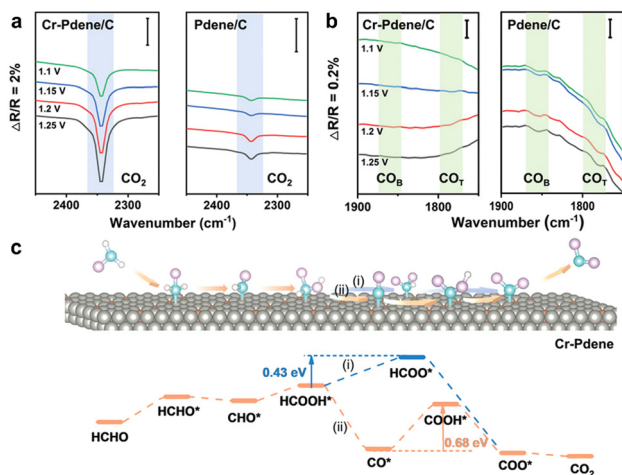
Fig. 6 (a) CO_2 and (b) bridged CO (CO_B) and threefold hollow CO (CO_T) signals on the surface of Cr-Pdene/C and Pdene/C. (c) Upper: schematics of two probable intermediate breakdown paths on the Cr-Pdene surface. Below: diagrams illustrating the intermediates for formaldehyde oxidation reaction's free-energy on the surface of Cr-Pdene. Reproduced from ref. 98 with permission from Wiley, copyright 2021.

4 Synthesis of SACs for sensing

To realize the full potential of SACs in various sensors, at least three basic problems need to be solved. (1) Instability: from the perspective of thermodynamics, the high surface free energies of single metal atoms make them prone to agglomeration to form clusters or nanoparticles. (2) Lack of universality: a single approach is often applied to prepare SACs with only one type of coordination environment. It is still a challenge to extend the synthetic method to the systems with rich SACs.[100] (3) Cost and batch processing technology problems: Precise and controllable synthesis technologies such as the atomic layer deposition method and mass-selected soft-landing method are often constrained by expensive experimental equipment and low output, making them challenging to apply in industry. Although the wet chemical approach is simple for batch manufacturing, it is usually suitable for creating low-loading SACs and has the disadvantages of being time-consuming, complicated and environmentally polluting. As a result, synthesizing SACs with high SA loading and various coordination environments is needed. In addition, large-scale and green preparation methods should also be considered in practical applications. In this section, we will discuss recent advances on intriguing synthetic strategies for SACs (Table 1).

4.1 Preparation of SACs with high-loading density

As the catalytic active centre of SACs is contributed by the immobilized unsaturated atoms, the atomic loading amount is an indispensable indicator of catalytic/sensing performance. Generally, the atom loading amount must be kept below a threshold concentration to avoid aggregation, which restricts the mass/volume activity of the SACs. Most of the prepared SACs have a profoundly low metal weight ratio (usually in the range of 0.5–3.0 wt%), and the SA loading obtained by ALD,

MSLL, CVD and other physical deposition methods is less than 5 wt%. The high surface energy of individual atoms will give rise to ubiquitous migration and aggregation of SAs to form nanoparticles at high-temperature during the synthesis process. Therefore, although dispersion and high-loading density of SAs are contradictory, it is critical to overcome the agglomeration effect of SACs in order to achieve a higher SA loading and thus improve sensor sensitivity.

A sophisticated synthesis strategy and substrate materials are the dominant factors affecting the SA loading. Generally, wet chemical synthesis and high-temperature pyrolysis strategies have the potential for large-scale applications in the preparation of highly metal-loaded SACs. It is expected that the isolated metal atoms are anchored with light element (such as heteroatom doped carbon) substrates through strong interactions such as coordination, electrostatic adsorption or ionic bonding, so that they can achieve higher SA loading compared to oxides. Zeng *et al.* used the strong affinity between Pt and S to coordinate adjacent Pt atoms on MoS_2 with abundant S atoms through metal–sulfur, so that the mass loading of uniformly dispersed Pt atoms was as high as 7.5 wt%.[101] During the synthesis, Pt atoms replace Mo atoms in MoS_2 nanosheets. The distance between the two nearest Pt SAs in Pt/MoS_2 is greater than 3 nm at low Pt loadings (<1 wt%). The distance will become smaller and some Pt SAs may become overlapped or adjacent. For 7.5 wt%, the content of isolated Pt SAs is 23.7% and that of neighbouring Pt SAs is 65.5%. Huang's group developed a salt template method to disperse isolated Co atoms on nitrogen-doped 2D carbon nanosheets through Co–N coordination bonds.[102] The site proportion of Co atoms is quite high (~15.3%). Hu's group developed a general cascade anchoring strategy for the mass production of a series of M-NC SACs with a metal loading up to 12.1 wt%.[103] Systematic investigation reveals that metal ions chelated by an oxygen-species-rich porous carbon support (*e.g.*, glucose), physical isolation of chelate complexes upon high loading, and binding with N-species (*e.g.*, melamine) at elevated temperatures (>600 °C) are all required for high-loading M-NC SACs.

Treating the substrate is an effective way to increase the SA loading amount, such as introducing defects, vacancies and doped heteroatoms to enhance the interaction between the carrier and metal atoms. Gu and colleagues developed a simple method to synthesize Ir SACs on NiO nanosheets.[104] The strategy involved facile immersion of the NiO-pretreated carbon cloth in an aqueous solution of Ir precursors, followed by heating, cooling and washing processes resulting in well-distributed Ir atoms on the NiO substrate. The content of Ir atoms can be tuned by adjusting the concentration of the precursor solution. Ir SAs are stably doped into NiO(001) with a loading amount of ~18 wt%. XPS and XAS showed that Ir^{4+} atoms are mainly dispersed on the surface of the NiO substrate and then formed a chemical bond with NiO, which improve the surface reactivity of NiO(001).

It has also been proven that heat-induced aggregation of SAs into nanoparticles can be prevented by gradually removing the ligand, thereby controlling the combination of metal

Table 1 Summary of principles, uniqueness, and respective advantages and disadvantages of different preparation strategies

Goals	Synthesis strategies	Active sites	Loading amount	Advantages	Disadvantages	Ref.
High-loading density	Wet-chemistry	Pt–S	7.5 wt%	Neighbouring Pt SAs collaborated to vary the reaction barriers	Small-scale preparation	101
	Salt template pyrolysis	Co–N	~15.3%	Large electrochemically active surface area		102
	Cascade-protection	M–N$_x$	12.1 wt%	Synthesis over 8 g, can be extended to Mn, Co, Ni, Cu, Mo, Pt SACs, etc.		103
	Defect engineering	Ir–O	~18 wt%	Loading amount can be controlled by chloroiridic acid ethanol solution		104
	Two-step annealing	Ni–N$_4$	23 wt%	Expandable to 15 SACs synthesis		105
	GQD-assisted synthesis	Ir–N$_4$	41.6 wt%	High nitrogen content of ~20 at%		106
Tailorable coordination environments	Sacrificial template	Ni–N$_x$–C	~0.9 wt%	Host–guest cooperative protection strategy	Experimental study	107
		Mn–N$_x$–C	0.36 and 0.42 wt%			108
	Electrochemical deposition	Ir–O/Cl	2.0 and 1.2 wt%	Can be extended to 34 SACs synthesis		109
	Seeding	Ni–N$_4$	2.8–7.9 wt%	Stable on 2D materials, rarely forming clusters or nanoparticles		110
	Controlled slow annealing process	Pt	2.12 wt%	Immobilized on a 2D substrate through non-covalent bonding		111
	Sacrificial template	Co/Ni–N	1.59 and 0.9 wt%	Abundant interaction between dual/triple atomic sites		84
		FeCoZn	0.5 wt%			112
Large-scale preparation	One-pot pyrolysis	Cu–N$_4$	0.32 wt%	Gram-scale (22.8 g)	Limited load amount	113
	Ligand-mediated	M–N	2.5 wt%	A scale of >1 kg, library of M-SACs (M = Ni, Mn, Fe, Co, Cr, Cu, Zn, Ru, Pt and combinations)		114
	Mechanochemistry (ball milling method)	Pd^0	0.25 wt%	From 10 g to 1.035 kg, can be extended to Rh, Ru and Pd$_1$/Cu		115
		Au^0	0.12 wt%	1.025 kg		116
Others	Ball-milling to form atomized metals	M–N–C	~1.10 wt%	Directly converts bulk metal into SAs without by-products and waste	Energy consumption	117
	Deposition	Fe–N$_4$O	0.745 wt %	Gaseous NH$_3$ and HCl condense into solid NH$_4$Cl and recycled downstream	Small-scale preparation	118
	3D printing	M–O$_4$	4.3–20.8 wt%	Coordination environment and geometric shape can be adjusted	Pyrolysis is required on a heatproof substrate	119
	Click chemistry	Co–N–C	1.71 wt%	No restrictions on molecular size or symmetry and high specificity	Specificity of the clicking reaction	120

precursors and carriers. Lu's group proposed a scalable strategy, including impregnation and two-step annealing to synthesize high-atomic-density SACs (Fig. 7a).[105] The method typically controls the ligand removal from precursors. The initial lower annealing temperature controls the maximal anchoring metal to coordination sites for high atomic coverage, while the higher temperature permits the complete removal of ligands and the transformation of metal precursors into SACs. In addition, the author achieved a standardized automatic control system for large-scale synthesis. The atomic platform enables accurate temperature control, metal addition and mixing of carriers and precursors. The routine can easily be used to obtain a series of SACs with up to 15 atomic species and the highest loading of 23 wt%, from the aspect of both high productivity per unit reactor and the atomic loading (Fig. 4b). During the SA loading process, metal atoms can use a carrier with surface functional groups to react with the deposited metal within the studied temperature range.

Recently, ultra-high density (5–15 atoms per square nanometer) SACs have attracted great attention due to their dense site synergy and corresponding electronic effect.[121,122] Wang's
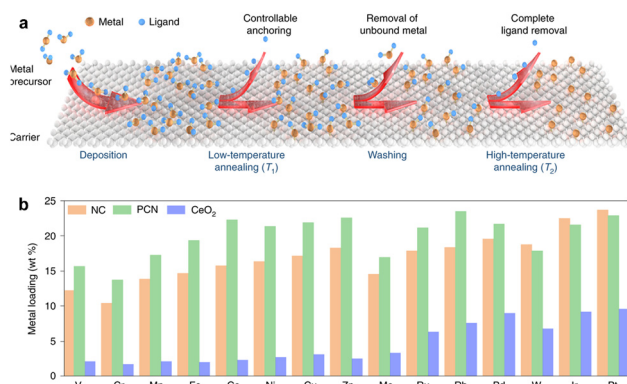

Fig. 7 (a) Preparation strategy of ultra-high-density SACs. (b) Metal loadings on nitrogen-doped carbon, polymeric carbon nitride and CeO$_2$ supports. Reproduced from ref. 105 with permission from Springer Nature, copyright 2021.

group proposed a synthesis method by freeze-drying interweaved graphene quantum dots (GQDs) as an aerogel substrate.[106] The result shows surprisingly high Ir loading up

to 41.6 wt% (3.84 at%) without aggregation. Aerogels with hierarchical pore structures as substrates can not only provide micropores for anchoring ultra-high-density SACs, but also supply mesopores and macropores for ion transport channels and structural supports, respectively. The strategy can also be applied for other widespread species like Pt and Ni with the loading of 32.3 wt% and 15 wt%, respectively. The highly isolated atomic pattern guarantees enough spacing between single atoms and prevents aggregation. Compared with top-down and bottom-up methods, the strategy employs high surface/volume ratio GQDs, which allows for an increase in surface functional groups and unsaturated coordination, therefore anchoring more isolated atoms through chelation and complexation effects. In addition, the GQD-modified support do not undergo structural transformation during pyrolysis due to its high thermal stability. This prevents the generation of atomic nanoparticles.

When the density of SAs increases, the distance between metal SAs will decrease. At ultra-high atomic densities (5–15 atoms nm^{-2}), the site distance may decrease to 0.2–0.5 nm or form neighboring atoms or dual atoms.[123] As a result, the key to forming SACs with high-loading density is to take advantage of a suitable substrate (such as specific surface area, defect/vacancy sites and structures) and build interactions between metal SAs and functional substrates (such as coordination type, anchor sites, bridging mode, and covalent bond interactions).[122] High density or nearby heterogeneous metal atoms not only improve catalytic activity, but also have a synergy between adjacent SAs to activate or adsorb special species in catalytic reactions that low-loading density SACs cannot realize.[124]

4.2 Preparation of SACs with tailorable coordination environments

Apart from the catalytic dynamics of isolated atoms, the interaction between atoms and the underlying supports (known as coordination environments) also impacts the activity, selectivity and stability of SACs. For instance, asymmetric tri-coordinated SACs ($Ni–N_3–C$) possess optimal adsorption energy and lower overpotential for the oxygen redox reaction than conventional tetra-coordinated ($Ni–N_4–C$).[125] During the synthesis of SACs, the abundant vacancy defects, trapping centres and unsaturated coordination sites on the surface of the support control the adsorption and reduction of metal precursors. Metal species are spatially distributed on the support and stabilized after post-treatments like high-temperature carbonization and acid washing to remove precursor ligands. Typically, SAs can be anchored by heteroatoms (such as N, O, S, and P) or defects on the substrates to form coordination environments such as $M–N_x$.

Although it is known that different coordination environments play different roles in catalytic process, it is still a challenge to synthesize SACs with various coordination environments. Jiang and colleagues designed a series of Ni SACs with different N coordination numbers ($Ni–N_x–C$, x = 2–4) by pyrolysis of MgNi-MOF-74 at different temperatures.[107] Han's
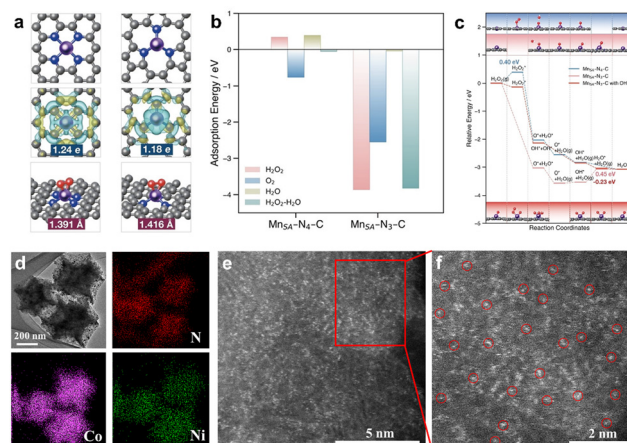

Fig. 8 (a) DFT-optimized structures, the corresponding charge density difference and Bader charges, and O–O bonding of adsorbed O_2 molecules of $Mn–N_4–C$ and $Mn–N_3–C$. (b) Adsorption energies of H_2O_2, O_2, and H_2O. (c) Free energy diagrams of peroxidase-like reaction. Reproduced from ref. 108 with permission from Wiley-VCHGmbH, copyright 2023. (d) Elemental mappings of Co/Ni dual site catalysts. (e and f) HAADF-STEM of Co/Ni dual site catalysts. Reproduced from ref. 84 with permission from Elsevier B. V., copyright 2018.

group constructed $Mn–N_3–C$ and $Mn–N_4–C$ by a host–guest approach at room temperature (Fig. 8a).[108] The $Mn–N_3–C$ complex shows higher oxidase-, peroxidase- and glutathione oxidase-like activities than $Mn–N_4–C$ (Fig. 8b and c). Furthermore, the $Mn–N_3–C$ based colorimetric sensor exhibits linear response to gallic acid (1.0–70 μM) and citric acid (0.2–15 μM).

More metal atoms and substrates need to be tried in order to controllably generate a diversified coordination environment. Zeng et al. developed a general electrochemical deposition method for preparing SACs.[109] Through electrochemical deposition in an electrochemical three-electrode system, Ir_1/$Co(OH)_2$ SACs with different valence states and coordination environments (mass loading of 2.0 and 1.2 wt%) are obtained through cathodic deposition and anodic deposition. This is due to different deposition species in the process of cathodic and anodic deposition by different redox reactions. By this method, 34 different SACs were prepared, containing 3d, 4d and 5d metals on cobalt hydroxide, molybdenum sulfide, manganese oxide and nitrogen-doped carbon substrates. It is worth noting that only when the loading amount of metal is lower than a certain limit SAs can be obtained. Otherwise, metal bonds will form between atoms such as Ir–Ir, forming metal clusters or particles.

2D materials with abundant exposed active sites as substrates have a much higher utilization efficiency for loading different metal SAs. Jiang and colleagues reported a seeding method for SAC production for a wide range of SAs (Ni, Co, Fe, Cu, Ag, Pd and dual atoms of Ni and Cu) on 2D materials (graphene, boron nitride, and MoS_2) with atom loading ranging from 2.8 wt% to 7.9 wt%.[110] This method can be used to form different coordination environments (e.g., M–N) by stabilizing SA dispersed carbon nitride (CN_x) on the modified 2D substrate with polyvinylpyrrolidone and poly(ethylene imine). Different

from traditional methods that rely on defects on the substrate surface to anchor SACs, the synergistic effect between the implanted SAs and the support substrates can be employed to form novel coordination environments. In addition to conventional 2D materials, Kim *et al.* proposed a general approach to prepare Pt SAs on inorganic nanosheets (metallic Pd, metal oxide: SnO_2, ZnO, and Co_3O_4, and perovskite: $LaCoO_3$) *via* sacrificial N-doped graphene (NG) template-assisted synthesis.[111] Among various substrates, Pt SAs on SnO_2 nanosheets (Pt SA loading of 2.12 wt%) with an inherent high SSA shows high response value (R_a/R_g = 95.4) for 10 ppm acetone sensing. Therefore, metal atoms are gradually and evenly immobilized on a 2D substrate through non-covalent bonding during the controlled slow annealing process. This represents a great potential for controlling produce SACs with diversified coordination environments.

When two or three SAs are relatively close, a synergistic coordination environment such as M_1–M_2 can be also formed. Dual-atom catalysts (DACs), as extended family members of SACs, have begun to emerge in recent years. Our group synthesized atomic Co/Ni dual sites in N-doped porous Janus-like carbon frameworks by coordinating ZIF-67 with Ni complexes (Fig. 8d).[84] Compared with single Co SACs, Ni–N bonds in Co/Ni DACs have been proven to increase the electronic activity of N atoms. Atomic Co/Ni dual sites can be observed in high-angle annular dark-field scanning transmission electron microscopy (HAADF-STEM, Fig. 8e and f). In addition to DACs, triple-atom catalysts (TACs) were also proposed. Chen's group developed FeCoZn TACs through a sacrificial ZIF template method.[112] The FeCoZn TACs can be used as a nanozyme-based colourimetric sensor array to identify seven preservatives in food. By introducing second/third metal sites to construct DACs/TACs, catalysts can have the advantages of abundant interaction between various atomic sites and substrates (synergy effect, spacing enhancement effect and electronic effect).[126]

4.3 Large-scale preparation of SACs

The effective sensing applications of SACs will be strongly dependent on the industrial-scale manufacturing of SACs with long-term homogenously dispersed metal SAs. However, applications based on SACs are limited by the fact that the productivity of most SACs is only up to the milligram or gram level. Active atoms easily move and aggregate during batch preparation, making it challenging to controllably ensure product quality. Strategies for large-scale synthesis of SACs will therefore be required for the industrialization of sensors.

A critical improvement method is to strengthen the interaction and the sufficient contact between SAs and the support surface. By minimizing the size of metal particles down to an atomic level, not only the relative density of active sites is increased, but also the surface free energy of particles leads to strong bonding with substrates, presenting reliable and highly catalytic SACs. Therefore, the synthesis of SACs needs to be precisely designed. However, previous precisely-controlled preparation methods such as atomic layer deposition have high costs but small outputs, which are difficult to scale up for

commercialization.[127] Yang *et al.* reported a scalable fabrication method that can generate gram-scale (22.8 g) SACs in one reactor.[113] It employs one-pot pyrolysis which involves a thorough mixing and stirring of carbonized chitosan and metal precursors under a N_2 atmosphere. Natural chitosan with rich N content acts as a defect-rich substrate and is capable of strongly anchoring Cu atoms. HAADF-STEM and X-ray absorption near-edge structure (XANES) measurements demonstrates that the Cu–N_4 sites instead of Cu nanoparticles, have a stable current density over 30 hours of CO_2 reduction.

High temperature triggers aggregation of isolated atoms, preventing high spatial uniformity and stable immobilization of atomic dispersion. A potential method is to reduce the kinetics and thermodynamic driving forces for the formation of metal nanoparticles by reducing the pyrolysis temperature (less than 800 °C). Zhan's group prepared a variety of M–SACs (M = Ni, Mn, Fe, Co, Cr, Cu, Zn, Ru, Pt and their combinations) using a "ligand-mediated" synthesis strategy (Fig. 9).[114] In this strategy, the modification of carbon black surfaces using metal complexes (*i.e.*, M^{2+} ions coordinated with 1,10-phenanthroline ligands) promotes the generation of "porphyrin-like" single metal sites, so as to closely bind metal cations and prevent metal atoms from aggregating into clusters or nanoparticles. In addition, the direct use of conductive carbon carriers eliminate the need of high pyrolysis temperatures that are significantly detrimental to SACs' stability (if carbon carriers derived from ZIF precursors, temperatures up to 900 °C are usually required to produce carbon materials with good conductivity). This universal strategy allows for large-scale production of SACs with a scale of >1 kg and high SA loading is highly promising for further expanding commercial production.
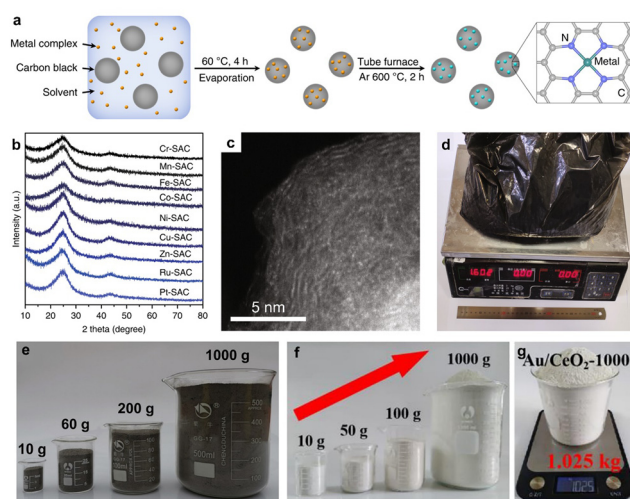
Fig. 9 (a) Schematic illustration of two-step SAC synthesis procedure. (b) XRD patterns for various SACs. (c) HAADF-STEM image and (d) photograph of the synthesized kg-scale Ni SACs with 2.5 wt% Ni loading amount. Reproduced from ref. 114 with permission from Springer Nature, copyright 2019. (e) Pictures of Pd_1/ZnO catalysts with different amounts. Reproduced from ref. 115 with permission from Springer Nature, copyright 2019. (f and g) Pictures of Au_1/CeO_2 catalysts with different amounts. Reproduced from ref. 116 with permission from Elsevier B.V., copyright 2020.

In addition to chemical synthesis, mechanochemistry (ball milling method) has attracted much attention because it can break and reconstruct chemical bonds of precursor molecules with sufficient energy input to directly synthesize SACs without solvent. Ma and Ji's group synthesized noble metal SACs from 10 g to 1.035 kg through the ball-milling and calcination treatment of two kinds of acetylacetone precursors (one containing noble metals Pd, Rh and Ru, and the other containing non-noble metals Zn and Cu) at a 1:400 weight ratio.[115] The average distance between noble metal atoms is significantly increased, effectively preventing the possible aggregation of noble metal species in subsequent calcination. This method does not require templates, additives or solvents, which greatly reduces the complexity of manufacturing and processing, thus reducing the cost. Similarly, Ji's group also mixed cheaper acetate precursors with two different metal centres, such as $Au(Ac)_3$ and $Ni(Ac)_2$ (Ac = acetate), at a lower weight ratio of 1:1000 for the ball-milling process.[116] After calcination, the two acetate salts are converted into corresponding metal oxides, resulting in Au SAs with a weight percentage of 0.12 wt%. Such Au SACs can be scaled-up to 1.025 kg through a single batch synthesis in the laboratory. In addition, the modified method can also be applied to the preparation of other SAs such as Ir on other substrates (*e.g.* ZnO and NiO).

At present, the strategies for large-scale synthesis of SACs mainly include wet chemical methods (ligand assisted synthesis and two-step heat treatment) and dry chemical methods (mechanical ball milling preparation and physical mixing assistance), which can already synthesize kg-level SACs to fulfil small-scale industrial applications. However, the resource and energy consumption, as well as the SA loading amount and stability of these methods, still need further researches to compete with bulk or nanoparticle metal catalysts in practical applications.

4.4 Other synthetic strategies of SACs

In most cases, the production process of SACs includes the preparation, mixing and waste disposal of nitrous, organic and toxic substances, which is contrary to the principle of sustainable development. Although some ball-milling methods claim that no solvent is needed by physically mixing metal salts and substrates, several steps still potentially generate hazardous waste. Baek and colleagues developed an environmentally friendly and low-cost strategy that directly converts bulk metal into single atoms without producing by-products and waste.[117] Target metal balls, N_2 gases and graphite are ball-milled in a reactor. Different from other mechanical mixing methods using metal salt, the metal ball forms atomized metal *via* an atomic-scale abrasion and transfers kinetic energy to drive the reaction. Dispersed SACs (Fe–N–C, Co–N–C, Ni–N–C and Cu–N–C) are evenly produced during a one-step mechanical reaction. By controlling the rotation speed, milling time, reactor volume and abrasion parameters, loading amount and productivity can be adjusted. The method can also be applied to a wide range of metals or dual metals on various substrates *via* a stable bonding between them. Another green method is to deposit and

collect gaseous products downstream of the tubular furnace. Wang and Ye's group developed a gaseous acid-mediated strategy for direct top-down atomization of industrial metal particles (Fe, Co, and Ni) with sizes up to 45 μm to metal ions using gaseous HCl generated from NH_4Cl that can be confined by nitrogen-doped carbon. At low temperatures, downstream of the tubular furnace, the gaseous NH_3 and HCl condense into solid NH_4Cl, which can be recycled facily.[118]

General synthesis strategies based on mechanochemical abrasion, thermal shockwave and laser irradiation are feasible but often require special equipment. Cost-effective three-dimensional (3D) printing techniques can directly assemble target materials, thus avoiding complex wet-chemical processes. Qiao's group creatively realized the combination of 3D printing strategy and SACs by using transition metals and natural polymers (gelatin and gelatin methacryloyl) as synthetic precursors (Fig. 10).[119] By changing the recipe of printing ink, the adjustment of element and atom loading in SACs is realized. The characterization results show that even if the transition metal precursor in the precursor is changed or different natural polymers are used as base materials, the obtained materials are still SACs. At the same time, the coordination environments of the obtained SACs can be regulated by changing the precursors and using post-treatment methods. Finally, the characterization results show that the use of different 3D printing parameters does not affect the dispersion of atoms in the final material. The electrocatalytic performance of the electrode was verified through nitrate reduction reaction. Compared with the carbon substrate electrode without SAs, the electrode with iron SAs shows higher electrocatalytic performance, which proves that the 3D printing process does not affect the electrochemical performance of the SACs. The combination of 3D printing strategy and SACs provides the continuous production ability and multi-scale expansion ability to SACs. This synthesis strategy provides a potential way for large-scale production or continuous production of SACs. At the same time, cheap 3D printers and 3D printing ink materials significantly reduce the cost of large-scale production, bringing potential opportunities for the subsequent large-scale industrial production and application of SACs.

The concept of "click chemistry" was proposed by Barry Sharpless and his colleagues in 2000, who received the 2022 Nobel Prize in chemistry.[128] Click chemistry aims to synthesize target products quickly without unnecessary by-products, *e.g.*, C–C or C–N coupling reactions. SACs can also be synthesized by click chemistry. Zhang's group chose cobalt-coordinated porphyrin and carbon nanotubes as precursors.[120] Given the high reaction selectivity between the carboxyl and amino groups, an amidation reaction was chosen as the click reaction to transplant cobalt-coordinated porphyrin with carboxyl onto the carbon nanotube substrate with amino groups. As a result, Co SACs with 1.71 wt% Co SAs can be detected without aggregation morphology. The clicking confinement technique has high specificity and is transferable to various SAC systems.
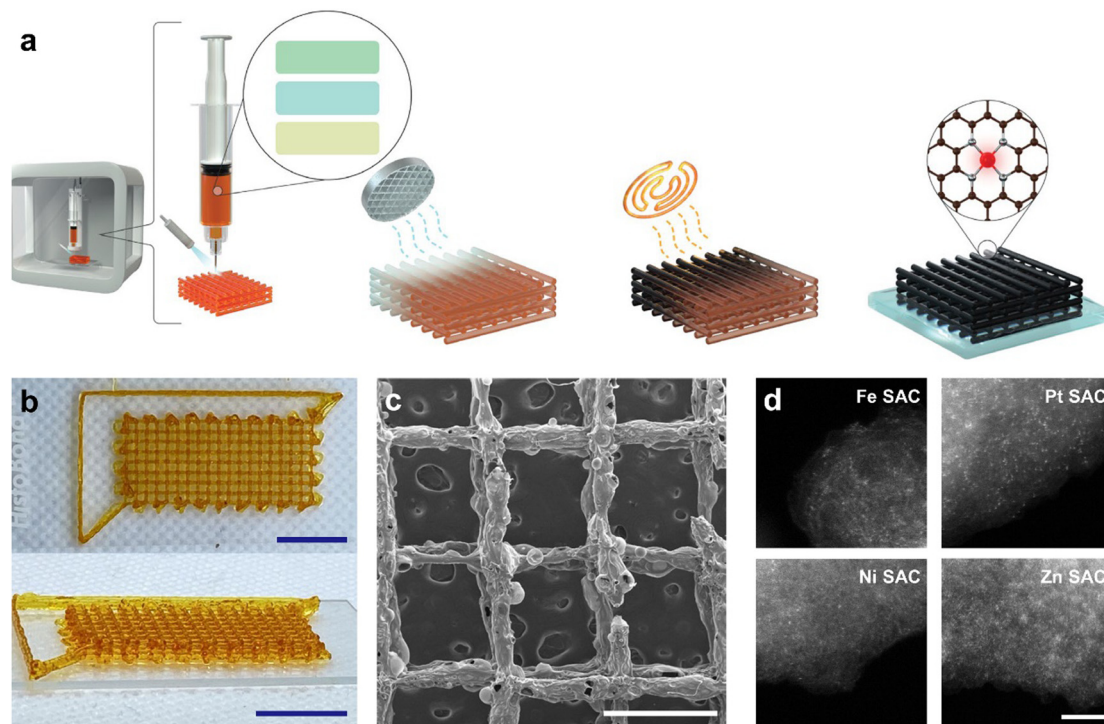
Fig. 10 (a) Synthesis schematic representation for 3D-printed SACs. (b) Photographs of the prepared precursor for SACs. Scale bars: 1 cm. (c) SEM image of 3D-printed Fe SACs with the hole size of precursor being 2.0 mm. Scale bar: 1 mm. (d) HAADF-STEM images of Fe, Pt, Ni and Zn SA sites. Scale bars: 2 nm. Reproduced from ref. 119 with permission from Springer Nature, copyright 2023.

5 Sensing applications of SACs

SACs have been actively explored in the fields of energy, environment, and health in recent years due to their excellent catalytic activity in redox processes, indicating their tremendous potential in catalytic sensing applications.[19,129] This section summarizes the recent progress of SACs for sensing gaseous inorganic and organic compounds, ions and small molecules in liquids, and biological molecules. Different mechanisms and the structure–activity relationships between SACs and analytes are emphatically discussed.

5.1 SAC-based gas sensing

With the improvement of industrial technology, gas sensors have gradually benefited in the fields of environmental monitoring, military safety, disease diagnostics, and food industries. In the past few years, SACs with their excellent sensitivity, low detection limits, high selectivity, good stability and 100% atomic utilization, have been considered attractive materials for gas sensing.

The interactions between SACs and gaseous molecules typically involve physical adsorption and chemical reaction, leading to an increased/decreased resistance of the SACs depending on the catalyst species (p-type or n-type) and gas species (reducing or oxidizing). Here, recent advances in SAC-based sensors for inorganic (oxidizing/reducing) and organic gases (reducing) are thoroughly discussed, and Table 2 compares their performance.

5.1.1 Inorganic oxidizing gas sensing.
Oxidizing gases, for example, nitrogen dioxide (NO_2) with a significant negative environmental impact, have been widely studied in gas sensing. NO_2 not only contributes to ozone formation and acid rain, but also harms humans even at very low concentrations (<3 ppm).[130] In addition, long-term exposure to NO_2 levels as low as tens of ppb can cause asthma, especially in youngsters and the elders.

To detect oxidizing NO_2 of low concentrations, an n-type semiconductor based on noble metal SAs is the primary choice. Xue *et al.* designed a step-rich ZnO ladder to load Au SAs (Au_1–ZnO).[131] The curved-edged ZnO with a large number of dangling bonds and defects serves as susceptibility centres for site-selective anchoring of isolated Au SAs (Fig. 11a). In the range of 10–300 ppb NO_2, Au_1–ZnO displayed a linear response and a 1.6- and 7-fold ($R_g/R_a = \sim 12.6$) higher response compared with Au NP–ZnO and ZnO (Fig. 11b). Au may function as a chemo-sensitizer when Au_1–ZnO is exposed to oxidizing NO_2 gas, hence facilitating the activation kinetics between NO_2 and adsorbed oxygen as well as the electron transfer between NO_2 and the carrier (ZnO). This can also be demonstrated by DFT calculation: a new band gap appears after anchoring Au SAs, which is broadened after the adsorption of NO_2 molecules (Fig. 11c).

Although loading noble metals (*e.g.*, Au, Pd, Pt and Ag) helps to improve the performance of NO_2 sensors, the high cost and scarce resources of noble metals restrict their widespread implementation. Tian *et al.* fabricated an atomically dispersed

Chem Soc Rev

Table 2 Comparison of the sensing properties of different SAC-based gas sensors

Type of gases	Analytes	Catalysts	Active sites	Active metal loading	Type of sensor	LOD (ppm)	Linearity range (ppm)	Sensitivity/response	Ref.
Oxidizing gases	NO_2	Au_1–ZnO	Au	0.32 wt%	CR	0.01	0.0126–0.03	41 ppm^{-1}	131
		AD FeNC	Fe–N_4	0.75 at%	CR	0.28	1–200^a	31% at 20 ppm	132
		$Pb_xCd_{1-x}Se$ QD gels	Pb, Cd	—	CR	0.003	0.1–0.6	0.6 ppm^{-1}	134
		$MoSe_2$:Nb 1C	Nb	—	CR	3	0–50^a	8.03 at 3 ppm	135
		$Ni_1/TiN_{0.5}C_{0.5}$	Ni	—	CR	0.01	0.1–0.5	~34.6 ppm^{-1}	133
Reducing gases	H_2	Pd/Co_3O_4	Pd–O	5.4 wt%	CR	—	—	~85% at 1000 ppm	74
	H_2S	In_2O_3/Pd_{atom}	Pd	0.26 wt%	CR	0.1	0–20^a	6.728 ppm^{-1}	136
		Pt SA-anchored $CuCrO_2$	Cu–V_O–Pt Cr–V_O–Pt	1.39 wt %	CR	0.0446	0–10^a	1250 at 10 ppm	137
		$Pt-B-MoS_2$	Pt–S	—	CR	1	0–50^a	205% at 10 ppm	138
	NH_3	AD CoNC	Co–N_4	1.0 at%	CR	100	20–1000^a	1.34 at 100 ppm	140
	SO_2	SAC–Ni/H–SnO_2	Ni	0.75 wt%	CR	0.1	0.1–40	0.61 ppm^{-1}	141
	CO	Pd_1–TiO_2	Pd–O–Ti	0.14 at%	CR	0.024	0.1–100	~1.25 ppm^{-1}	45
		Cr/ZnO	Cr–O	0.5 wt%	CR	—	—	65.45%	159
VOCs	TEA	$SA-Pt/WO_3$	Pt (II)	0.22 wt%	CR	0.00018	~2–20	28.37 ppm^{-1}	144
		Pt/SnO_2	Pt–O	—	CR	0.007	0.1–100	8.76 ppm^{-1}	145
		$AD–Ag–WO_3$	Ag	—	CR	0.0017	0.1–50^a	5150 at 50 ppm	146
		3DOM Pt/SnO_2	Pt–O	0.20 wt%	CR	0.00032	0–100	8.135 ppm^{-1}	147
		0.25 Pt/In_2O_3 (H_2)	Pt	<0.25 wt%	CR	0.00005	10–100	48.5371 ppm^{-1}	148
		Pt $SA-Ti_3C_2T_x$	Pt	—	FET	0.014	0–10^a	~6% at 10 ppm	149
	TMA	Pt SAs/WO_3	Pt–V_O–W	0.1 at%	CR (PTM)	0.00000078	0.01–1^a	6541.5 at 1 ppm	150
	Xylene	Pt SAs/WO_3	Pt–V_O–W	0.1 at%	CR (PTM)	0.00000018	0.01–1^a	1001.1 at 1 ppm	150
		$PtCo–WO_3$	Pt	0.08 wt%	CR	0.00108	0–80	3.91 ppm^{-1}	153
	HCHO	Au/In_2O_3	Au	0.0154 wt%	CR	0.00142	5–100	1.57 ppm^{-1}	154
		$Pt-MCN–SnO_2$	Pt–C/N	4.3 wt%	CR	1	0.05–5^a	33.9 at 5 ppm	155
Organic vapour	Methanol	$Ag–LaFeO_3@ZnO–Pt$	Pt–O–Zn	0.75 wt%	CR	0.00327	0.062–100^a	453.02 at 5 ppm 21.25 at 0.062 ppm	26
	Ethanol	$Pt–MoS_2$	Pt	—	CR	5	5–100^a	—	89
		AMC $ZnNC_2$	Zn–NC_2	—	CR	50	50–1500^a	~0.26 at 1500 ppm	157
		$Pt_1–Fe_2O_3$-ox	Pt–O	—	CR	10	10–200^a	102.4 at 100 ppm	158
		Pt $SAs@SnO_2$ NRs@SiC NSs	Pt	—	CR	0.500	—	119.75 at 500 ppm	81
	Acetone	$Pt–MoS_2$	Pt	—	CR	20	20–400^a	—	89
		$Pt_1–SnO_2$ NSs	Pt–O	2.12 wt%	CR	1	0–10^a	95.4 at 10 ppm	111
		Pt_1/TiO_2 NRs@NSs	Pt–O_4	0.25 wt%	CR	—	5–500^a	13.6 at 50 ppm	156
		$Eu/nanoC_3N_4$	Eu–N	4.0 wt%	LS	—	—	71.0%^{b}	85
	Cyclohexane	$Eu/nanoC_3N_4$	Eu–N	4.0 wt%	LS	—	—	79.1%^{b}	85

List of abbreviations. AD: atomically dispersed, AMC: atomically dispersed metal catalysts, CMS: the carbonaceous microsphere templates, CR: chemiresistive, FET: field effect transistor, LS: luminescent, MCN: melamine-derived carbon nitride nano-sheet, $MoSe_2$:Nb 1C: the Nb-doped $MoSe_2$ obtained after one and five plasma-enhanced atomic layer deposition cycles, NRs: nanorods, NSs: nanosheets, PTM: pulsed temperature modulation, and V_O: oxygen vacancy. ^{a} Note: detection range. ^{b} Quenching efficiency (QE).

non-precious iron–nitrogen-doped carbon catalyst (AD FeNC) for NO_2 sensing, which realized a low LOD of 0.28 ppm at room temperature.[132] DFT confirmed that the AD FeNC is an n-type semiconductor with a strong surface affinity for NO_2 molecules. The AD FeNC with an FeN_4 coordination significantly lowered the barrier for NO_2 decomposition from >2.60 eV to 0.73 eV, making it remarkably selective for NO_2 detection compared to five commonly encountered gases (NO, H_2, NH_3, CH_4 and CO_2). Additionally, the AD FeNC has a long response time (t_{res} = 1270 s) and recovery time (t_{rec} = 1300 s) for 20 ppm NO_2.

In order to achieve both a strong response and a quick recovery time, coupling an extensive amount of electron transfer and weak adsorption energy is desired. However, charge transfer is usually associated with adsorption energy. Geng *et al.* prepared bimetallic PbCdSe quantum dot (QD) gels containing Pb ionic sites (Pb_xCd_{1-x} QD).[134] Pb ionic sites were atomically dispersed in the gels with low Pb contents (x = 0.04 and 0.09). When x was 0.09 ($Pb_{0.09}Cd_{0.91}Se$ QD), it exhibits an optimal combination of high response (0.06%/ppb), ultra-low LOD (3 ppb), the fast t_{res} (28 s), and short t_{rec} (60 s) to NO_2

sensing. Atomically dispersed Pb sites in the hexagonal CdSe matrix can transmit electron density to nearby Cd cations, enabling them to offer NO_2 with more electron donors and thereby boost the response.

Long-term stability is also significant for practical applications. Compared to easily oxidized 2D $MoSe_2$, Nb SAs doped $MoSe_2$ by the plasma enhanced atomic layer deposition (PEALD) method exhibit little resistance change to NO_2 (11.3%, that of $MoSe_2$ is ~99.6%) over 120 days.[135] The difference in the lattice distance between Mo—Se and Nb—Se causes lattice distortion. Such distortion degrades the honeycomb structure of ternary $MoSe_2$. Meanwhile, adding Nb at grain boundaries of $MoSe_2$ helps reduce defects such as dangling bonds and vacancies, making the SACs more impervious to oxidation and therefore showing higher stability. Mxenes are another promising 2D support for SAs to increase stability. Cao and colleagues proposed a one-step molten salt etching method to anchor Ni SAs on MXene analogues.[133] The Ni SAs doped in the lattice of $TiC_{0.5}N_{0.5}$ enable greater charge transfer from Ni atoms to neighbouring Ti atoms, leading to good selective
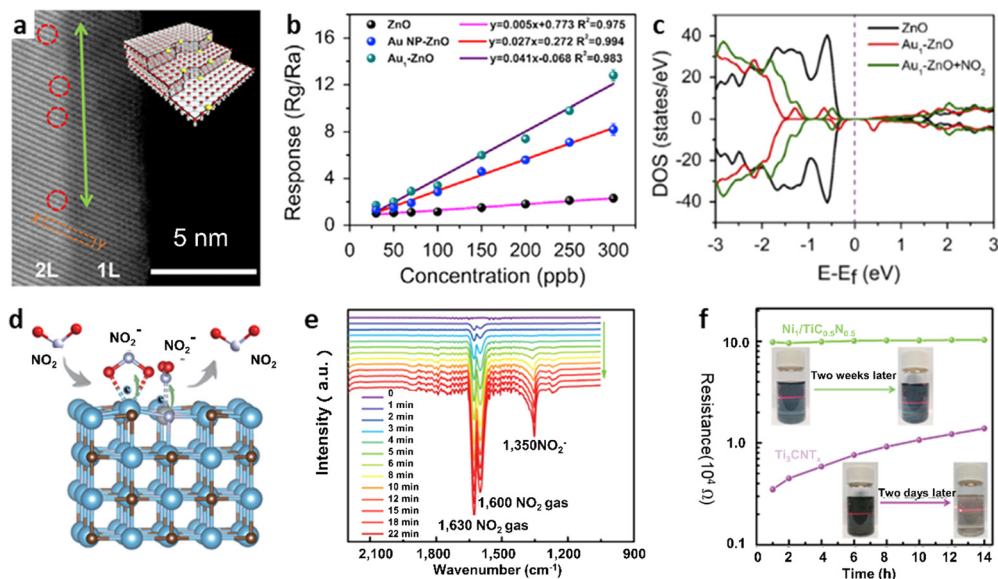
Fig. 11 (a) HAADF-STEM image and structural scheme (inset) of $Au_1–ZnO$. (b) The sensing responses for $Au_1–ZnO$ and reference samples at different NO_2 concentrations. (c) The calculated density of states for bare ZnO, $Au_1–ZnO$, and $Au_1–ZnO + NO_2$. Reproduced from ref. 131 with permission from Elsevier Inc., copyright 2020. (d) Mechanism of NO_2 sensing on Mxenes analogue $TiC_{0.5}N_{0.5}$ doped with Ni SAs ($Ni_1/TiN_{0.5}C_{0.5}$). (e) *In situ* FT-IR spectra during the NO_2 adsorption process on the $Ni_1/TiN_{0.5}C_{0.5}$. (f) Measured resistance of $Ni_1/TiN_{0.5}C_{0.5}$ and Ti_3CNT_x (MXene) in the presence of air. Inset: photographs of colloidal solutions of $Ni_1/TiN_{0.5}C_{0.5}$ (top) and Ti_3CNT_x (bottom) in the presence of air. Reproduced from ref. 133 with permission from Tsinghua University Press, copyright 2022.

adsorption of electrophilic NO_2 molecules and a low LOD of $\sim$10 ppb (Fig. 11d–e). $Ni_1/TiC_{0.5}N_{0.5}$ also shows strong tolerance to O_2, which has a stable baseline in the air for two weeks, superior to titanium-carbonitride (Ti_3CNT_x) (Fig. 11f).

5.1.2 Inorganic reducing gas sensing. Hydrogen (H_2) has a high calorific value during combustion and good reducibility, making it a potential replacement for fossil fuels. However, H_2 becomes explosive and flammable when its concentration exceeds 4%. Therefore, a fast response is a crucial requirement for H_2 sensing, which can be significantly enhanced by surface decoration with SAs. The noble metal palladium has the most substantial adsorption for hydrogen. Koga investigated different loading amounts of Pd atoms (0–20%) on Co_3O_4 NPs (Fig. 12a) *via* reactive pulsed laser ablation (PLA).[74] When the Pd loading was 5%, the Pd SA density reached the highest (5.4 wt%), and the SMO-based sensor exhibited high sensitivity ($\sim$85%) and fast t_{res} ($\sim$13 s) to 1000 ppm H_2 (Fig. 12b). XPS and XANES spectra both demonstrate that about 10% of the individual Pd atoms in the Pd^{4+} state are reduced to Pd^{2+} at 1000 ppm H_2 (Fig. 12c), implying that $Pd^{4+} \leftrightarrow Pd^{2+}$ catalytic redox cycle is the key to accelerating the water formation reaction and improve the H_2 sensing rate.

Pd atoms can also lower the operating temperature of SMOs (normally $> 250\ ^\circ C$) to selectively sense other combustible gas such as carbon monoxide (CO). Ye *et al.* synthesized Pd SAs on TiO_2 nanoflowers ($Pd_1–TiO_2$) *via* a photochemical method.[45] Experiments demonstrated that the LOD of $Pd_1–TiO_2$ to CO at room temperature is as low as 24 ppb, which is one order of magnitude lower than that of the reported best CO sensor, including the ones obtained at high working temperatures. UV-

vis spectroscopy and ultraviolet photoelectron spectroscopy analysis indicate that $Pd_1–TiO_2$ displays the p-type nature, that is, O_2 molecules acquire electrons on the $Pd_1–TiO_2$ surface to form active oxygen species (O_2^-) (Fig. 12d). The conductivity state of $Pd_1–TiO_2$ changes with adsorption/desorption of reductive analytes such as CO. As CO reacts with the O_2^- to generate the sensing signal, the concentration of O_2^- on the sensing material is an essential determinant of its sensitivity. Electron spin resonance (ESR) spectroscopy (Fig. 12e) confirms that $Pd_1–TiO_2$ (0.14 at%) shows much higher efficiency in increasing O_{ads} (52.12%) than pristine TiO_2 (8.02%) and Pd NPs–TiO_2 (31.59%), and thereby exhibits a much higher response of 12 692% at room temperature.

Another toxic industrial gas, hydrogen sulfide (H_2S), also requires low operating temperature sensing to minimize energy consumption and avoid spontaneous combustion and explosion. Duan *et al.* fabricated Pd SAs on In_2O_3 substrates (In_2O_3/Pd_{atom}) *via* a MOF-templated method, lowering the working temperature from 200–400 $^\circ C$ (In_2O_3) to 100 $^\circ C$.[136] Compared with pure In_2O_3, Pd NPs supported on In_2O_3 (In_2O_3/Pd_{nano}) and PdO particles supported on In_2O_3 (In_2O_3/PdO), In_2O_3/Pd_{atom} demonstrate the highest sensitivity (6.728 ppm^{-1}) and excellent H_2S selectivity among various reducing VOCs and volatile sulfur compounds (Fig. 13a). It can be concluded that atomic Pd sites significantly enhance the surface affinity for H_2S molecules, and the H–S bond of the H_2S molecules adsorbed on Pd SA sites is easier to split apart into S species with a small barrier (Fig. 13b). Quasi *in situ* XPS analysis identified sulfur species during H_2S sensing, which may be the primary cause of the sensing signal. Similarly, Meng *et al.* proposed a Pt SA anchored
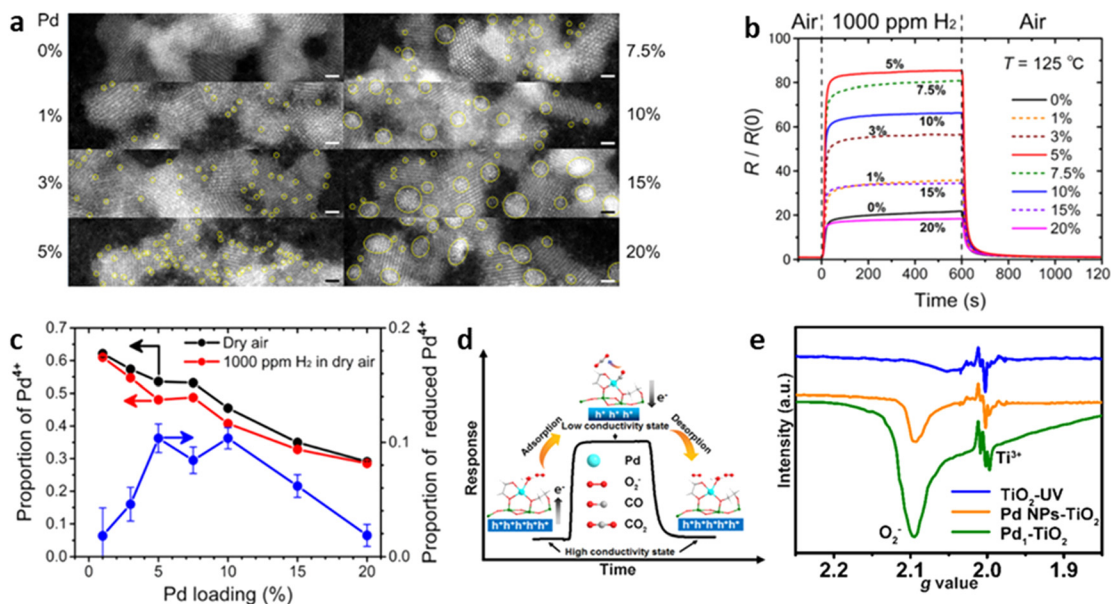
Fig. 12 (a) HAADF-STEM images of Pd–Co₃O₄ NPs with various Pd loading amounts. The small and large yellow circles represent Pd SAs and PdO$_x$ clusters, respectively. Scale bar: 1 nm. (b) Response and recovery curves at 125 °C and 1000 ppm H₂ for Pd–Co₃O₄ with 0–20% Pd loading amount. (c) Influence of Pd loading amount on Pd^{4+} proportions after exposure to dry air and 1000 ppm H₂ in dry air, as well as on the proportion of Pd^{4+} reduced to Pd^{2+}. Reproduced from ref. 74 with permission from American Chemical Society, copyright 2020. (d) Proposed mechanism of Pd₁–TiO₂ for CO sensing and (e) ESR spectra of Pd₁–TiO₂ and reference samples at 90 K. Reproduced from ref. 45 with permission from American Chemical Society, copyright 2021.
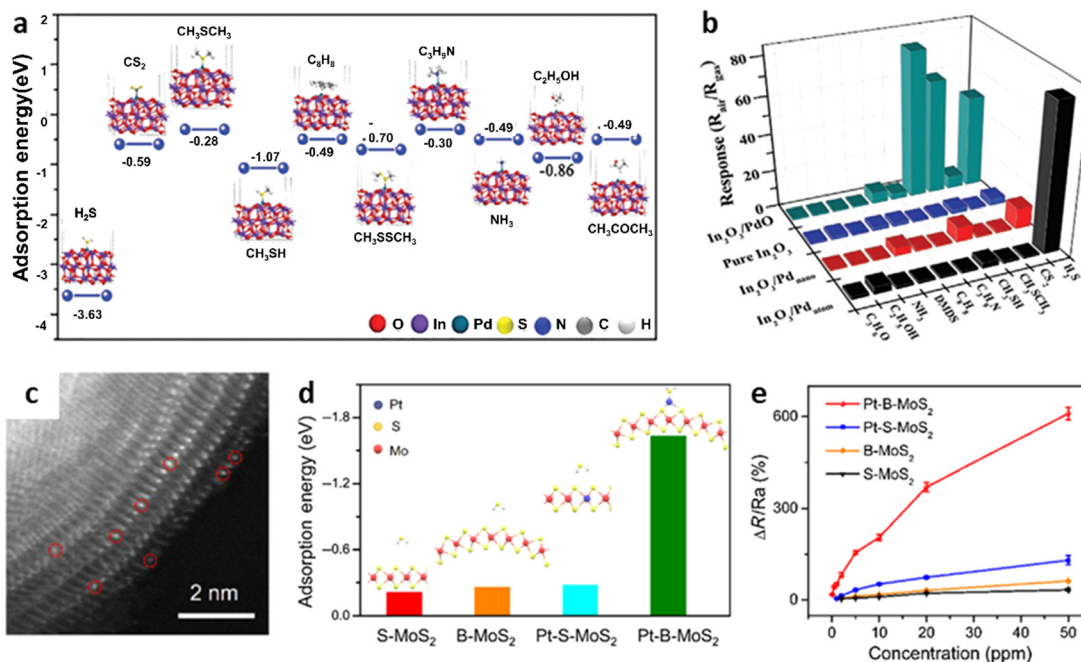

Fig. 13 (a) The surface adsorption energy of In₂O₃/Pd$_{atom}$ toward various gas molecules. (b) The selectivity of In₂O₃/Pd$_{atom}$ and reference samples towards various gases at 100 °C and 10 ppm concentration. Reproduced from ref. 136 with permission from Wiley-VHC, copyright 2021. (c) The HAADF-STEM image of Pt decorated bending MoS₂ (Pt-B-MoS₂). (d) The adsorption energy of Pt-B-MoS₂ and reference samples towards H₂S molecules. (e) The sensing responses of Pt-B-MoS₂ and reference samples at various H₂S concentrations. Reproduced from ref. 138 with permission from Chinese Chemical Society, copyright 2022.

CuCrO₂ sensor, which could significantly improve the sensor's response from ∼35 to 1250 when exposed to 10 ppm H₂S at 100 °C.[137] Despite the interference of water vapour, the Pt-anchored CuCrO₂ sensor ensures a high response (∼50) at 90%RH.

In order to further maximize the sensitivity and selectivity, the adsorption and electron transfers need to be optimized. Wu's group proposed strain-assisted Pt SAs on a high-curvature MoS_2 surface (Pt-B-MoS_2) (Fig. 13c).[138] A multilayer MoS_2 structure with bending base planes (0.8% stretch strain) was achieved by using N-methyl-2-pyrrolidone as a guiding molecule. Such a curved MoS_2 surface confers a unique "tip" effect to the low-coordinated Pt SAs, resulting in more electron accumulation around the Pt species and thus accelerating the electrical transfer between H_2S and MoS_2 supports (Fig. 13d). Compared with straight MoS_2 (S-MoS_2), B-MoS_2, and Pt–S-MoS_2, the Pt-B-MoS_2 species are found to have the strongest adsorption ability (E_{ads} = −1.63 eV, S-MoS_2: –0.21 eV, B-MoS_2: –0.26 eV, Pt–S-MoS_2: ∼–0.28), thereby enabling a higher response (205% at 10 ppm) and faster t_{res} and t_{rec} (25 and 20 s) to H_2S sensing at 25 °C (Fig. 13e).

Another critical issue is to avoid the sulphur poisoning that often occurs in catalytic reactions of gases containing S impurities. DFT calculation investigated the mechanism of H_2S adsorption and dissociation on a Ni–N co-doped graphene catalyst.[139] Single vacancy graphene decorated with Ni and one nitrogen atom (PG–Ni–N_1) showed the highest energy barrier among PG–Ni–N_x (x = 1–3) in the determining second dissociation reaction. The calculations demonstrate that PG–Ni–N_1 has the best anti-sulphur properties, which contributes to the development of highly sulphur-tolerant H_2S sensors.

Ammonia (NH_3) is another widely utilized reducing gas in chemical industries. According to Occupational Safety and Health Administration (OSHA) regulations, human bodies cannot be exposed to NH_3 concentrations of 25 ppm for 8 hours or 35 ppm for 10 minutes. The current generation of SMO-based NH_3 sensors still faces challenges at lower operating temperatures (energy consumption). Co SAs anchored on nitrogen-doped carbon synthesized by a sacrificial MgO template method can detect NH_3 from 20 to 1000 ppm at room temperature, which is lower than the OSHA limits.[140] This can be attributed to a large number of ∼50 nm pores significantly increasing the SSA and facilitating the contact between the SACs and NH_3. The doped Co SAs in CoN_4 have a strong affinity for N-containing gas molecules, making the sensor sensitive (R_a/R_g = 1.34) to NH_3 even at room temperature. Besides, due to the difference in oxidation and reduction characteristics of NO_2, NO, and NH_3, the sensor exhibits different resistance change trends, making selectively detection of NH_3 possible. However, the sensor response decreases with increasing humidity as H_2O would inhibit the ammonia oxidation reaction (NH_3 → H_2O) and occupy the active site.

Sulfur dioxide (SO_2) is a unique gas with both reducing and oxidizing properties, in which the sulfur atom is in an intermediate valence state. In the atmosphere, SO_2 can be oxidized into sulfuric acid mist or sulfate aerosol, which is a major precursor of environmental acidification. The human body may be affected if the atmospheric SO_2 concentrations exceed 0.5 ppm. Liu et $al.$ synthesized Ni SAs anchored on the oxygen vacancy-rich SnO_2 nanorods (SAC–Ni/H–SnO_2) by the solvothermal-impregnation-calcination method.[141] The SAC shows high sensitivity (0.61 ppm^{-1}), low LOD (100 ppb, lower than immediately dangerous level) and long-term stability (degraded by only 5% during the 60 day test) to SO_2. In $situ$ Diffuse Reflexions Infrared Fourier Transformations Spectroscopy and ESR characterization shows that the oxygen vacancies on the surface of SnO_2 generate superoxide radicals via electron transfer, while Ni SAs promote the adsorption of SO_2 by creating Ni–S bonds.[142,143] Therefore, the adsorbed SO_2 can effectively release the trapped electrons and react with the abundant superoxide radicals on the surface of SAC–Ni/H–SnO_2 to produce a thinner electron depletion layer and reduce the resistance of SACs.

5.1.3 Organic gas sensing. Organic gases, especially VOCs, are pollutants that can easily volatilize in air under normal atmospheric conditions. Most organic gases are reducing gases; however, their health impact is more concerning as they are harmful to humans and the ecosystem in many daily scenarios at low concentrations. As a result, sensitive, selective, and long-term organic gas detection is gaining traction in scientific research and engineering applications.

Triethylamine (TEA) is a typical VOC species that is widely applied as an organic solvent, a curing agent, a catalyst and a preservative. However, TEA is hazardous due to its volatility, flammability and explosive properties. The OSHA has advised that the environmental TEA concentration should be less than 10 ppm. WO_3 is an n-type semiconductor with a low band gap and has superior charge transport capability. Noble metal SAs anchored on SMOs have presented potential in TEA sensing.[144–148] Wang's group loaded the three-dimensionally ordered macroporous (3DOM) WO_3 with Pt SAs (0.22 wt%) (Fig. 14a) via a colloidal crystal template method, realizing higher sensitivity (28.37 ppm^{-1}) and an ultra-low LOD (0.18 ppb).[144] Here, O_2 molecules in the environment absorb electrons from the conduction band of WO_3 and create adsorbed oxygen (O^-) as a depletion layer to increase the resistance. When exposed to TEA, which has high electron-donating properties and selectively adsorbs to Pt SAs, it is oxidized. Following the reaction, the collected electrons will be released to WO_3, reducing the depletion layer thickness and sensor resistance, resulting in a high sensitivity to TEA. Similarly, Pt SAs on 3DOM SnO_2 (0.20%) also have a low LOD (0.32 ppb) and fast t_{res} (10 s) and t_{rec} (180 s) at 80 °C and 20 RH%.[147] By adjusting the Pt content of the catalyst from 0% to 1%, it is found that 0.20% Pt SA has the highest Hall mobility (contributing to efficient resistance change), the lowest electron concentration (indicating high electron mobility) and the highest resistivity (indicating the formation of reactive oxygen species), thus contributing to the highest response (Fig. 14b). Wang's group further lowered the LOD for TEA to 50 ppt via hydrogen treatment of Pt loaded In_2O_3 nanosheets.[148] After the hydrogen treatment, the sensitivity of Pt/In_2O_3 is significantly improved from 4.0269 to 48.5371 ppm^{-1} in the linear range of 10–100 ppm. This is due to the fact that the amount of low-valence Pt increases after treatment, which stimulates the production of adsorbed oxygen and lowers the TEA response energy barrier.
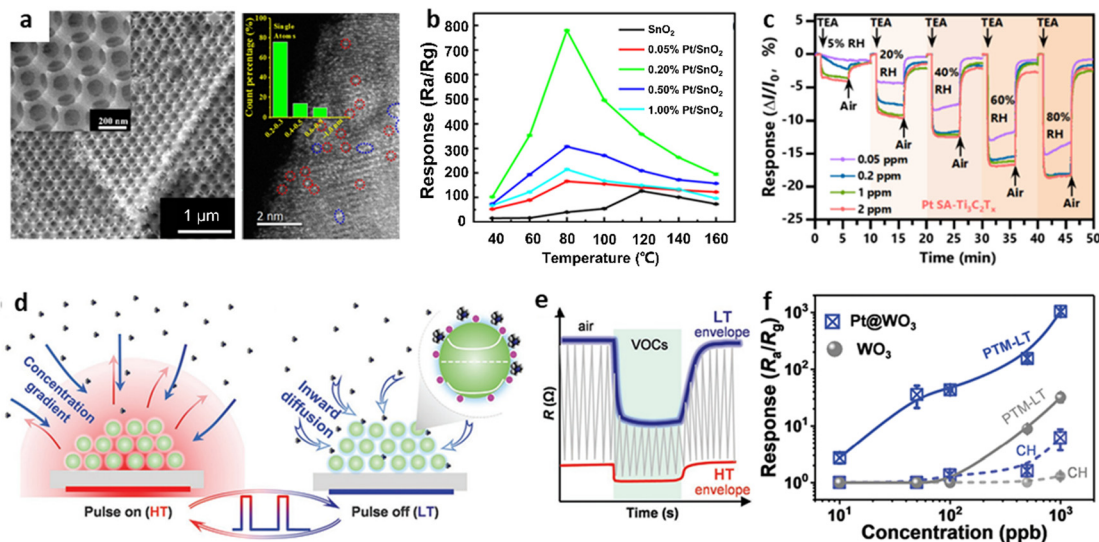
Fig. 14 (a) Left: SEM images (inset: magnified), and right: HAADF-STEM image (inset: size distribution based on >100 Pt species) of SA-Pt/WO₃. Pt SAs and sub-nm clusters are marked with red and blue circles, respectively. Reproduced from ref. 144 with permission from Elsevier B.V., copyright 2019. (b) Response of Pt/SnO₂ with 0–1% Pt to 100 ppm TEA at 40–160 °C. Reproduced from ref. 147 with permission from American Chemical Society, copyright 2022. (c) Sensing responses of Pt SA–Ti₃C₂Tₓ to 0.05–2 ppm TEA at 5%–80% RH. Reproduced from ref. 149 with permission from American Chemical Society, copyright 2022. (d) Gas concentration and temperature gradient throughout the sensor surroundings during the pulsed heating on (left) and off (right). (e) PTM response curve with two separate low and high temperature (LT and HT) envelopes. (f) Responses of WO₃ anchored with and without Pt SAs towards 10–1000 ppb xylene under PTM mode and continuous heating (CH) mode. Reproduced from ref. 150 with permission from Wiley-VCH GmbH, copyright 2022.

However, when operating at higher RH (>33%), the chemiresistive sensor's response will be noticeably reduced because of water molecules adsorbing on SMOs and preventing the formation of adsorbed oxygen. Mao *et al.* investigated the TEA sensing performance and effect of humidity using Pt SA anchored $Ti_3C_2T_x$ (a kind of Mxenes, Pt SA–$Ti_3C_2T_x$) nanosheets fabricated through simple wet chemistry.[149] Although the response of the Pt SA–$Ti_3C_2T_x$ sensor increases with increasing relative humidity (5–80%) in the short term (Fig. 14c), it is found that the sensitivity of Pt SA–$Ti_3C_2T_x$ to 1 ppm TEA decreases by 60 and 89% after 20 day exposure at 20% RH and 80% RH, whereas barely change in an ambient dry environment (5% RH). This can be attributed to the adsorption of water molecules, and oxidation and degradation of p-type $Ti_3C_2T_x$. Therefore, although Pt SAs can enhance the response of $Ti_3C_2T_x$ *via* the chemical sensitization effect and TEA adsorption enhancement, a stable substrate in a humid environment and suitable calibration curves at different relative humidity values to eliminate the influence of humidity are still significant for practical applications.

Toxic VOCs like xylene and formaldehyde are common industrial raw ingredients utilized in everyday life and construction materials. Moreover, there have been numerous related risks in pathology laboratories. The OSHA short-term exposure limit for xylene and formaldehyde is 5 ppm and 2 ppm.[151,152] In order to reduce exposure risk, highly sensitive SACs with abundant active sites are in demand. Wang group added Co and Ni oxides to SA–Pt/WO₃ to fabricate PtCo–WO₃ and PtNi–WO₃.[153] The PtCo–WO₃ (both Pt and Co: 0.08 wt%) showed a low LOD of 1.08 ppb and a high sensitivity of

3.91 ppm⁻¹ for xylene gas. XPS analysis showed that the inclusion of cobalt and nickel can develop oxygen vacancies, which improves Pt SA dispersion to minimize the band gap and increases the electron mobility of WO₃. The higher loading amount of SAs improves the sensitivity of gas sensing. However, excessive loading can lead to SA agglomeration into clusters, reducing the contact area between the catalytic site and the gas molecules, and bringing down the sensitivity.[154] To prevent the aggregation of SAs into clusters, thermally stable substrates are also needed. Shin *et al.* synthesized Pt–MCN–SnO₂ SACs by stabilizing Pt SAs on one-dimensional melamine-derived carbon nitride/SnO₂ heterostructures.[155] Due to its excellent thermal stability, graphitic carbon nitride can effectively inhibit the aggregation of SAs at high temperatures, resulting in a high Pt SA loading of 4.3 wt%. Pt–MCN–SnO₂ exhibits a wide detection range of 0.05–5 ppm and high stability (only 7.1% degradation after >170 h sensing at 275 °C). Pt SAs serves as active sites for O₂ adsorption and dissociation on SnO₂, increasing the concentration of O₍ₐds₎ on the Pt–MCN–SnO₂ surface and improving its catalytic capabilities.

Although there have been notable advancements in the design of SAC-based sensors with LODs at ppb levels, the observed response at the ppb level is low, limiting their potential application in medical analysis. This problem can hardly be solved by the widely adopted strategies of continuously heated chemiresistors working at an optimized fixed temperature, as the preferable working temperatures are usually different for the redox reaction and the adsorption of target molecules. Therefore, Meng's group proposed to equip Pt SAs anchored WO₃ (Pt SAs/WO₃) with a pulsed temperature

modulation (PTM) heating strategy (Fig. 14d and e), which promoted the response for 1 ppm xylene from 5.4 to 1001.1 (Fig. 14f).[150] At a pulsed high-temperature state, abundant oxygen vacancy active sites can be generated on Pt SAs/WO$_3$ surfaces (Fig. 14d, left), while at a pulsed low-temperature state, gas molecules can easily diffuse to the sensing layer driven by a PTM-induced concentration gradient (Fig. 14d, right). Therefore, the charge interaction between the generated active sites and the target gas molecules is significantly improved, offering an ultralow LOD of 0.18 ppt and a considerably high response of 3.1 to 10 ppb xylene.

Commonly used organic solvents in industrial production include ethanol, methanol, acetone, and cyclohexane. Although the health risks of these solvent vapours are lower than those of TEA, xylene, and HCHO, their unstructured emission and industrial safety require more extensive monitoring. Therefore, high selectivity is the key to realizing the applications of sensors. Rong *et al.* synthesized Pt SAs (0 ~ +2 valence) in a 3D porous Ag-LaFeO$_3$@ZnO core–shell sphere with Pt–O–Zn interactions.[26] The SACs exhibit good selectivity with the best sensitivity to methanol gas than others (453.8 to 124.1). DFT simulations demonstrated that addition of Pt SAs improves the adsorption and activation energy of Ag-LaFeO$_3$@ZnO to methanol gas and oxygen, hence greatly enhancing the sensitivity and selectivity. Besides the component and coordination of SACs, the substrate structure is also important. Wu's group grew perpendicular TiO$_2$ nanosheets on TiO$_2$ nanorod-supported Pt SACs, creating microchannels to guide gas molecules to the Pt SA sites and thus facilitate the mass transfer and reaction (Fig. 15a).[156] The growth of nanosheets introduces numerous vacancies and dislocations around the nanosheet–nanorod interfaces (Fig. 15b), reducing the electronic states and coordination of Pt species, strengthening the O$_2$ adsorption (Fig. 15c), and enhancing the selective sensing response to acetone gas by three times (Fig. 15d).

Creating a chemical adsorption process will enable more selective sensing than physical adsorption. Qiu *et al.* synthesized atomically distributed nitrogen–zinc-codoped graphene catalysts, which exhibited a 25% response to 1500 ppm ethanol and high selectivity.[157] The SAC-based sensor DFT simulations demonstrated that ethanol was chemically adsorbed on the SACs *via* forming a strong Zn–O bond, resulting in a noticeable charge transfer from ethanol to SACs. In addition, Pt SAs with higher valence may effectively promote the selective adsorption of ethanol. Li *et al.* oxidized Pt SAs in one-dimensionally aligned Fe$_2$O$_3$ nanoparticles (Pt$_1$–Fe$_2$O$_3$) *via* air-heating.[158] After the oxidizing, Pt^{2+} in Pt$_1$–Fe$_2$O$_3$ changes to approximately Pt^{4+} in Pt$_1$–Fe$_2$O$_3$–ox, and develops a stronger interaction with Fe. The Pt$_1$–Fe$_2$O$_3$–ox shows the highest response (R_a/R_g) and a more robust selectivity for ethanol, approximately 12- and 3-fold higher than those of Fe$_2$O$_3$ and Pt$_1$–Fe$_2$O$_3$.
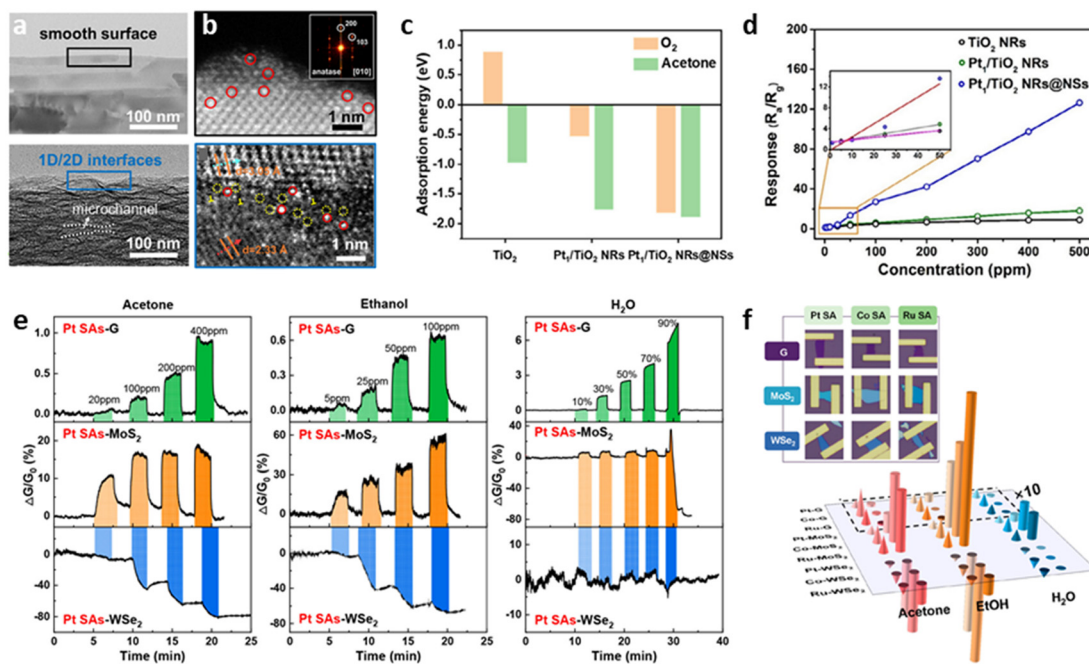

Fig. 15 (a) TEM and (b) HAADF-STEM images of the interface structure of Pt$_1$/TiO$_2$ NRs (up) and Pt$_1$/TiO$_2$ NRs@NSs (down). SAs are marked by red circles, vacancies are marked by yellow circles, and dislocations are marked by yellow ⊥. (c) Calculated adsorption energies of O$_2$ and acetone on Pt$_1$/TiO$_2$ NRs@NSs and reference samples. (d) Response of Pt$_1$/TiO$_2$ NRs@NSs and reference samples to acetone with different concentrations. Reproduced from ref. 156 with permission from Wiley-VCH GmbH, copyright 2022. (e) Relative conductivity response of Pt–graphene, Pt–MoS$_2$ and Pt–WSe$_2$ SACs when exposed to 20–400 ppm acetone, 5–100 ppm ethanol and 10–90% RH water vapour. The coloured regions show the gas/vapour exposure time. (f) Conductivity response of SAC arrays when exposed to 400 ppm acetone, 100 ppm ethanol and 20% RH water vapour. Left cones: binding energies and right tubes: response intensity, those within the black dotted frames are multiplied 10 times. Inset: optical view of a proposed SACs' sensor array. Reproduced from ref. 89 with permission from American Chemical Society, copyright 2022.
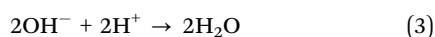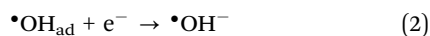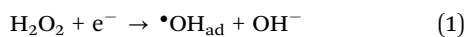
The current sensing of solvent vapour using SACs has achieved high sensitivity and selectivity but is still susceptible to interference from gas molecules with similar structures and chemical properties.[81,158] To solve this problem, a SAC-based sensor array is an effective way. Ding's group used 2D atomic crystal materials (metallic graphene, n-type MoS_2 and p-type WSe_2) as substrates on which Pt, Co and Ru SAs were loaded (Fig. 15f, inset).[89] As the binding energies of various VOC molecules and SACs are different, sensor arrays constructed from a diverse set of SAs and 2D crystal supports can identify various VOC molecules (ethanol, acetone and water vapour) based on their different response in mixtures *via* the principal component analysis method (Fig. 15e and f).

Apart from SAC-based chemiresistive sensing, luminescence sensing also shows potential due to its convenience in visualization. Mori *et al.* doped Eu^{3+} into the exfoliated g-C_3N_4 nanosheets with a high quenching efficiency (QE = $(1 - I/I_0) \times 100\%$) of acetone and cyclohexane at 10 ppm. This can be attributed to the bonds between Eu^{3+} ions and six N atoms from three heptazine units.[85] Eu/nanoC_3N_4 exhibits Eu^{3+} emissions owing to the $^5D_0 \rightarrow {}^7F_2$ transitions, which can be rapidly quenched at room temperature by VOCs with moderate adsorption energies, such as acetone and cyclohexane. In addition, humidity can also affect the quenching efficiency of Eu/nanoC_3N_4, only maintaining a 30.1% response when sensing acetone gas contain 10 vol% H_2O.

5.2 SAC-based liquid sensing

Online and real-time monitoring of molecules and ions in liquid is essential for environmental protection, industrial processes and even human health, which has attracted considerable attention over the past decades. Like gas sensors, SACs with high surface defects, multiple exposed active sites, high conductivity, and specific ability to bind to the detector and accelerate electron transfer are favoured for detecting small molecules and ions in liquids. The difference between liquid and gas sensors in the SAC sensing mechanism is that water as a medium would be involved in catalytic reactions of liquid sensors, and liquid sensors are usually electrochemical types. Here, recent advances in SACs sensors for H_2O_2, ions, and organic pollutants are carefully discussed with their performance comparison in Table 3.

5.2.1 H_2O_2 sensing. H_2O_2 is a versatile green oxidant widely used in chemical, food, and medical applications. In 2024, H_2O_2 production will reach 6000 kt, worth US$6.4 billion.[160,161] However, high-concentration H_2O_2 can cause irreversible damage to the human gastrointestinal tract and mucous membranes.[162,163] Therefore, it is essential to quickly measure the concentration of H_2O_2 in liquids. The essence of detecting H_2O_2 is a two-electron pathway of the oxygen reduction reaction process of H_2O_2 to H_2O:[164]

$$H_2O_2 + e^- \rightarrow {}^\bullet OH_{ad} + OH^- \qquad (1)$$

$$^\bullet OH_{ad} + e^- \rightarrow {}^\bullet OH^- \qquad (2)$$

$$2OH^- + 2H^+ \rightarrow 2H_2O \qquad (3)$$

where $^\bullet OH_{ad}$ is the hydroxyl radical adsorbed on the electrode surface. As the H_2O_2 reduction is a two-electron transfer process, SACs with two-electron transfer capability are preferred to detect H_2O_2 rapidly.

Transition-metal (TM) SA motifs coordinated in a well-defined carbon matrix, with a range of tuning knobs such as distinct metal atom centres and various nearby coordinative dopants, have attracted the researchers' interests in the heterogeneous catalysis field.[165] The earlier report of SACs with TM SAs to detect H_2O_2 was in 2018 by Hu's group.[166] An ordered mesoporous carbon structure containing atomically dispersed Fe–N–C sites achieves a broad detection range (8–23 000 μM), low detection limit (5 μM) and high sensitivity (709.63 μA mM^{-1} cm^{-2}) to H_2O_2 sensing. The highly ordered mesoporous structure promotes the diffusion of the analyte and allows for the uniform distribution of atomically dispersed Fe–N–C sites on the surfaces. The Fe–N–C sites allow for a faster electron transfer and a higher adsorption and catalytic effect of H_2O_2. Similarly, Fe SAs anchored N-doping graphene also shows a high sensitivity of 3214.28 μA mM^{-1} cm^{-2} (Fig. 16a and b).[167] DFT calculation exhibits that the distances between neighbouring sites match the optimum "bridge-adsorption" mode for the catalysis.

Cobalt is highly selective for two-electron transfer, which can provide adequate sites for H_2O_2 sensing.[168–171] Our group developed an atomic Co–N_x–C site anchored neuronal-like carbon-modified amperometric sensor (Fig. 16c), which exhibited a broad detection range (250 nM–50 mM), high sensitivity (743.3 μA mM^{-1} cm^{-2}), strong selectivity, robust reliability (2.86% decay for one week) and fast response (5 s) for residual H_2O_2 detection.[168] The atomic Co–N_x–C sites can promote the two-electron transfer and reduce the production of intermediate products ($^\bullet OH_{ad}$), enhancing the selectivity. Such SACs can be integrated into portable devices, which display sensing data on smartphones (Fig. 16d). In order to improve the Co–N_x–C sites for higher H_2O_2 sensing sensitivity, we also developed Co NPs and atomic Co–N_x anchored on nitrogen-doped carbon nanotube arrays (Co–N/CNT) by urea-assisted pyrolysis of ZIF-67.[169] The formation of Co–N_x species enhanced electrocatalytic activity, enabling a low LOD of 32.4 nM and a wide linear range of 50 nM–50 mM (Fig. 16e). More importantly, a portable Co–N/CNT-based screen-printed sensor was employed to quickly detect H_2O_2 generated in microbial fuel cells in 40 seconds using only 50 μL solution. The sensor-measured concentrations were consistent with those obtained by the standard spectrophotometric approach, demonstrating the potential of such catalysts in sensor applications (Fig. 16f). Hu *et al.* also explored controllably dispersed atomic Co–N sites on nitrogen-doped carbon nanosheets by a dual-template (ZIF and g-C_3N_4) method.[171] The catalyst with 4% Co (>4% Co would aggregate into NPs) achieved a high sensitivity of 605.50 μA mM^{-1} cm^{-2} for 0.5×10^{-3}–1×10^{-1} M H_2O_2 and a low LOD of 6.18×10^{-9} M.

Cu SAs also prefer the two-electron pathway and have a large overpotential and high O_2 activation energy during $O_2 \rightarrow H_2O_2$. Thus Cu SAs have a stronger potential to avoid interference

Table 3 Comparison of the sensing properties of different SAC-based liquid sensors

Type of analytes	Analytes	Catalysts	Active sites	Active metal loading	Type of sensor	LOD[a] (μM)	Linear range[a] (μM)	Sensitivity (μA mM^{-1} cm^{-2})	Ref.
ROS	H_2O_2	Fe/NOMC	Fe–N–C	—	EC	5	8–23 000	709.63	166
		Fe–SASC/G	Fe–N	0.51 at%	EC	0.02	10–920	3214.28	167
		CoSAN/C@rGO	Co–N$_x$–C	0.78 at%	EC	0.1	0.25–50 000	743.3	168
		Co–N/CNT	Co–N$_x$	0.48 wt%	EC	32.4 × 10^{-3}	0.05–50 000	568.47	169
		Co–N–C SANs	Co–N–C	—	EC	0.13	0.3–10 000	943.9	170
		Co(4%)–N/CNS	Co–N$_x$	0.35 at%	EC	6.18 × 10^{-3}	1–500 500–10 000	468.95 605.50	171
		Mn–N/C	Mn–N–C	1 at%	EC	0.036	0.1–50 000	205.7	78
		Cu–N/C	Cu–N–C	1 at%	EC	0.047	0.5–50 000	2992.1	78
		Cu–N–C	Cu–N–C	0.17 at%	CM	0.12	0.1–20	—	173
		2D MoSe$_2$	Mo–Se	—	EC	12.6 × 10^{-3}	20–100 000	0.02–0.2 mM: 659.80 0.2–100 mM: 614.98	175
		Fe–SASC/NW	Fe–N$_x$	2.05 wt%	CM	46.35 × 10^{-3}	0.0005–500 000	—	214
		IIM-Fe–SASC	Fe–N$_x$	2.12 wt%	CM	—	250–5000	—	215
		Fe,N–C-800	Fe–N–C	0.74 at%	CM	4.23	100–628	—	216
		SA–Pt/g-C$_3$N$_4$–K	Pt–N$_4$	3 wt%	CM	1	5–500	—	217
Ions	Hg^{2+}	Fe–N–C SAE	Fe–N–C	—	EC	1 × 10^{-3}	0.03–3	−30 mV per decade	39
		Fe–SAC	Fe–N$_x$	1.43 wt%	ECL	0.00013	0.00001–0.0005	—	65
		Fe–N/S–C	Fe–N–S–C	—	CM	0.00017	0.001–10	—	179
	Cr^{6+}	SA–Fe/NG	Fe–N–C	0.36 wt%	CM	0.003	0.03–3	—	181
		SACe–N–C	Ce–N–C	—	CM	1.8 (93.65 ng mL^{-1})	9.6–96 (0.5–5 μg mL^{-1})	—	182
	Fe^{3+}	SACe–N–C	Ce–N–C	—	CM	0.62 (34.72 ng mL^{-1})	4.5–27 (0.25–1.5 μg mL^{-1})	—	182
	Al^{3+}	SACe–N–C	Ce–N–C	—	FS	0.848 (22.89 ng mL^{-1})	0.18–0.926 (5–25 μg mL^{-1})	—	183
	PO$_4^{3-}$	SA Fe–CDs	Fe–O/N	—	CM FS	13.5 2.74	15.6–250 3.90–125	— —	184
	As^{3+}	Pt$_1$/MoS$_2$	Pt–S	4%	EC	0.000667 (0.05 ppb)	0.000667–0.1068 (0.05–8 ppb)	3.31 μA ppb^{-1}	73
		Co SAC	Co–N$_2$C$_2$	2.63 wt%	EC	0.000267 (0.02 ppb)	0.0013–0.133 (0.1–10 ppb)	11.44 μA ppb^{-1}	76
		FeN$_2$C$_2$	Fe–N$_2$C$_2$	1.85 wt%	EC	0.00053 (0.04 ppb)	0.027–0.147 (2–11 ppb)	17.98 μA mM^{-1} (0.24 μA ppb^{-1})	77
		FeN$_3$P	Fe–N$_3$P	1.02 wt%	EC	0.00013 (0.01 ppb)	0.013–0.147 (1–11 ppb)	292.2 μA mM^{-1} (3.90 μA ppb^{-1})	
	Pb^{2+}	Mn–MoS$_2$	Mn–S	0.92 wt%	EC	—	—	133.90 μA μM^{-1}	187
		Mn/g-C$_3$N$_4$	Mn–N$_4$–C	3.06 wt%	EC	0.01	0.1–0.8	2 714 470	188
Organic pollutants	Methyl parathion (belongs to OP)	Fe SAs/N$_5$–pC-4	Fe–N$_5$	0.54 wt%	CM	0.0023 (0.0006 μg mL^{-1})	0.004–76 (0.001–20 μg mL^{-1})	—	192
	Malathion (belongs to OP)	Fe–N/C	Fe–N–C	0.83 wt%	CM	Analytical: 0.00042 Phone RGB: 0.001	Analytical: 0.0005–0.01 Phone RGB: 0.001–0.01	—	194
	Paraoxon-ethyl (belongs to OP)	FeSNC	Fe–N$_3$S$_1$	1.3 wt%	CM	0.0030 (0.87 ng mL^{-1})	0.003–0.3 (1–100 ng mL^{-1})	—	196
		Fe–N–C	Fe–N$_x$	0.96 at%	CM	0.044 (0.012 μg mL^{-1})	0.11–7.3 (0.03–2 μg mL^{-1})	—	218
					PT	0.047 (0.013 μg mL^{-1})	0.11–7.3 (0.03–2 μg mL^{-1})	—	
	Omethoate (belongs to OP)	SACe–N–C	Ce–N–C	—	CM	0.2618 (55.83 ng mL^{-1})	0.469–3.274 (100–700 μg mL^{-1})	—	197
	Chlorpyrifos (belongs to OP)	PdSA/TiO$_2$	Pd–O	0.53 wt%	PC	0.00003 (0.01 ng mL^{-1})	0.00009–30 000 (0.03–10 000 000 ng mL^{-1})	—	72
	OP	Boron-doped Fe–N–C	Fe–N$_4$–2B	0.6 wt%	CM	2.19 ng mL^{-1}	8–1000 ng mL^{-1}	—	195

Table 3 (*continued*)

Type of analytes	Analytes	Catalysts	Active sites	Active metal loading	Type of sensor	LOD^a (µM)	Linear range^a (µM)	Sensitivity (µA mM^{-1} cm^{-2})	Ref.
		Ir SASC	Ir–N$_x$	—	EC	0.17 ng mL^{-1}	0.5–500 ng mL^{-1}	—	202
		Fe SACs/ Cu$_2$O/ Ti$_3$C$_2$T$_x$	Fe	3%	PEC	0.08 ng mL^{-1}	0.5–600 ng mL^{-1}	—	203
		Cu–N–C SACs	Cu–N–C	∼5.1 wt%	CM	0.60 ng mL^{-1}	1–300 ng mL^{-1}	—	219
	2,4-Dichlorophenoxy-acetic acid	Fe–SASC	Fe–N$_x$	2.45 wt%	CM	0.0037 (0.82 ng mL^{-1})	0.0045–1.13 (1–250 ng mL^{-1})	—	198
	Carbendazim	CSACs	Co	4.69 wt%	LS	0.0000094 (1.8 pg mL^{-1})	0.00005–0.26 (0.01–50 ng mL^{-1})^b	—	199
		Co SADCs	Co	5.55 wt%	LS	0.0000017 (0.33 pg mL^{-1})	0.000005–0.13 (0.001–25 ng mL^{-1})^b	—	200
	Imidacloprid	Co$_3$N@Co SACs	Co–O$_4$, Co$_3$–N	3.08 wt%	LS	0.0000066 (1.7 pg mL^{-1})	0.0002–0.039 (0.05–10 ng mL^{-1})	—	201
	Nitrobenzene	SANb-BCN/ GCE	Nb	—	EC	0.7	2–100 100–600	—	206
	p-Phenylenediamine	ZnBNC	Zn–N$_4$B$_2$	—	CM	0.1	0.3–10	—	207
		Fe–SAs@FNC	Fe–N	—	CM	0.07	0.2–50	—	208
	Hydroquinone	SA–Pt/CN	Pt	0.12 wt%	CM	0.07	1–10	—	209
		Mo SAs/ NPO–C	Mo–O	0.2 wt%	EC	0.005	0.02–200	—	210
	Bisphenol A	SAFe	Fe	1.18 at%	RRS	0.00008	0.0001–0.004	—	211
		SAFe	Fe	1.18 at%	SERS	0.00003	0.0001–0.012	—	211
	PFOS	Cu–CN	Cu	0.96 wt%	CM	0.0149	0.07–3	—	213
	Phenol	Fe$_1$@CN-20	Fe–N	2.9 wt%	CM	2.6	160–532	—	220
	4–Chlorophenol	Fe$_1$@CN-20	Fe–N	2.9 wt%	CM	3.3	3.9–391	—	220
	2,4-Dichlorophenol	Fe$_1$@CN-20	Fe–N	2.9 wt%	CM	1.3	30–184	—	220
	2,6-Dimethoxy-phenol	Fe$_1$@CN-20	Fe–N	2.9 wt%	CM	1.2	32–260	—	220
	Catechol	Fe$_1$@CN-20	Fe–N	2.9 wt%	CM	2.3	45–182	—	220

List of abbreviations. CM: colourimetric, CNSs: carbon nanosheets, EC: electrochemical, Fe/NOMC: N-doped mesoporous carbon by atomically dispersed Fe–N, Fe–SASC/G: iron single atomic site catalyst anchored on 2-D N-doping graphene, Fe SAs/N$_5$-pC-4: SACs with Fe–N$_5$ confined by hierarchically porous carbon nanoframes, Fer: ferrocene, FS: fluorescent, IIM: ion-imprinting method, LS: luminescent, NW: nanowire, OP: organophosphorus pesticide, PC: photocatalytic, PEC: photoelectrochemical, PT: photothermal, RRS: Rayleigh scattering signals, SAE: single atom enzyme, SASC: single-atomic site catalysts, and SERS: surface-enhanced Raman scattering, ^{a} The units and data in the reference are noted in brackets when there are unit conversions. ^{b} Detection range.

from oxygen reduction reactions.[78,172,173] Mao's group developed SACs with Cu SAs anchored on mesoporous graphitic carbon nitride (Cu$_1$/C$_3$N$_4$).[172] The adsorption-edge of the sample in the XANES spectrum (Fig. 17a) is between Cu foil and CuO, indicating the 0– +2 valence of the Cu atom, attributed to the strong interaction between Cu and C$_3$N$_4$. The Fourier transformed extended X-ray absorption fine structure (FT-EXAFS) spectra (Fig. 17b) show only one primary peak at 1.5 Å similar to that of copper phthalocyanine (CuPc). Further fitting indicates that the coordination number of Cu in Cu$_1$/C$_3$N$_4$ is 2.2, suggesting a Cu–N$_2$ structure. The Cu$_1$/C$_3$N$_4$ system achieves high sensitivity and selectivity (Fig. 17c and d) due to the two-electron preferred pathway of Cu–N$_2$ sites with the neighbouring C atom on C$_3$N$_4$. For the H$_2$O$_2$ reduction reaction, the final •OH$_{ad}$ desorption step on the C atom is considered the rate-determining step because of its higher free energy (1.31 eV), which is lower than that of the oxygen reduction reaction (1.44 eV).

In addition to forming TM–N bonds on carbonaceous substrates, catalytically active SAs can also be anchored on SMOs for H$_2$O$_2$ sensing. Zhang's group doped Au onto the oxygen vacancies provided by CeO$_2$ nanorods, achieving an ultra-sensitive (LOD = 1.4 nM) detection of H$_2$O$_2$.[36] The anchored Au promotes the Ce^{3+} formation and facilitates the migration of lattice oxygen from the crystal to the surface, resulting in more oxygen vacancies and more adsorption sites for H$_2$O$_2$. In addition to SMOs, 2D transition metal dichalcogenides are an appealing candidate for SAC-based sensor devices due to their atomic thickness, high carrier mobility, fast charge transfer, and intrinsic spin-valley couplings.[174] Luo *et al.* etched MoSe$_2$ nanosheets with Ar plasma to produce Se vacancies and doped them with N atoms through a N$_2$ plasma treatment, achieving a low LOD (12.6 nM), fast response (2 s) for H$_2$O$_2$ detection in a wide operational pH range of 1–13.[175] The bandgap of MoSe$_2$ reduces with increasing Se vacancy concentration and edge active surfaces following N atom doping, which can strengthen the binding to •OH and promote the electron transfer kinetics.

5.2.2 Ion sensing. Detecting ions, especially heavy metal ions, is one of the major concerns in research for aquatic sensors, as these ions are highly toxic at low concentrations
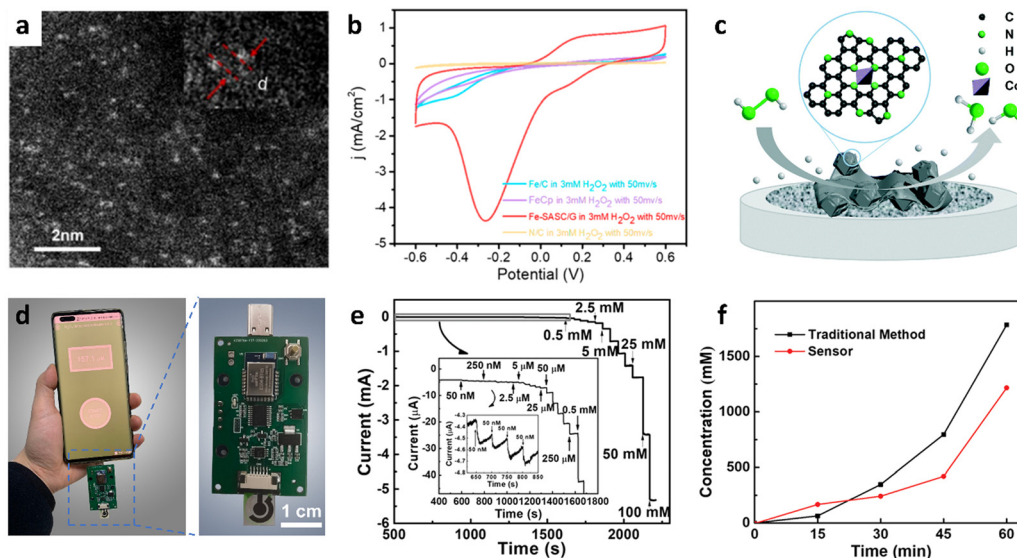
Fig. 16 (a) HAADF-STEM image of Fe SA anchored N-doping graphene (Fe–SASC/G). (b) CVs of electrodes modified by Fe–SASC/G and reference materials in 3 mM H_2O_2. Reproduced from ref. 167 with permission from American Chemical Society, copyright 2022. (c) Proposed H_2O_2 sensing mechanism for the atomic Co–N_x–C site anchored carbon-modified sensor. (d) Photographs of a portable H_2O_2 sensor device, including a screen-printed electrode, an amplifier, voltage stabilizing circuits, a micro control unit and a bluetooth communication module. Reproduced from ref. 168 with permission from the Royal Society of Chemistry, copyright 2022. (e) Chronoamperometric responses of the Co–N/CNT sensor on adding various amounts of H_2O_2 at −0.7 V vs. Ag/AgCl. (f) H_2O_2 generation by a microbial fuel cell measured by the traditional spectrophotometric method and Co–N/CNT SPE sensor at 0–60 min. Reproduced from ref. 169 with permission from Wiley-VHC, copyright 2019.
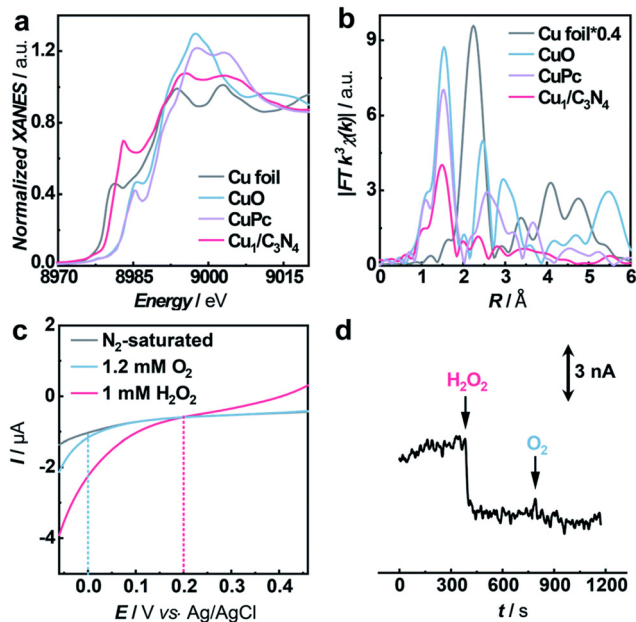

Fig. 17 (a) Normalized XANES spectra and (b) FT-EXAFS spectra at the Cu K-edge of Cu_1/C_3N_4 and reference samples. (c) LSVs of the Cu SAC-based electrode in artificial cerebrospinal fluid (aCSF) with 1.2 mM O_2 or 1 mM H_2O_2 under an atmosphere of N_2. Scan rate: 50 mV s^{-1}. (d) Amperometric response of the Cu SACs-based electrode when adding 5 μM H_2O_2 and 50 μM O_2 in aCSF. Applied potential: 0 V vs Ag/AgCl. Reproduced from ref. 172 with permission from the Royal Society of Chemistry, copyright 2021.

(nM to μM level). For example, non-degradable heavy metals are persistent environmental pollutants that can easily accumulate in living organisms, and are highly toxic and damage the nervous system, gastrointestinal system and essential organs and even cause cancer.[176–178] Therefore, developing a highly sensitive, rapid response sensing method for accurately determining ions is essential for ecological, environmental, and health applications. Similar to H_2O_2 sensing, SAs are usually anchored on nitrogen-doped carbon and MOF substrates via TM–N bonds for ion sensing, where TMs includes Fe, Ni, Zn and Mn have been reported.

Mercury ions (Hg^{2+}) can transform into methylmercury and accumulate in the body, causing irreparable harm to organs including the endocrine, liver, kidney, brain, and neurological systems. The World Health Organization (WHO) and the United States EPA have established tolerable limits for inorganic Hg^{2+} in drinking water, which are 30.0 nM and 10.0 nM, respectively. Yao et al. synthesized Fe–N–C SACs by packing iron phthalein cyanide molecules into ZIF-8 cages, followed by high-temperature pyrolysis and H_2SO_4 treatment.[39] The Fe–N–C SA-modified solution-gated graphene transistor (SGGT) can rapidly detect Hg^{2+} down to 1 nM within 2 s (Fig. 18a and b). The catalytic Fe–N_4 sites can boost the electron transfer of Hg^{2+}, resulting in amplified signals. In addition, the strong chelation between Hg^{2+} and N embedded in Fe SACs enables a high Hg^{2+} selectivity (almost no interference from 14 metal ions as shown in Fig. 18c).

The colourimetric method is also practical for Hg^{2+} sensing. Zhao's group constructed an "on–off–on" colourimetric sensor based on Fe–N/S–C SACs for colourimetric Hg^{2+} sensing with an ultralow LOD of 0.17 nM (Fig. 18d and e).[179] The appropriate introduction of S to Fe–N–C sites can prevent the formation of
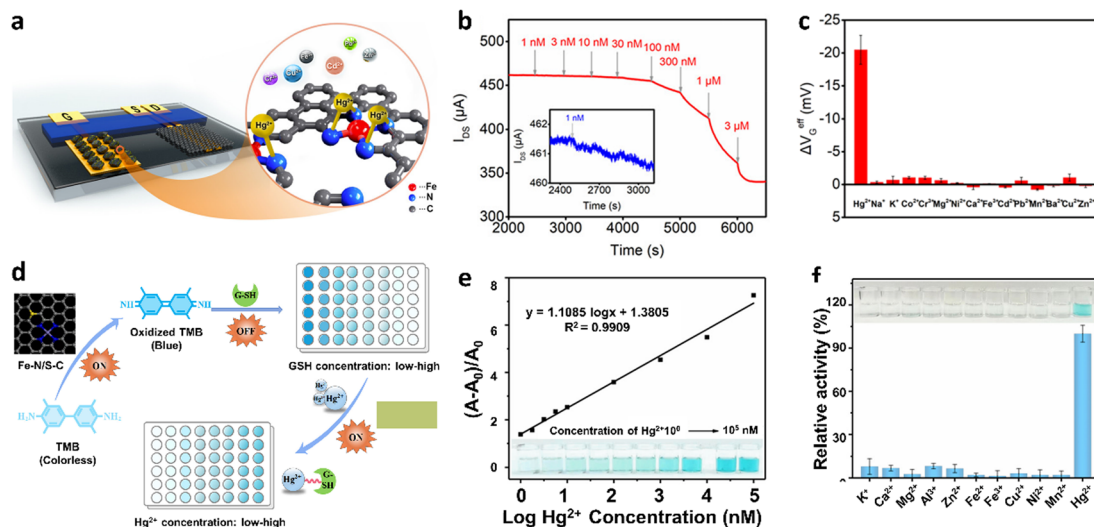
Fig. 18 (a) Schematic illustration of an SGGT based on the Fe−N−C SAC/Au-modified gate electrode for Hg^{2+} detection. G, S, and D are denoted to the gate, source and drain electrode, respectively. (b) Chronoamperometric responses of the Fe−N−C SAC/Au-modified gate electrode SGGT to the 1– 3000 nM Hg^{2+} in 0.01 M Tris-HCl solution at V_G = 0.7 V and V_{DS} = 0.05 V. (c) Selectivity of the Fe−N−C SAC/Au-modified gate electrode SGGT. Hg^{2+} concentration: 300 nM, other analytes: 1 μM. Reproduced from ref. 39 with permission from American Chemical Society, copyright 2020. (d) Schematic illustration of a colourimetric sensor based on Fe−N/S−C SAC for simultaneous detection of GSH and Hg^{2+}. (e) Sensing response of the Fe−N/S−C− TMB-GSH system to 1–10^5 nM Hg^{2+}. Inset: the corresponding photographs. (f) Selectivity of the Fe−N/S−C−TMB-GSH system towards Hg^{2+} (1 μM) and other metal ions (100 μM). Inset: The corresponding photographs. Reproduced from ref. 179 with permission from Elsevier B. V., copyright 2022.

iron carbide, promoting the growth of porous carbon and improve the SSA.[180] In the colourimetric sensing system, Fe– N/S–C SACs with oxidase-mimicking activity can oxidize TMB into blue oxTMB ("on"), and the reduced glutathione (GSH) can prevent TMB from oxidizing ("off"). When Hg^{2+} exists in the liquid, the blue colour can return ("on") as a result of the strong specific affinity between the sulfhydryl groups of GSH and Hg^{2+}, which shows strong selectivity for Hg^{2+} over other cations (Fig. 18f). More importantly, the colourimetric RGB value can be rapidly analysed using a smartphone, showing a good linear response from 1 nM to 10 μM for Hg^{2+}.

In the food industry, it is important to develop a fast and portable method for Fe^{3+} and Cr^{6+} detection to avoid excessive intake. Following a similar "on" and "off" colourimetric sensing mechanism, Zheng's group synthesized Fe−N−C SACs by anchoring Fe SAs on NG for Cr^{6+} sensing with a low LOD of 3 nM and a linearity range of 0.03–3 μM.[181] During the sensing process, 8-hydroxyquinoline was preadded to the solution to specifically interact with Cr^{6+} via chelation. Cheng's group found that both Fe^{3+} and Cr^{6+} could significantly accelerate the electron transfer between Ce^{3+} and Ce^{4+}, enabling the dual detection within a Ce−N−C SACs-based sensor.[182] For Fe^{3+}, the LOD was 34.72 ng mL^{-1} and the linearity range was 0.25– 1.5 μg mL^{-1}. For Cr^{6+}, the LOD was 93.65 ng mL^{-1} and the linearity range was 0.5–5 μg mL^{-1}. Due to their different redox properties, Fe^{3+} and Cr^{6+} cause the optimized TMB solution to turn blue at 30 s and 60 s, respectively, and the colour fades only in the presence of Fe^{3+}, allowing for the specification for Fe^{3+} and Cr^{6+} detection.

Al^{3+} is widely used during food production as a curing and swelling agent, stabilizer, anti-caking agent, and dyeing agent.

However, its excessive accumulation can lead to metabolic disorders such as Alzheimer's and Parkinson's disease. Cheng's group also prepared Ce−N−C SACs to quickly detect Al^{3+} based on fluorescence sensing.[183] As Al^{3+} can combine with the O atom in the Ce−N−C SAC to cause aggregation, an increasing Al^{3+} concentration would reduce the fluorescence intensity (substrate 4-methylumbellione phosphate disodium salt can produce blue fluorescence at 430 nm), showing a linear relationship in the range of 5–25 μg mL^{-1} and a LOD of 22.89 ng mL^{-1}.

In a water environment, excess phosphate ions (PO_4^{3-}) can lead to water eutrophication and a hazardous ecosystem. As sensors based on a single detection mechanism may be sensitive to interference producing inaccurate results and limited in their use scenarios, Lin's group proposed SA Fe doped carbon dots (SA Fe−CDs) for the dual-mode colourimetric and fluorometric detection of PO_4^{3-}.[184] The carbon dots provide tunable fluorescence and serve as large-SSA supports for oxidase-mimetic SA Fe loading to oxidize TMB. The oxTMB can then quench the PL of carbon dots. PO_4^{3-} can specifically interact with Fe active sites to form Fe−O−P coordination bonds, inhibiting the TMB colouration and recovering the PL. Based on this principle, the SA Fe−CDs realized a low LOD of 13.5 μM for PO_4^{3-} in a colourimetric mode and 2.74 μM in a fluorescence mode.

Arsenic pollution in natural water is a global problem, with millions of people drinking water contaminated with high levels of As^{3+}. Arsenic in compounds appears in various multi-valent states, including 3, 0, +3, and +5, and As^{3+} is the most toxic form, being hundred times more toxic than others.[185] Huang's group developed Pt SAs anchored on MoS_2 with

different loadings (1%, 4% and 12%) to catalyse the determination of As^{3+} (Fig. 19a).[73] The 4% Pt loading has the highest sensitivity (3.31 μA ppb^{-1}) due to higher SA loading compared to 1% Pt and the absence of Pt NP gathering observed in 12% Pt (Fig. 19b). XPS and DFT calculation reveal that Pt SAs would activate the nearby S atoms to transfer electrons into H_3AsO_3 via O and As atoms, respectively. This can decrease the energy required for the rate-limiting step of As^{3+} reduction to accelerate the reaction (Fig. 19c). In addition to noble metal SAs, Co SACs have been fabricated by pyrolysis of Zn doped-ZIF-67 powders as a precursor for As^{3+} sensing.[76] Compared with Co NPs, the Co SACs with the same mass of Co atoms shows a 14 times higher peak current (sensitivity of 11.44 μA ppb^{-1}). XANES spectra reveal that a large number of H_3AsO_3 molecules are adsorbed on Co SAs with CoN_2C_2 coordination by forming Co–O bonds, decreasing the energy barrier and favouring the breakage of As–O bonds for H_3AsO_3 reduction. DFT calculation shows that the dissociation energy of As–O bond breakage, which has been demonstrated to be the rate-limiting step of the H_3AsO_3 reduction process, is smaller on Co SACs (0.28 eV) than that of Co NPs (1.40 eV).

Another serious problem for the As^{3+} detection reliability and accuracy in water quality analysis is the interference of Cu^{2+}. To overcome this problem, the same group fabricated Fe SACs with a FeN_3P coordination structure, achieving a high sensitivity of 3.90 μA ppb^{-1} and a low LOD of 0.01 ppb (Fig. 19e).[77] Compared with FeN_2C_2, H_3AsO_3 prefers to be reduced by FeN_3P due to the strong Fe–As and P–O affinities, which enhances the response signals (Fig. 19d and e). Meanwhile, SEM images and DFT calculations demonstrated that Cu^{2+} does not compete with As^{3+} for active Fe SA sites on FeN_3P, successfully avoiding the interference of Cu^{2+} (Fig. 19f–m).

Pb^{2+} has been identified as one of the ten chemicals of primary public health concern by the WHO. The WHO and the United States EPA have established a guideline value of 0.01 mg L^{-1} for Pb^{2+} in drinking water.[186] Huang et al. substituted Mo sites in MoS_2 nanosheets with Mn atoms, realizing ultrasensitive electrochemical detection of Pb^{2+} (sensitivity of 133.90 μA μM^{-1}).[187] The electron donor Mn atoms destabilized the MoS_2 lattice, resulting in sulphur vacancy (V_S) formation, which is supposed to enhance the charge carrier density and adsorption capability of MoS_2. In addition to MoS_2, Mn atoms can be anchored in g-C_3N_4 via simple one-step calcination.[188] The anchored Mn atoms will serve as strong electron donors to modulate the electronic structure distribution of the N atoms, offering plenty of negatively charged sites for catalytic reactions. In this way, the Mn/g-C_3N_4 catalyst achieves highly sensitive detection of Pb^{2+} with a LOD of 0.01 μM and a sensitivity of 2714.47 μA μM^{-1} cm^{-2}, which can be applied to real water samples.

5.2.3 Organic pollutant sensing. Organic pollutants in liquid, including pesticides, benzenes, and organofluoride have seriously harmful effects on the environment and human health.[189–191] These lipophilic chemicals may accumulate in the food chain and cause acute to chronic poisoning. Therefore, developing highly sensitive, selective and robust SAC-based sensors for long-lasting detection of organic pollutants in harsh environments is essential for applications.

Pesticides, including organophosphorus (methyl parathion, malathion, paraoxon-ethyl, omethoate, methamidophos, and chlorpyrifos), nicotinamide (imidacloprid), benzimidazole (carbendazim), carbamate (carbofuran) chemicals, etc., have been extensively studied in SAC sensing due to their wide application and severe health risks. To achieve selective
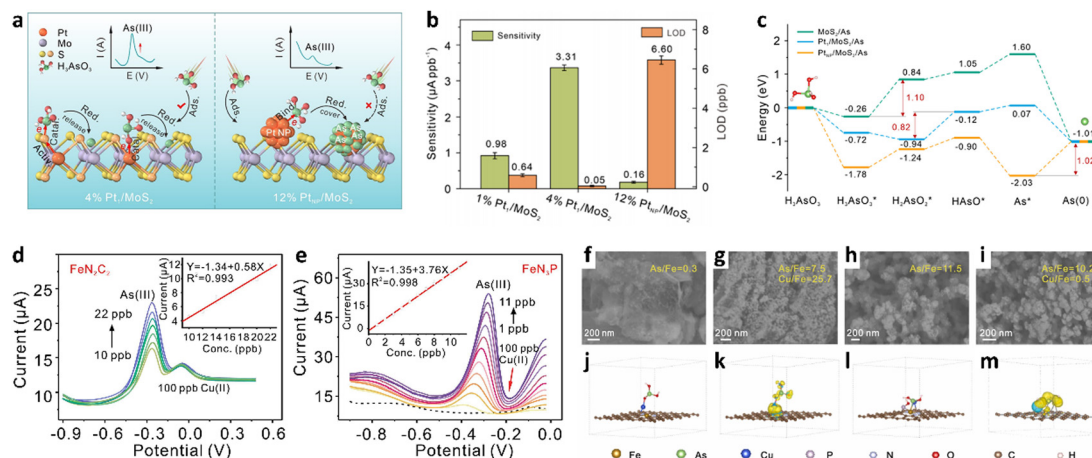

Fig. 19 (a) The proposed sensing mechanism of 4% Pt_1/MoS_2 and 12% PtNP/MoS_2 to As(III). (b) Sensitivities and LODs of 1 and 4% Pt_1/MoS_2 and 12% PtNP/MoS_2. (c) The relative reaction energy of intermediates produced during the reduction of H_3AsO_3 on Pt_1/MoS_2 and reference samples. Reproduced from ref. 73 with permission from American Chemical Society, copyright 2021. The SWASV current signals of As(III) in the presence of 100 ppb Cu(II) via (d) FeN_2C_2 and (e) FeN_3P. Insets: correlation between current values and As(III) or Cu(II) concentrations with linear correction. SEM images of FeN_2C_2 after (f) 20 ppm As(III) deposition and (g) 20 ppm As(III) and 200 ppm Cu(II) co-deposition. SEM images of FeN_3P after (h) 20 ppm As(III) deposition and (i) 20 ppm As(III) and 200 ppm Cu(II) co-deposition. DFT-calculated configurations of As(III) and Cu(II) co-adsorbed on (j) FeN_2C_2 and (l) FeN_3P. (k and m) The charge density in (j and l), where the yellow region indicates electron aggregation, and the cyan region indicates electron dissipation. Reproduced from ref. 77 with permission from Elsevier B. V., copyright 2022.

detection of pesticides, cascade sensing is frequently employed.[192] First, SACs stimulate the ORR to accelerate the production of ROS and enhance the amperometric, colourimetric, or luminescence emission signals. Then certain enzymes and corresponding substrates are added, producing hydrolysate that can reduce the corresponding signals. When pesticide residues exist, they can inhibit the activity of certain enzymes and restrict the production of hydrolysate, resulting in the recovery of the corresponding signals.

Fe–NC SACs with atom-scattered FeN$_4$ sites have been shown to have enzyme-like activity. Experimental and theoretical results reveal that the activity of FeN$_4$ is higher than that of CoN$_4$ and ZnN$_4$.[193] Ge *et al.* synthesized Fe–N/C SACs with Fe–N$_x$ *via* sacrificial templates and cascaded the catalytic reactions with acid phosphatase in a TMB containing solution to detect malathion with an ultralow LOD of 0.42 nM.[194] The SACs could directly oxidize colourless TMB to blue-coloured oxTMB by producing ascorbic acid instead of H$_2$O$_2$. The Fe–N/C SACs also respond to various organophosphorus pesticides, but only weakly to ions and carbamate or pyrethroid pesticides. In addition, a colourimetric paper sensor with Fe–N/C and TMB was developed to show the colour change with the addition of malathion. By using a colour recognizer APP on a smartphone, the colourimetric data can be identified in the RGB value, where a linear relationship between the malathion concentration and the (G + B)/2R value can be built, allowing for convenient and reliable detection of malathion (Fig. 20a and b). The paper sensor can also be stored in a dry environment at 4 °C for 20 days. To further enhance the activity of Fe–N$_4$, heteroatoms (B, S) are doped into the structure. Guo and Zhu's group found that doping boron atoms into Fe–N–C SACs could modify the electronic structure of Fe–N$_4$ sites and reduce the energy barrier created by reaction intermediates.[195] By cascading the catalytic reaction of FeBNC SACs and acetylcholinesterase (AChE), the proposed sensor achieved a LOD of 2.19 ng mL^{-1} for paraoxon-ethyl. A year later, Guo's group discovered that S atoms with a larger atomic radius could modify the electronic structure of the central metal by altering both the geometry of the ligand heteroatoms and the electronegativity difference of the atoms, further lowering the energy barrier formed by the active intermediates and bringing down the LOD for paraoxon-ethyl to 0.87 ng mL^{-1}.[196]
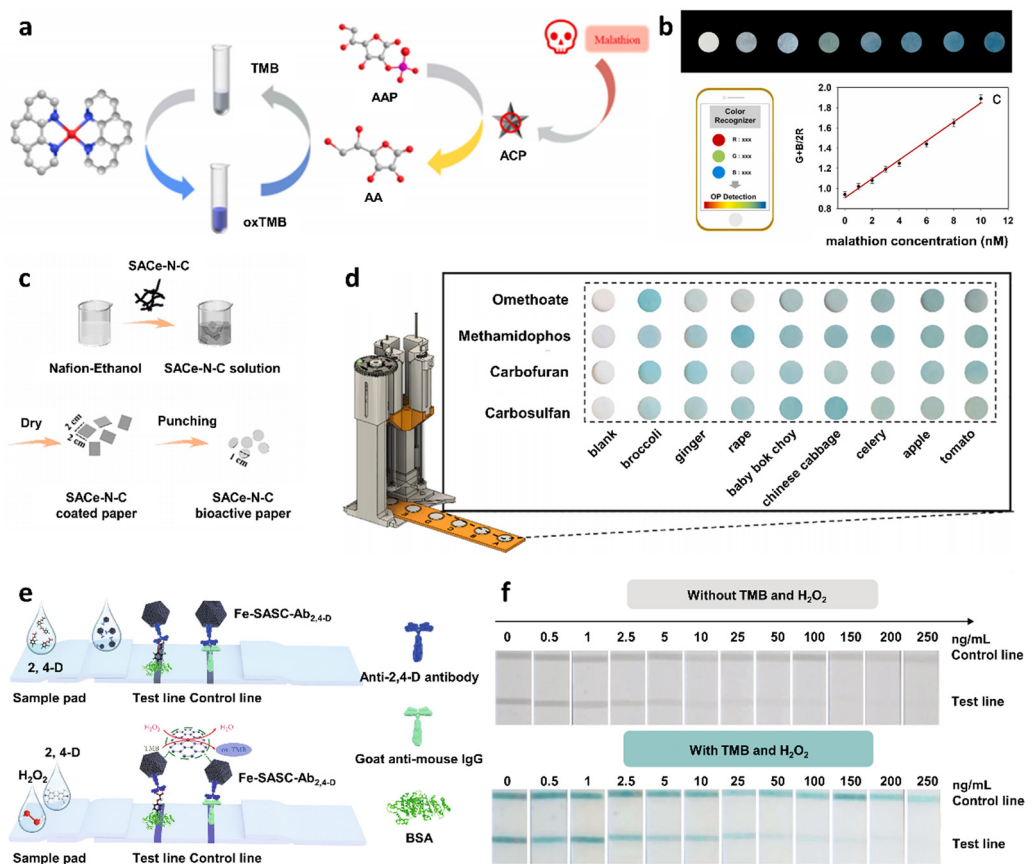

Fig. 20 (a) Mechanism of Fe–N/C SACs for colourimetric malathion sensing. (b) Using a colour recognizer APP on a smartphone to recognize 0–10 nM malathion *via* RGB data driven from photographs of the colourimetric paper sensor. Top: photographs of the colourimetric paper sensor. Bottom right: the linear relationship between malathion concentration and the (G + B)/2R value. Reproduced from ref. 194 with permission from Elsevier B. V., copyright 2022. (c) Preparation process and (d) practical photographs of Ce–N–C SAC-based paper for detecting OP residues. Reproduced from ref. 197 with permission from Elsevier Ltd., copyright 2022. (e) Method schematics and (f) testing results in human urine of Fe SACs enhanced LFIA for 2,4-D detection. Reproduced from ref. 198 with permission from American Association for the Advancement of Science, copyright 2022.

In order to facilitate on-site detection of pesticide residues, Cheng's group fabricated a bioactive paper with synthesized Ce–N–C SACs rather than a liquid phase one.[197] By constructing a 3D printed platform with 4 syringes providing AChE, acetylcholine (ACh), TMB, and H_2O_2 solutions, a portable approach was developed to monitor pesticide residues in fruits and vegetables within 30 min using SAC-based paper sensors (Fig. 20c and d). The Ce–N–C SAC-based paper showed a high sensitivity for omethoate, methamidophos, carbofuran, and carbosulfan with LODs of 55.83, 71.51, 81.81, and 74.98 ng mL^{-1}, respectively. To build a portable and rapid point-of-care detection platform for the 2,4-dichlorophenoxyacetic acid (2,4-D, a herbicide) exposure evaluation, Lin's group designed a Fe SAC to enhance the performance of lateral flow immunoassay (LFIA).[198] In the presence of 2,4-D, it would specifically interact with the Fe SAs tagged 2,4-D antibodies to prevent them from attaching to the pre-adsorbed haptens (BSA) on the test lines, resulting in a fading label (Fig. 20e). Based on this mechanism, a fast, visible, and selective 2,4-D detection was accomplished in a human urine sample with a low LOD of 0.93 ng mL^{-1} and a linear detection range of 1–200 ng mL^{-1} (Fig. 20f). Different from those colourimetric cascade sensing induced by ROS generation, such antibody tagged SACs can also amplify specific luminescence signals to selectively detect pesticides.[199] Based on the luminescence cascade sensing mechanism, Fu's group used MOFs with large SSAs, abundant active sites, and high stability as a substrate to support Co SACs, realizing the lowest LOD of 0.33 pg mL^{-1} for carbendazim.[200] They further found that atomic clusters can enhance the amount of catalytic active sites by introducing dual atomic-scale sites to accelerate the H_2O_2 decomposition into singlet oxygen.[201] By synthesizing Co_3N cluster-assisted Co SACs which contain $Co–O_4$ and $Co_3–N$ as coordination environments, the luminescence signals are significantly enhanced by 2155.0 times, approximately 20.9 times higher than those of the pure Co SACs.

Compared to cascade colourimetric and luminescence sensing, electro/photo-catalysis also shows potential in pesticide sensing. The difference from colourimetric/luminescent cascade sensing is that the ORR on SACs was detected *via* electrochemical V–I signals rather than the colour/luminescence development process of the substrates. Zhu's group prepared an Ir SAC through a template-sacrificed strategy and combined it with AChE to produce an electrochemical sensor.[202] In this way, the electrochemical cascade sensing by Ir SACs achieved a lower LOD (0.17 ng mL^{-1}) for organophosphorus pesticides. More recently, the same group integrated Fe SACs on the surface of $Cu_2O/Ti_3C_2T_x$ semiconductors for photoelectrochemical sensing.[203] Fe SACs would significantly accelerate the ORR on the Cu_2O surface and reduce interfacial recombination of photoexcited electrons. Besides, Fe SACs would accelerate the oxidation of 4-chloro-1-naphthol to generate insoluble benzo-4-chlorohexadienone precipitates on the photoelectrode surface, reducing the photoelectrochemical signal. Consequently, the Fe SACs/$Cu_2O/Ti_3C_2T_x$-based sensor exhibited a lower LOD for OPs of 0.08 ng mL^{-1}. Without any complex pre-processing procedures (*e.g.*, cascading), Guo's group constructed a less

time-consuming and direct photocatalytic sensing platform for chlorpyrifos residues.[72] Owning to the high-density active sites of Pd SAs, the synthesized PdSA/TiO_2 catalyst shows significantly higher photocatalytic activity with the H_2 production rate (10 mol g^{-1} h^{-1}) than that of PdNP/TiO_2 (1.95 mol g^{-1} h^{-1}), although they have the similar Pd contents. As chlorpyrifos can adsorb on the electron-rich PdSA/TiO_2 (demonstrated by *in situ* XPS), they can selectively inhibit the photocatalytic activity of PdSA/TiO_2 and reduce the H_2 production rate. Therefore, the production rate of H_2 can precisely reflect the chlorpyrifos concentration, achieving an extremely low LOD of 0.01 ng mL^{-1} and a wide linear range of 0.03 ng mL^{-1}–10 mg mL^{-1}.

Benzenes, such as nitrobenzene, *p*-phenylenediamine, hydroquinone, and bisphenol A are another group of organic pollutants that are widely used as industrial raw materials but they pose a severe threat to human health once they leak into the water environment. For example, *p*-phenylenediamine, the primary ingredient in hair dyes, has the potential to cause allergic reactions.[189] Long-term exposure to bisphenol A is linked to various female disorders, such as polycystic ovary syndrome.[204,205] Therefore, the highly sensitive and selective detection of benzenes is desperately needed in the water treatment industry. SAs with atomically dispersed M–N$_x$ active sites are widely used for sensing benzenes, but their activity is still limited. The additional heteroatom (B, P and F) doping strategy effectively controls the coordination environments, thereby improving the sensitivity and selectivity. Hu's group found that anchoring the Nb atom to two B atoms and two N atoms allows the Nb SAs to be uniformly dispersed on the boron-carbon-nitrogen nanotubes (BCNs).[206] The SANb-BCNs showed a low LOD of 0.7 μM for nitrobenzene and a high selectivity (current interference <9%) in the presence of various ions and molecules with a 100-times higher concentration than that of nitrobenzene. Yang's group found that the doping of B atoms with smaller electronegativity (2.04) than the N (3.04) and C (2.55) atoms would remarkably change the electron density and improve the defects and hydrophilicity of the SACs.[207] The synthesized ZnBNC SACs shows a low LOD of 0.1 μM for *p*-phenylenediamine detection. They also found that the doping of F atoms would promote the uniformity of the SA dispersion and increase the active sites, allowing the Fe–SAs@FNC sensor to achieve a lower LOD of 0.07 μM for *p*-phenylenediamine.[208]

Hydroquinone, catechol and resorcinol are dihydroxybenzene isomers with similar structures and properties. Although electrochemical sensing of these isomers has been effective,[209] selectivity remains a challenge due to interference. Liu's group prepared four Mo-based nanostructures anchored on N, P and O co-doped carbon (NPO-C) by precisely controlling the addition of Mo precursors with a polyoxometalate-based supermolecule confinement-pyrolysis strategy (Fig. 21a–d).[210] The electrochemical sensitivity for hydroquinone follows the order: Mo SAs > Mo_2C nanodots > Mo nanoclusters > Mo_2C NPs, demonstrating the good intrinsic superiority of Mo SAs (Fig. 21e). The same class (metal or TM carbide) follows the rule that a smaller particle owns better sensing performance.
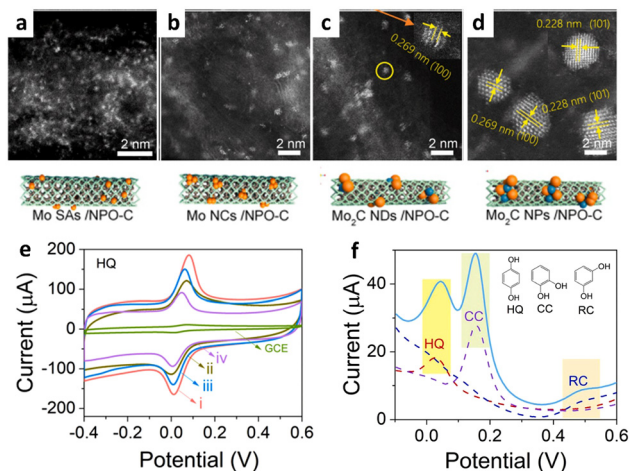
Fig. 21 HADDF-STEM images (top) and schematic structures (bottom) of (a) Mo SAs/NPO−C, (b) Mo NCs/NPO−C, (c) Mo$_2$C NDs/NPO−C, and (d) Mo$_2$C NPs/NPO−C. (e) Electrochemical impedance spectroscopy curves of (i) Mo SAs/NPO−C, (ii) Mo NCs/NPO−C, (iii) Mo$_2$C NDs/NPO−C, (iv) Mo$_2$C NPs/NPO−C, and GCE in 10 μM hydroquinone with 0.1 M PBS as electrolyte. (f) DPV curves of Mo SAs/NPO−C modified GCE when adding individual and a mixture of 10 μM hydroquinone, 20 μM resorcinol, and 10 μM catechol. Reproduced from ref. 210 with permission from Elsevier B. V., copyright 2022.

Differential pulse voltammetry (DPV) response curves reveal that Mo SAs achieve a sensitivity of up to ∼0.54 A M^{-1} cm^{-2} (18 times that of Mo$_2$C NPs/NPO−C), a low detection limit (0.005 μM) and a wide linear range (0.08–200 μM). More importantly, detecting hydroquinone among catechol and resorcinol with similar structures demonstrates high selectivity because their oxidation peaks are well separated by the potential difference (Fig. 21f).

To detect benzenes with ultra-trace concentration, Jiang's group proposed a di-mode method of resonance Rayleigh scattering (RRS) and surface-enhanced Raman scattering (SERS) based on Fe SACs to detect nM-level bisphenol A.[211] The sensing mechanism is that Fe SACs catalysed the reaction of HAuCl$_4$ and ethylene glycol to produce Au NPs with RRS and SERS effects. Introducing the bisphenol A aptamer may encapsulate and inhibit Fe SACd via intermolecular interaction, lowering the RRS and SERS signals. When there is bisphenol A in the solution, Fe SACs can be released owing to aptamer's specific binding to bisphenol A, resulting in a rebound of the RRS and SERS signals. Based on the linear relationships between the rise in RRS/SERS signals and the concentration of bisphenol A, the quantitative sensing of bisphenol A is achieved with a linear range of 0.1–4.0 nM (RRS) and 0.1–12.0 nM (SERS) and LODs of 0.08 nM and 0.03 nM, respectively.

Perfluorooctane sulfonate (PFOS), one of the most frequently used perfluorinated chemicals worldwide, has been recently reported as a persistent organic pollutant.[212] By using strong coordination and fluorophilic interaction between PFOS and atomic Cu(ı) in the Cu−CN catalyst, Liu et al. enabled colourimetric sensing of PFOS in the H$_2$O$_2$–TMB solution.[213] Owing to its high catalytic capacity and robust colloidal

stability, Cu−CN demonstrates a low LOD of 14.9 nM and a linear relationship between the PFOS concentration and the absorbance in the 0.07–3 μM range. The Cu−CN sensor was successfully employed in real water samples (from the river, lake and tap water) with 94%–114% recovery, implying a promising application.

5.3 SAC-based biosensing

Biosensing is defined as the sensing for the detection and identification of corresponding bio-related targets. Recently, demand of highly selective, sensitive, and fast sensing techniques for biomolecules in medical diagnostic, healthcare, environmental monitoring and lab-on-chip chemical analysis applications are increasing. Since the term "nanozyme" was coined in 2004, artificial nanozymes have been widely developed as a highly stable and low-cost substitute for natural enzymes in biosensing.[221] However, nanozymes also face huge challenges of complex size, composition, facet-dependent catalysis and inherent low active site density. SACs (or single-atom nanozymes) have atom-dispersed enzyme-like active sites. Compared with traditional nanozymes, SACs have significant catalytic performance due to their maximization of atom utilization efficiency and the precise definition of the active sites, revealing their potential mechanisms, and showing great potential to become the next generation of nanozymes. Here, recent advances in SACs sensors for reactive oxygen species (ROS), metabolites, neurotransmitters, nutrients, drugs and toxins, enzymes, cancer biomarkers and others are carefully discussed with their performance comparison in Table 4.

5.3.1 ROS. ROS is a high-activity chemical produced during electron transfer, including H$_2$O$_2$, $^\bullet$OH, superoxide anions (O$_2^{\bullet-}$), etc. ROS have been implicated in being responsible for significant cellular damage.[222] Excessive intracellular ROS could impair normal biological and physiological processes responsible for cancer, neurodegenerative and cardiovascular diseases.[223,224] Cellular ROS is allowed to be detected by electrochemical, electrochemiluminescence and colourimetric sensing technologies based on Pt,[217] Co,[170] Fe[225–229] and Zn/Mo[230] SACs.

The oldest known heme enzymes with pentacoordinate heme iron active sites have high sensitivity and selectivity to detect H$_2$O$_2$. However, their application is limited due to high costs and low stability. An alternative with a similar structure and activity is promising. A Fe SA site catalyst nanowire (FeSASC/NW, Fe loading of 2.05 wt%) derived from polypyrrole was synthesized via a zinc-atom-assisted method.[214] Typical chromogenic reactions with H$_2$O$_2$ using TMB, 1,2-diaminobenzene (OPD) and ABTS as substrates confirmed the peroxidase-mimicking properties of FeSASC/NW. The FeSASC/NW with Fe−N$_x$ sites owns a high catalytic activity (specific activity: 42.8 U mg^{-1}), a wide detection range (5.0×10^{-10}–0.5 M) and a low LOD (46.35×10^{-9} M), which can be applied in commercial disinfectant detection.

Fe SAs, as enzyme-like active sites, can be precisely controlled by an ion-imprinting method (IIM). The synthesized Fe−N−C SACs can improve the loading of Fe SAs to 2.12 wt%

Table 4 Comparison of the sensing properties of different SAC-based biosensors

Type of analytes	Analytes	Catalysts	Active sites	Active metal loading	Type of sensor	LOD[a] (μM)	Linear range[a] (μM)	Sensitivity (μA mM⁻¹ cm⁻²)	Ref.
ROS	H_2O_2	Co–N–C SANs	Co–N_x	0.96 at%	EC	0.13	0.3–10 000	943.9	170
		SA–Pt/g-C_3N_4–K	Pt	3 wt%	CM	1	5–500	—	217
		Fe–N–C	Fe–N_x	1.3 wt%	CM	—	500–100 000	—	225
		Fe SAs–N/C	Fe–N_x	—	EC	0.34	1–54, 54–764, 764–9664	∼604.1 ∼226.8 ∼138.3	226
		$Fe_3C@C$/Fe–N–C	Fe–N–C	0.92 at%	EC	0.26	1–6000	1225	227
		Fe–NDs	Fe	—	CM	0.072	1–25	—	228
		CNT/FeNC	Fe–N_x–C	0.2 at%	CM	0.03	0.1–100	—	229
		Zn/Mo DSAC–SMA	Zn/Mo	Zn: 1.5 wt% Mo: 7.3 wt%	CM	24.4	0–3000	—	230
	O^{2-}	sCo/NSG	Co–N	0.32 at%	EC	0.0015	0.0015–50	710.03	231
Metabolites	Glucose	Cu–N–C	Cu–N–C	0.17 at%	CM	0.58	0.1–20	—	173
		CNT/FeNC	Fe	0.2 at%	CM	20	100–10 000	—	229
		Zn/Mo DSAC–SMA	Zn/Mo	Zn: 1.5 wt% Mo: 7.3 wt%	CM	One-step: 21.4 Two-step:15.6	One-step:0–1000 Two-step:0–1800	—	230
		NCAG/Fe	Fe–N	0.95 wt%	EC FS	0.5 3.1	2–2000 20–1000	—	235
		NCA–Co	Co–N	1.2 wt%	EC	0.1	0.5–6000	—	236
		Pt_1/Ni(OH)$_2$/NG	Pt	0.36 wt%	EC	10	10–2180	220.75	237
		Pt_1/Ni_6Co_1LDHs/NG	Pt	0.61 wt%	EC	10	10–2180	273.78	238
		BiSA@Au	Bi	1.05 wt%	CM	43.2	80–1000	—	239
		PGA–Fe/CS NPs	Fe–N	1.5 at%	CM	2.4	20–600	—	240
		SA–Ir/NC	Ir–N_5	—	EC	0.0673	0.1–200[c]	—	241
	Galactose	Fe–SAC	Fe–N–C	2.32 wt%	CM	10	50–500	—	242
	UA	A–Co–NG	Co–N	1.03%	EC	0.0333 ± 0.000024	0.4–1055 1055–41 950	297.2 21.2	243
		Ru-Ala–C_3N_4	Ru–N–C	—	EC	0.17	0.5–2135	∼1.73 μA mM⁻¹	248
		FeN_5 SAC	Fe	∼1.57%	EC	0.000027	0.01–480	—	249
Neurotransmitters	DA	Fe–SAC	Fe–N_x	1.43 wt%	ECL	0.0000001	0.000001–0.001	—	65
		Co–N–C SANs	Co–N_x	0.96 at%	EC	0.04	0.06–1200	979.6	170
		Mn–MoS_2	Mn(II)/ Mn(III)	∼2.15 at%	EC	PBS, pH = 7.2:0.00005 10% serum:0.005 Artificial sweat: 0.05	PBS, pH = 7.2:0.0005–5 10% serum: 0.005–500 Artificial sweat: 0.05–500	—	246
		Ni–MoS_2	Ni	1.4 wt%	EC	0.000001	0.000001–1000	—	247
		Ru-Ala–C_3N_4	Ru–N–C	—	EC	0.02	0.06–490	∼10.4 μA mM⁻¹	248
		FeN_5 SAC	Fe	∼1.57%	EC	0.000007	0.005–500	—	249
	ACh	Cu–N–C	Cu–N–C	5.1 wt%	CM	1.24	10–8000	—	219
	Adrenaline	Fe_1@CN20	Fe–N_4	2.9 wt%	CM	1.30	27.3–273.2	—	220
Antioxidants	AA	CNT/FeNC	Fe–N_x–C	0.2 at%	CM	0.03	0.1–10	—	229
		Fe–N–C SANs	Fe	1.13 wt%	CM	0.5	0.5–33	—	256
		Ni–N_4/C	Ni–N_4	0.35%	ECL	0.095	0.35–70	—	257
		Zn/Mo DSAC–SMA	Zn/Mo	Zn: 1.5 wt% Mo: 7.3 wt%	CM	0.76	0.1–5000	—	230
		SA–Pd/NPC	Pd	0.27 wt %	CM	1.24	10–8000	—	254
		SA–Pd/NC	Pd–N_4/C	0.20 wt%	CM	0.08	5–40	—	57
	Trolox	Fe–N–C SACs	Fe–N–C	1.3 wt%	ECL	0.8	0.8–1000	—	69
	Glutathione	Fe–NDs	Fe	—	CM	0.3	1–60	—	228
		SA–Pd/NPC	Pd	0.27 wt %	CM	3	10–100	—	254
		Co–N–C	Co	0.32%	CM	0.07	0.1–40	—	255
	Cysteine	Co–N–C	Co	0.32%	CM	0.06	0.1–20	—	255
Drugs and toxins	Oxytetracycline	SA–Pt/g-C_3N_4–K	Pt	3 wt%	CM	0.0224 (10.3 μg L⁻¹)	0.13–1.95 (60–900 μg L⁻¹)	—	217

Table 4 (continued)

Type of analytes	Analytes	Catalysts	Active sites	Active metal loading	Type of sensor	LOD^a (μM)	Linear range^a (μM)	Sensitivity (μA mM^{-1} cm^{-2})	Ref.
	4-Acetaminophen	FeSANs	Fe–N	0.028%	CM	3.23	30–400	—	259
	Levodopa	Co–SASC/GCE	Co	1.13 wt%	EC	0.033	0.1–200	—	261
		PtHPCN-222	Pt	0.24 at%	EC	0.003	0.1–1.0, 1–130	$\sim$848.3	262
	Fumonisin B1	Fe–N–C	Fe–N$_x$	4.86 wt%	CM	0.00002 (13.9 pg mL^{-1})	0.000028–0.21 (0.02–150 ng mL^{-1})	—	263
	Aflatoxin B1	Fe–N–C	Fe–N$_x$	4.86 wt%	CM	0.000009 (2.8 pg mL^{-1})	0.000016–0.64 (0.005–200 ng mL^{-1})	—	263
		Co SASCs	Co–O$_5$	2.08 wt%	ECL	0.0000014 (0.44 pg mL^{-1})	0.000032–3.02 (10–1000 pg mL^{-1})	—	264
Enzymes	α-Glucosidase	SA–Pt/CN	Pt	0.12 wt%	CM	3.8 U L^{-1}	10–8000 U L^{-1}	—	209
	BChE	Fe–N–C SAN	Fe–N–C	$\sim$1.85%	CM	0.054 U L^{-1}	2–40 U L^{-1}	—	266
	AChE	Fe–N–C	Fe	1.3 wt%	CM	0.0000323 (2.19 ng mL^{-1})	0.0001–0.0148 (8–1000 ng mL^{-1})	—	195
		Fe SA Cs	Fe	3%	EC	0.22 U L^{-1}	2–500 U L^{-1}	—	203
		Au–CDs	Au	—	CM	0.107 U L^{-1}	0.1–5 U L^{-1}	—	267
		Fe–N–C	Fe–N$_x$–C	0.2 at%	CM	0.014 U L^{-1}	0.1–25 U L^{-1}	—	268
		Fe–SAs/NC	Fe–N–C	—	FS	0.56 U L^{-1}	2–70 U L^{-1}	—	269
		Fe–N–C	Fe–N$_x$	0.96 at%	CM PT	1.9 U L^{-1} 2.2 U L^{-1}	3–40 U L^{-1} 3–40 U L^{-1}	—	218
	ACP	SA–Pd/NC	Pd–N$_4$/C	0.20 wt%	CM	0.0059 U L^{-1}	0.001–10.0 U L^{-1}	—	57
	ALP	Fe–N/C	Fe–N$_x$	2.06 wt%	CM	0.02 U L^{-1}	0.05–100 U L^{-1}	—	270
		Fe/NC–SAs	Fe–N–C	—	CM	0.05 U L^{-1}	0.1–1.5 U L^{-1}	—	271
	Tyrosinase	Cu,Gd@BHb^{FITC}	Cu/Gd	—	FS	FRET: 200 U L^{-1} IEF: 50 U L^{-1}	FRET: 1000–7800 U L^{-1} IEF: 400–1970 U L^{-1}	—	272
	Thrombin	TiMOF–Pt	Pt	—	EC	0.0000013	0.0000004–0.2	—	284
Cancer and tumour biomarkers	PSA	Fe$_{SA}$–Pt$_C$	Fe–N–C	Fe:1.2 wt%	CM	1.8 pg mL^{-1}	8–1000 pg mL^{-1}	—	273
		Co SAs/Co@C	Co	—	CL	20 pg mL^{-1}	0.05–10.00 ng mL^{-1}	—	275
	CEA	Fe–N–C SAC	Fe–N$_4$	5.0 wt%	CM	0.55 pg mL^{-1}	1–1000 pg mL^{-1}	—	274
		Fe–N–C SACs	Fe–N–C	—	ECL	1.1 pg mL^{-1}	5–80 000 pg mL^{-1}	—	276
	Exosomes	HCdS–Pt$_1$	Pt	1.76 wt%	PEC	157 particles μL^{-1}	500–50 000 particles μL^{-1} ^{b}	—	277
	HepG2 cells	Apt/Fe–N–C	Fe–N–C	0.80%	CM	—	100–200 000 cells	—	278
	miRNA-187	Au$_{SA}$/MXene	Au	—	ECL	0.0000000156	0.00000004–0.02	—	279
Others	H$_2$S	NiN$_4$–SACs	Ni–N$_4$	0.63 wt%	EC	$\sim$2	$\sim$2–198	—	28
	NO	Ni SACs/N–C	Ni–N–C	0.10%	EC	0.0018	—	430.6	37
		Ni–N$_2$O$_2$/AB	Ni–N$_2$O$_2$	9.2 wt%	EC	0.0018	0.01–6	0.072 μA nM^{-1}	282
	Haemoglobin	Fe–SAC	Fe–N$_x$	1.43 wt%	ECL	0.0000007	0.000001–0.01	—	65
	Cardiac troponin I	Co SACs	Co–O$_5$	0.2 wt%	CL	3.3 pg mL^{-1}	(0.01–50 ng mL^{-1})	—	265
	Cholesterol	Zn/Mo DSAC–SMA	Zn/Mo	Zn: 1.5 wt% Mo: 7.3 wt%	CM	0.76	0.1–5000	—	230
	Staphylococcus aureus (MRSA)	Ni@PEG	Ni	2.06 wt%	ECL	25 CFU mL^{-1}	73–7 300 000 CFU mL^{-1}	—	283

List of abbreviations. A–Co–NG: cobalt atoms anchored on an N-doped graphene matrix, Ala: alanine, Apt/Fe–N–C: aptamer modified Fe–N–C SACs, Au–CDs: Au-decorated N-rich carbon dots, CL: chemiluminescence, Co–SASC/GCE: Co SACs modified glassy carbon electrode, Fe–NDs: SA iron oxide-nanoparticle-modified nanodiamonds, Fe$_1$@CN20: iron single-atom anchored N-doped carbon material, NCA–Co: N-doped carbon aerogels embedded with Co single atoms, NCAG/Fe: N-doped carbon aerogels, Ni–N$_2$O$_2$/AB: Ni SA with N$_2$O$_2$ coordination anchored in porous acetylene black, Ni@PEG: PEGylated Ni SACs, PBS: phosphate-buffered saline, PGA-Fe/CS NPs: SA Fe-site-containing poly-γ-glutamic acid/chitosan hydrogel nanoparticles, PT: Photothermal, Pt$_1$/Ni$_6$Co$_1$LDHs/NG: Pt SAs anchored on Ni$_6$Co$_1$ layered double hydroxides/NG, Pt$_1$/Ni(OH)$_2$/NG: Pt SAs anchored on Ni(OH)$_2$ nanoplates/NG, PtHPCN-222: SA Pt anchored on a hollow-structured porphyrin zirconium-based MOF. SA–Pd/NPC: single-atomic palladium-loaded nitro-gen-doped porous carbon catalyst, sCo/NSG: single–Co atom dispersed NG, and Zn/Mo DSAC–SMA: Zn/Mo dual single-atom catalyst supported on the macroscope aerogel. ^{a} Note: The units and data in the reference are noted in brackets when there are unit conversions. ^{b} Detection range.

and therefore realize a higher peroxidase-mimicking activity (48.5 U mg^{-1}).[215] In the process of IIM, mesoporous silica as the imprinted substrate and [3-(2-aminoethylamino)propyl]tri-methoxysilane (A-Tri-EOS) were employed to provide abundant coordination sites for anchoring Fe SAs. Benefiting from its high activity and selectivity, Fe–SACs can be applied as a nanoprobe for the *in situ* detection of H$_2$O$_2$ generated from breast cancer cells.

The intentional modulation of the metal–support inter-action may also result in promising peroxidase-mimicking

activity. Zhu's group synthesized Fe–N–C SACs using $FeCl_2$, glucose, and dicyandiamide precursors. The SACs have good biocompatibility, realizing the *in situ* detection of H_2O_2 generated from the HeLa cells with a fine linear relationship between absorbance values of the TMB solution and H_2O_2 concentration in the range from 0.5 to 100 mM.[225] The Fe SAs can also be coupled with carbon-encapsulated Fe_3C nanocrystals (Fe_3C@C/Fe–N–C) by using $FeCl_3 \cdot 6H_2O$, $ZnCl_2$, glucosamine and melamine as precursors (Fig. 22a).[227] Compared with Fe–N–C SACs without carbon precursors, Fe_3C@C/Fe–N–C shows a higher sensitivity of 1225 $\mu A\ mM^{-1}\ cm^{-2}$ (Fe–N–C: 210.28 $\mu A\ mM^{-1}\ cm^{-2}$) and a lower LOD of 0.26 μM (Fe–N–C: 0.84 μM) (Fig. 22b). DFT calculations conclude that the electron transfer from the Fe_3C@C substrate to Fe SAs contributes the lower adsorption barrier and stronger adsorption of H_2O_2 molecules on Fe SAs (Fig. 22c).

Another cellular ROS, $O_2^{\bullet-}$, is the first radical formed by cells during the metabolic process and a precursor of other ROS, which is essential in various biological processes such as free radical inactivation, gene mutations and protein damage.[232] Detecting $O_2^{\bullet-}$ produced by cells is essential in diagnosing and treating various diseases, including cancers and cardiovascular diseases.[233,234] The adsorption mode plays a crucial role in sensing $O_2^{\bullet-}$. A Co SA dispersed NG (Fig. 22d) is applied for detecting $O_2^{\bullet-}$ released from prostate cancer cells.[231] With the addition of 4 nM $O_2^{\bullet-}$, the sensor reaches a 95% steady-state current within 1.2 s (Fig. 22e), and its LOD and sensitivity are approximately 1.5 nM and 710.03 $\mu A\ \mu M^{-1}\ cm^{-2}$, respectively. Theoretical calculation and experimental results indicate that Co SAs can vertically end-adsorb $O_2^{\bullet-}$, which produces a huge steric space for exposed Co to collect additional $O_2^{\bullet-}$, allowing fast and sensitive $O_2^{\bullet-}$ detection (Fig. 22f).

5.3.2 Metabolites.

Sweat, saliva and urine, as vital body fluids, contain a huge number of chemical compounds that indicate nutritional and metabolic states, which hold enormous promise for non-invasive and continuous monitoring of physiological indicators critical to human health. The disclosed SAC-based sensors primarily target a small number of analytes, such as electrolytes, glucose, and lactic acid.

Glucose is an essential ingredient for body metabolism. A glucose imbalance can lead to hypoglycemia, insulin shock, and diabetes. One of the most effective strategies to prevent and cure these disorders is accurately monitoring blood glucose concentrations. Electrochemical and fluorescence bioanalysis have the advantages of great sensitivity and rapid response time for glucose detection. N-doped carbon aerogels packed with Fe SAs (0.95 wt%) are proved to act as a peroxidase mimic for sensitive glucose detection by fluorescence spectroscopy as well as an excellent catalyst for the electrochemical oxidation of glucose.[235] The glucose concentration can be quantified within a wide linear range (electrochemical: 2–2000 μM, fluorometric: 20–1000 μM) and a low LOD (electrochemical: 0.5 μM, fluorometric: 3.1 μM). Similarly, N-doped carbon aerogels embedded in CoN_x sites (1.2 wt%) can also exhibit good performance (linear range of 0.5–6000 μM, and LOD of 0.1 μM) (Fig. 23a–c).[236] According to XANES, EXAFS and DFT simulations, the metal–N SAs (FeN_4, CoN_3 and CoN_4) at the edges of the aerogel nanopores exhibit optimal glucose adsorption energy, which contributes to the high sensitivity. The introduction of Co to $Ni(OH)_2$/NG can enhance the loading of Pt SAs from 0.36 wt% to 0.61%, increasing the sensitivity for glucose from 220.75 to 273.78 $\mu A\ mM^{-1}\ cm^{-2}$, and reducing the t_{res} from 4.6 to 1.8 s.[237,238]
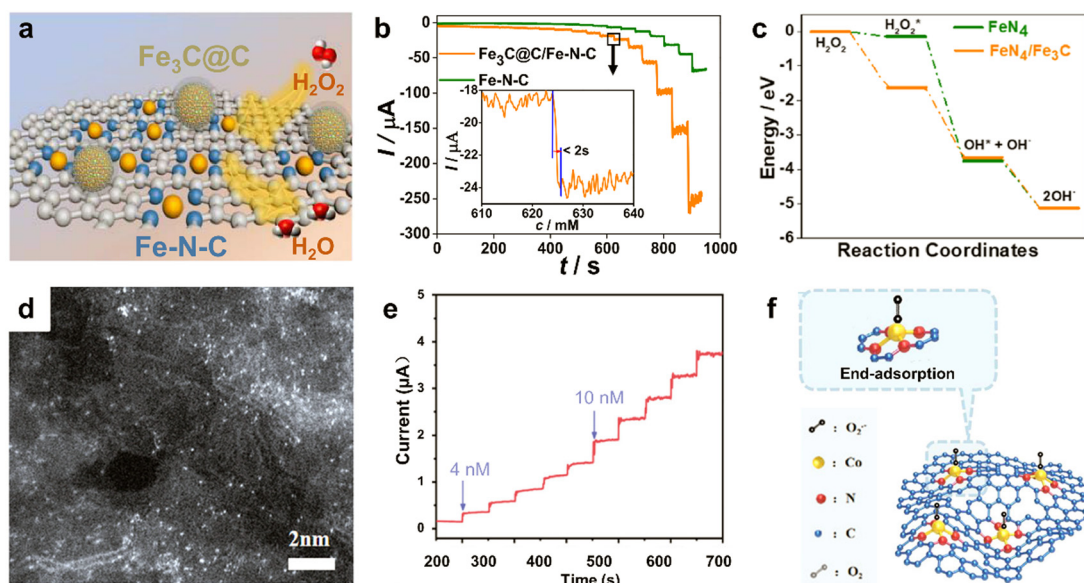

Fig. 22 (a) Schematic illustration of the Fe_3C@C/Fe–N–C catalyst for electrochemical H_2O_2 detection. (b) Chronoamperometric responses of Fe_3C@C/Fe–N–C and Fe–N–C to the H_2O_2 addition at 0 V. (c) Reaction energy of the H_2O_2 reduction on FeN_4 and FeN_4/Fe_3C coordination. Reproduced from ref. 227 with permission from American Chemical Society, copyright 2021. (d) HAADF-STEM image of Co SAs dispersed NG. (e) Chronoamperometric responses of Co SAs dispersed NG to the $O_2^{\bullet-}$ addition in PBS at 0.9 V vs Hg/Hg_2Cl_2. (f) The proposed end-adsorption mechanism for Co SAs in the $O_2^{\bullet-}$ oxidation. Reproduced from ref. 231 with permission from American Chemical Society, copyright 2021.
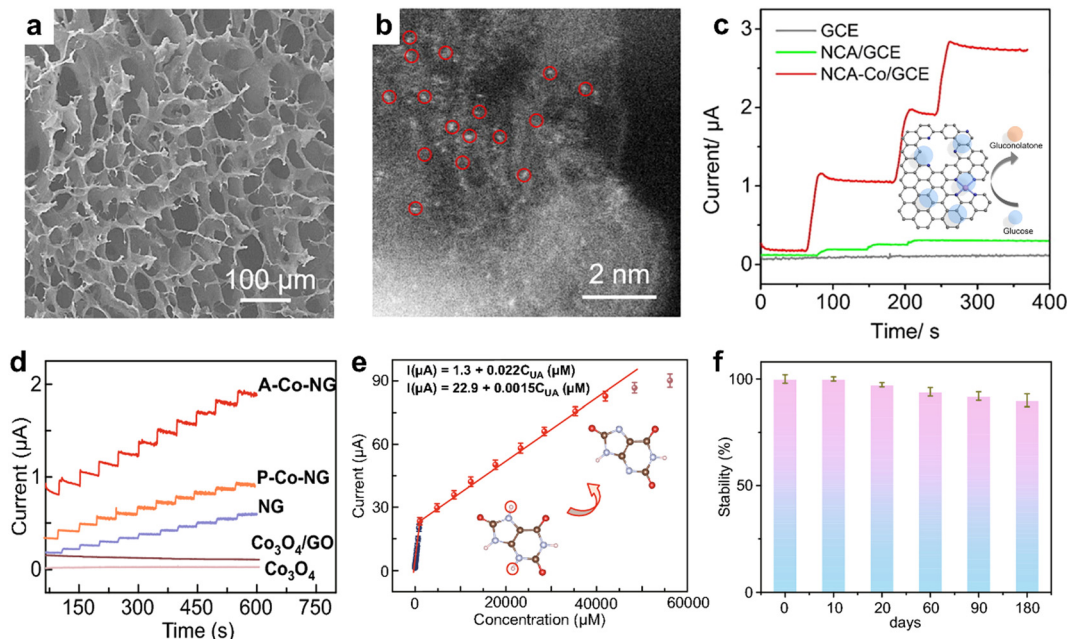
Fig. 23 (a) SEM image of the hydrogel precursor for the Co SA substrate. (b) STEM image of nitrogen-doped carbon aerogel anchored with Co SA sites. (c) Chronoamperometric patterns of GCE modified with/without Co SAs when 100 M glucose was added into 0.1 M NaOH at +0.3 V. Reproduced from ref. 236 with permission from Elsevier B.V., copyright 2022. (d) Chronoamperometric patterns of Co SACs and reference samples when adding 5 μM UA in 0.1 M NaOH at 0.3 V. (e) Correlation between current values and UA concentrations with linear correction. (f) Stability of the Co SACs for UA sensing within 180 days. Reproduced from ref. 243 with permission from Springer Nature, copyright 2020.

Traditionally, glucose oxidase (GOx) can decompose glucose in the presence of oxygen and water to produce H_2O_2. Consequently, the concentration of glucose can be indirectly detected from the concentration of generated H_2O_2 utilizing a SACs' fluorometric[235] or colourimetric[239,240] sensing technique. Enlightened by this, a cascade sensing proposal is to use Ir SA embedded nitrogen-doped carbon (SA–Ir/NC) as the cathode of liquid zinc–air batteries to detect glucose with a low LOD of 67.3 nM.[241] During the reaction of batteries, the Zn foil transfers electrons to the cathode, while the SA–Ir/NC reduces O_2 to produce H_2O. Simultaneously, GOx would consume O_2 while transferring glucose to produce gluconate and H_2O_2. Since the catalytic process of SA–Ir/NC occurs through a direct $4e^-$ pathway rather than a $2e^-$ pathway to H_2O_2, there is only a considerable drop in current responsiveness to saturated O_2 (weak response to H_2O_2). In this way, variations in glucose concentration would result in changes in oxygen concentration, which could be reflected by the open-circuit voltage signal and enable self-powered sensing.

Galactose is yielded from the hydrolysis of lactose. High galactose levels may lead to severe galactosemia, which can induce liver failure, mental retardation, cataract and a variety of other complications. Su's group developed a cascade colourimetric sensor based on galactose oxidase and Fe–N–C SACs.[242] The principle is that galactose oxidase can precisely decompose galactose and generate H_2O_2, which is then selectively catalyzed by peroxidase-like Fe–N–C SACs to form •OH and oxidize TMB to turn blue. The two cascaded selective catalytic processes ensure the highly selective detection of galactose. The linear relationship between galactose concentration and TMB solution absorbance in the range of 50–500 M can be used to quantify galactose concentration.

Uric acid (UA) is a significant metabolite in normal human urine. The normal UA concentration in human blood is 15 to 80 mg L^{-1}, but an abnormal UA concentration can be associated with disorders including hyperuricemia, cardiovascular and genetic diseases.[244] Recent studies have focused on SACs as a replacement for the enzyme in the electrochemical detection of UA with a broad detection range and low detection limit. Co SACs consisting of Co–$N_{3.4}$ SAs on an N-doped graphene matrix preferentially catalyzes the oxidation of UA, resulting in a broad electrochemical detection range (0.4–41 950 μM) and a low LOD (33.3 nM, Fig. 23e).[243] The sensitivity of Co SACs (301.6 μA mM^{-1} cm^{-2}) is nearly quadrupled compared to Co particle-modified N-doped graphene at 5 μM UA (Fig. 23d). The Co SACs also exhibit strong stability by retaining more than 90.5% activity after 180 days of storage (Fig. 23f). DFT calculation reveals that the formation of Co^{3+}–OH is the probable limiting step for the oxidation of UA.

5.3.3 Neurotransmitters. Neurotransmitters are chemicals that communicate between neurons or between neurons and effector cells, such as glandular and muscle cells. They play a significant part in various physiological and pathological aspects, as well as conveying stimulating information to the kidney, cardiovascular system, and central nervous system. Therefore, precise and quantitative detection of neurotransmitters is crucial for biological research and medical diagnosis. Despite the fact that techniques

such as liquid chromatography-mass spectrometry, enzyme-linked immunosorbent assay, and northern blot have advantages such as high sensitivity and accuracy, drawbacks such as being expensive, complicated, and time-consuming limit their applications, making SACs-based electrochemical biosensors more suitable for point-of-care evaluation.

Dopamine (DA) is an essential endogenous nitrogenous chemical molecule in the human body. Abnormal dopamine release is linked to neurological conditions and depression. To fully comprehend the physiological significance of DA, it is vital to track its levels *in vivo* and in real-time.[245] A Co–N–C structure synthesized from ZIF-8 and ZIF-67 precursors with 0.25% Co–N_x provides a high sensitivity (979.6 µA mM^{-1} cm^{-2}) and a low LOD (0.04 µM) for the electrochemical detection of DA produced by live PC12 cells.[170] Meanwhile, the carbonaceous substrate brings robust stability of Co–N_x SAs under H_2O_2 conditions.

To further improve the sensitivity of the SAC-based DA sensor, 2D MoS_2 with a high surface-to-volume ratio was used as a substrate for loading Mn SAs. Ebrahimi's group synthesized an Mn-doped MoS_2 sensor by electrodeposition and solid vapour deposition to reach a high Mn atom ratio of ∼2.15 at% (Fig. 24a).[246] The LODs of the Mn-MoS_2-based sensor to DA were 50 pM, 5 nM, and 50 nM in phosphate-buffered saline, 10% serum, and artificial sweat, respectively. Two different defect configurations were observed in Mn-doped MoS_2: Mn on top of a Mo atom (Mn_{topMo}) and Mn substituting a Mo atom (Mn_{Mo}) (Fig. 24c). According to the DFT calculations, the defect formation energy of Mn_{Mo} is significantly lower than that of other defect configurations, making the Mn_{Mo} sites twice as abundant as Mn_{topMo} sites. The Mn_{Mo} can physically adsorb DA even at a low concentration (50 pM) (Fig. 24b), allowing for a higher probability of hole transfer to DA. Considering that Ni has a stronger electronegativity and redox pair Ni(ɪɪ)/Ni(ɪɪɪ) to adsorb and oxidize DA more easily, Wu's group doped Ni SAs
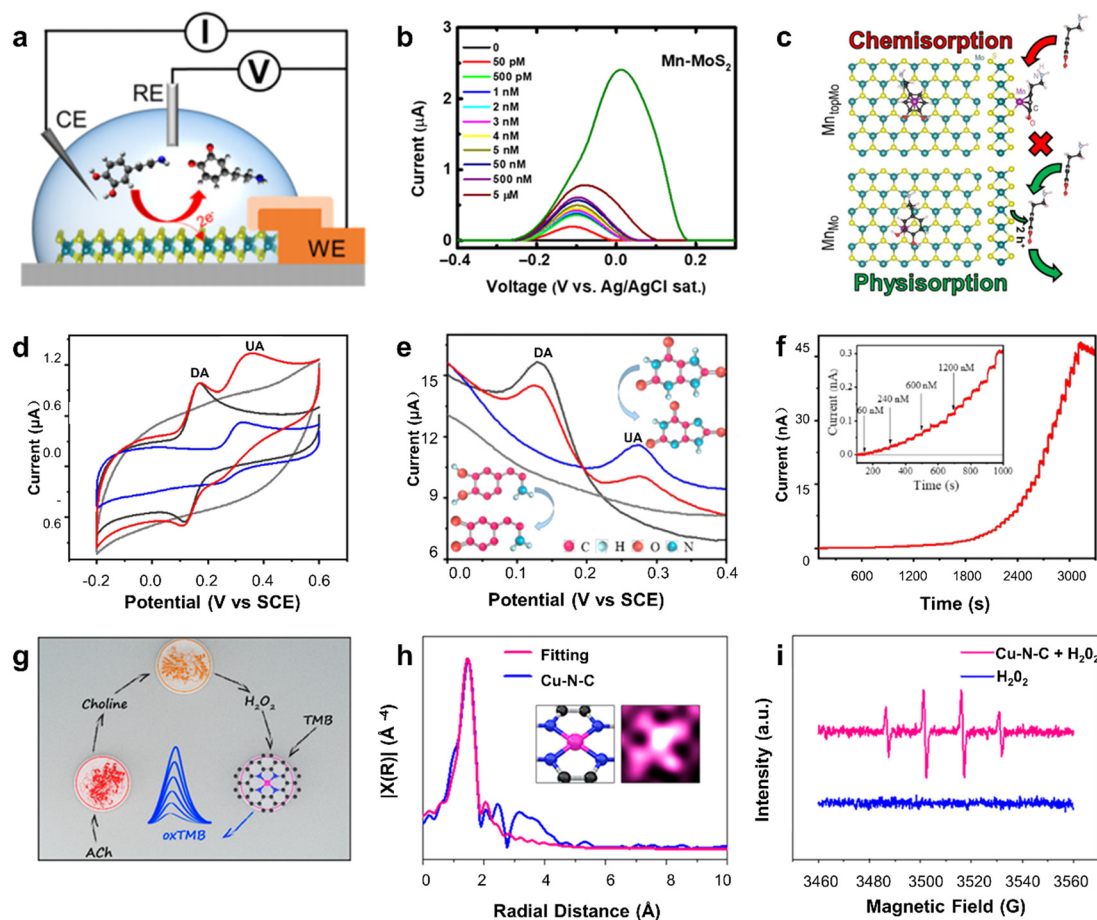

Fig. 24 (a) Schematic illustration of the electrochemical DA detection with an all-integrated sensor. (b) DPV of Mn-MoS_2 SACs in PBS with DA of different concentrations. (c) The schematic illustration of DA interacting with Mn_{topMo} (neutral defect) and creating a chemical bond, as well as DA physically adsorbed on $Mn_{Mo}{}^{+1}$. Reproduced from ref. 246 with permission from American Association for the Advancement of Science, copyright 2020. (d) CVs and (e) DPVs of the Ru SACs upon addition of 100 µM DA (black) and 200 µM UA (blue) in the presence (red) and absence (grey) of 100 µM DA and 200 µM UA mixture in 0.1 M PBS. (f) Chronoamperometric patterns of Ru SACs when adding DA in 0.1 M PBS at 0.2 V *versus* SCE. Reproduced from ref. 248 with permission from American Chemical Society, copyright 2021. (g) Schematic of the three-enzyme system (red circle: AChE, orange circle: ChOx, purple circle: Cu–N–C SACs) for ACh detection. (h) FT-EXAFS spectra and the fitting curve of Cu–N–C. Inset: Local Cu–N_4 structure. (i) EPR spectra for the ·OH detection in H_2O_2 with and without Cu–N–C. Reproduced from ref. 219 with permission from American Chemical Society, copyright 2020.

on flower-like MoS_2, enabling a lower LOD of 1 pM for DA detection.[247]

As DA and UA with similar structures are meaningful electrochemically active molecules that coexist in the human body, selectively sensing them is noteworthy but challenging due to adjacent redox potentials. SACs *via* Ru SAs dispersed on a C_3N_4 substrate were designed to detect them simultaneously by CV and DPV measurements.[248] The Ru SAC-based sensor shows a large separation of peak potentials (180 mV) for the electro-oxidation of DA and UA, indicating the feasible distinction between them (Fig. 24d–e). Furthermore, due to the good conductivity of Ru atoms and the increasing sp^2 C after doping, electron transfer is significantly facilitated, enabling simultaneous electrochemical determination of DA and UA over a wide linear concentration range (DA: 0.06–490 μM, Fig. 24f, UA: 0.5–2135 μM) and low LODs (DA: 20 nM, UA: 170 nM). Another enzyme-like Fe–N₅ SAC obtained by the sol-freeze dry-pyrolysis method exhibits a lower LOD (0.007 nM DA and 0.027 nM UA).[249] This can be attributed to both the effective incorporation of Fe SAs (1.57%) to enhance electrochemical reaction and the strong contact of DA/UA with the graphene substrate to enable fast electron transfer from Fe–N₅ SACs to DA/UA.

Combining electrochemical and luminescence phenomena, luminol-assisted ECL has been applied for DA sensing due to its benefits of simplicity and expeditiousness.[65] In the luminol-assisted ECL systems, Fe SACs (1.43 wt% Fe) and dissolved oxygen rather than H_2O_2 act as co-reactants in the generation of ROS, which avoid the application of unstable H_2O_2. Due to the competition between the ROS oxidation process of luminol (which would enhance the ECL light signals) and DA molecules, the DA concentration can be determined from the light signal weakening. The developed Fe SAC–luminol-dissolved O_2-ECL system can detect DA, hemin, and Hg^{2+} with low LODs of 0.1 pM, 0.7 pM, and 0.13 nM, respectively. In the system, an $Au@SiO_2$ nanomembrane was also used to excite 2D plasmons and link with the ECL system to improve ECL performance, which can be increased by Fe SACs.

ACh is an important neurotransmitter in the nervous system. A disordered amount of ACh is highly associated with Alzheimer's and Parkinson's diseases.[250] Zhu's group constructed a three-enzyme-based cascade catalysis for colourimetric detection of ACh by using acetylcholinesterase AChE, choline oxidase (ChO_x) and peroxidase (such as SACs), where ACh is catalyzed by AChE and ChO_x to generate H_2O_2 (Fig. 24g).[219] The produced H_2O_2 would be catalysed to ROS with the help of peroxidase, changing the colour of TMB solutions. To precisely detect this H_2O_2 with a concentration much lower than that of ACh, Cu–N–C SACs with peroxidase-like activity were synthesized *via* a KCl-template strategy. Benefiting from the abundant Cu sites (~5.1 wt%, Fig. 24h), the SACs are able to trace 10–8000 μM ACh linearly and realize a low LOD of 1.24 μM. The active sites of Cu SAs can also be demonstrated by the presence of the ·OH active intermediate during the catalytic processes from EPR spectra (Fig. 24i).

Adrenaline is a phenolic molecule that functions as a neurotransmitter and hormone. Adrenaline can cause a person to breathe faster, increase his pulse rate and blood flow, and speed up his body's energy production when exposed to stimuli. Laccase is regarded as a green catalyst in the detection and degradation of phenolic substrates because it can oxidize a number of phenols through the process of four-electron reduction of O_2 to water. However, due to its sensitive nature, low denaturation stability, and expensive purifying method, its applications are limited. Fe SA anchored on N-doped carbon can act as a laccase-like nanozyme, catalyzing the oxidation of phenolic compounds such as adrenaline.[220] Compared with laccase (LOD of 3.9 μM), the Fe SACs show a lower LOD (1.3 μM) and higher stability for adrenaline, which have similar kinetic constants to those of laccase. This can be attributed to the homogeneous and well-defined Fe SAs (2.9 wt%) supported by the carbon substrate with a large specific surface area (681 m² g⁻¹).

5.3.4 Antioxidants. Antioxidants serve as free radical scavengers and are crucial for redox homeostasis in the body.[251–253] Glutathione, cysteine, and AA are representative antioxidants in the body. Although it is possible to use colourimetric sensing with H_2O_2 as an oxidant to produce TMB-H_2O_2 colourimetric reactions,[254] stable SACs with high oxidase-like catalytic activity are required for use as a substitute in antioxidant sensors because no destructive and unstable H_2O_2 is involved (Fig. 25a).

Glutathione and cysteine are biothiols and are associated with a variety of clinical diseases, such as cancerous tumours, Parkinson's disease and Alzheimer's disease. Homogeneous Co–N–C SAs on nitrogen-doped porous carbon synthesized by a sacrificed ZIF-template method was reported to have high sensitivity and low LODs of 70 nM and 60 nM for glutathione and cysteine, respectively.[255] The Co SACs show 11-fold higher oxidase-like activity than that of Co NPs. In addition, the SACs also exhibit good selectivity among 12 kinds of other amino acids with 10 times higher concentrations.

AA, also known as vitamin C, is a reducing agent (electron donor) in the human body, which can be oxidized by ROS and lose two electrons from the double bond between its second and third carbon to have numerous therapeutic properties, such as bone formation, prevention of blood clotting and synthesis of collagen. Although some nanozymes such as iron oxide (Fe_3O_4) process intrinsic peroxidase-like activity, their catalytic activities are still much inferior to those of natural peroxidases like horseradish peroxidase (HRP). The Fe SACs prepared by ionic salt-assisted synthesis methods were found with better oxidase-like activities compared to those without the salt template. Fe SACs were synthesized by anchoring Fe SAs on N-doped carbons supported on CNT (CNT/FeNC).[229] During the synthesis, NaCl plays an important role in making nanopores and improving the SSA to anchor more Fe–N_x–C moieties, resulting in 100% Fe–N_x–C moieties in the final CNT/FeNC. Due to the large surface area (1140 m² g⁻¹) of the site-holding substrate (CNT) and the 100% SA dispersed active sites, CNT/FeNC realized the lowest LOD of 30 nM to AA. As potassium shows much easier intercalation than sodium in the activation process of materials, KCl-treated Fe SACs showed a
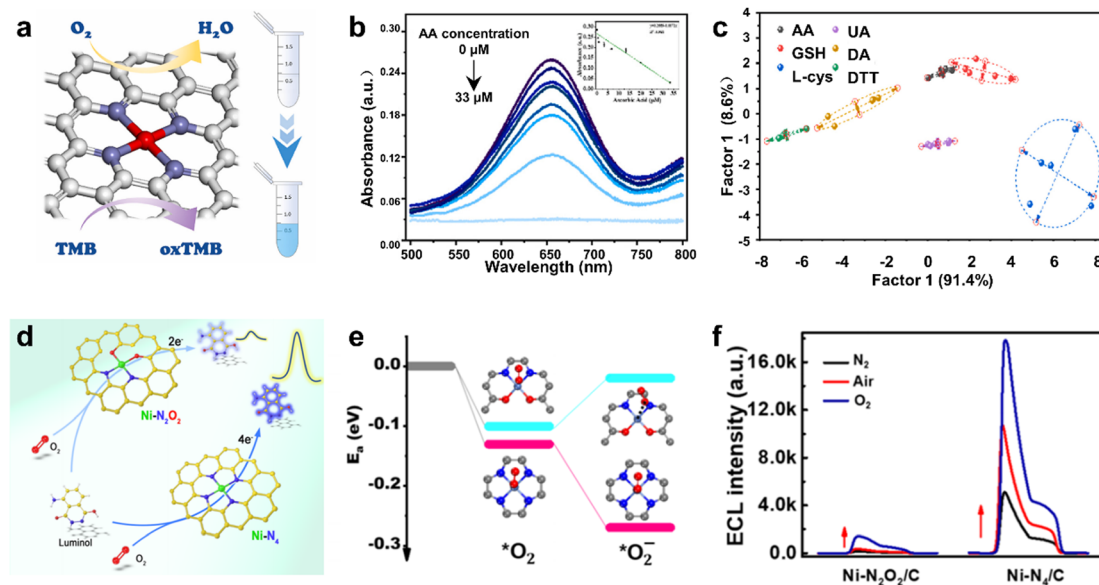
Fig. 25 (a) Schematic illustration of the oxidase-like activity of SACs. (b) UV-vis absorption spectra of TMB solutions containing KCl-treated Fe–N–C SACs and 0–33 μM AA. Inset: linear correlation between AA concentration and absorbance signals at 652 nm. (c) 2D canonical score-plot of linear discriminate analysis for six antioxidants at 10 μM. Reproduced from ref. 256 with permission from Elsevier B. V., copyright 2022. (d) Schematic illustration of SACs with Ni–N₄ sites in the luminol-dissolved O₂-ECL system for DA detection. (e) Adsorption energies (E_a) of the adsorbed $*O_2$ to $*O_2^-$ on Ni–N₂O₂ and Ni–N₄ sites. (f) ECL intensities of Ni–N₂O₂/C- and Ni–N₄/C-modified electrodes in a saturated solution of N_2, air, and O_2. Reproduced from ref. 257 with permission from American Chemical Society, copyright 2021.

higher defect rate than NaCl-treated Fe SACs in anchoring Fe SAs, resulting in more active oxidase-like properties (0–33 μM, Fig. 25b).[256] More importantly, KCl-treated Fe SACs exhibit oxidase-like activity retention of 76%, 79% and 88% after undergoing 12 h of strong acid and alkali treatment and 6 months, respectively.

A similar method to that used to detect luminol-dissolved O_2-ECL DA can also detect AA *via* SACs. Zhu's and Hu's group synthesized carbon-supported nickel with Ni–N₄ and Ni–N₂O₂ as coordination environments to amplify the luminol ECL emission (Fig. 25d).[257] The Ni–N₄ SAC-luminol-dissolved O_2-ECL system can detect AA in the linear range of 0.35–70 μM with a low LOD of 95 nM. The polarization curve and DFT calculation results reveal that SACs with Ni–N₄ sites show a lower $O_2^{\bullet-}$ adsorption energy (−0.27 eV) than that of Ni–N₂O₂ sites (−0.02 eV). The preference for Ni–N₄ can be attributed to its propensity toward the four-electron pathway to reduce O_2 into H_2O, thereby boosting the ROS emission and ECL performance (Fig. 25e and f). The luminol-dissolved O_2-ECL system with Fe–N–C SACs is also suitable for Trolox sensing, which can realize a linear detection range of 0.8–1000 μM.[69]

Antioxidants and free radical scavengers such as AA, GSH, L-cys, DTT, UA, and DA often exist in the same drug, which propose challenges for their selective sensing. The combination of machine learning and Fe–N–C SAC-based sensor arrays can achieve accurate identification.[256] The original data sets are achieved from absorbance records of "3 SACs as sensing elements × 6 antioxidants as analysts × 5 replicates". Then the data are gathered as groups by linear discrimination analysis and hierarchal cluster analysis methods. The sensor

array can discriminate six kinds of antioxidants at 0.5, 6.67, 10 and 33 μM (Fig. 25c).

5.3.5 Drugs and toxins. Drugs such as 4-acetamidophenol (AMP), oxytetracycline and levodopa have unique effects in the treatment of certain disorders. However, excessive use can have detrimental repercussions on the human body, including organ damage, movement abnormalities, and other problems. As a result, drug sensing is beneficial in correctly controlling its dosage.

AMP is applied as an analgesic and antipyretic drug, but its overuse may result in severe liver and brain damage.[258] The usual chromatography and high-performance liquid chromatography require complex processes and expensive equipment. Dong's group proposed a colourimetric method for convenient AMP detection based on the inhibitory effects of AMP on Fe SACs synthesized by salt-templated and pyrolytic strategies.[259] AMP reacts with Fe SACs to prevent TMB oxidation, resulting in blue-colour fading (absorbance at 652 nm decreasing). The colourimetric sensing method demonstrated a linear detection range of 0.03–0.4 mM and a LOD of 3.23 μM at a signal-to-noise ratio of 3. When being applied to the AMP measurement in commercial paracetamol tablets, the Fe SAC-based sensor showed 92.0%–110.3% recovery with <5.7% relative standard deviation, indicating its applicability. Based on the similar inhibitory effect of analytes on SACs, Pt SACs with Pt–N–C coordination environments realized a linear detection range of 60–900 μg L⁻¹ and a LOD of 10.3 μg L⁻¹ for colourimetric detection of oxytetracycline (a rapid bacteriostatic agent).[217]

Levodopa is a precursor for dopamine synthesis and is used in the clinical treatment of Parkinson's disease.[260] A series of

analytical techniques have been developed to detect levodopa, such as capillary electrophoresis, chemiluminescence, spectroscopy, high-performance liquid chromatography and electrochemistry. However, it is still a challenge to detect levodopa in real and complex biological samples. An electrochemical sensor based on Co SACs synthesized from pyrolyzed ZIF-8@ZIF-67 (Fig. 26a and b) showed a linear detection range of 0.1–200 μM and a LOD of 0.033 μM to levodopa (Fig. 26c).[261] Levodopa's current signal is altered by 3.9% when the main interferents in human serum (K^+, Na^+, Cl, Fe^{3+}, nitrate, glucose, AA, lactic acid, urea, and L-cysteine) are added at 10 times higher concentrations than that of levodopa (50 μM) (Fig. 26d). This improves the potential of Co SAC-based sensors in a complex biological matrix. In addition, considering that the hollow structure can enhance the porosity to improve the diffusion rate of the target analytes, and increase the SSA to expose more SA sites, a naturally hollow-structured MOF (HPCN-222) was proposed to be doped with Pt SAs.[262] This design enabled the stable dispersion of Pt SAs, realizing a lower LOD of 3 nM and a good stability for 150 days (stored at 4 $^\circ$C).

Apart from pharmaceuticals, mycotoxins also require sensors for quick detection. For instance, aflatoxin B1, a mycotoxin existed in many foods, has strong thermal stability (decomposition temperature > 280 $^\circ$C) and ranks first in terms of carcinogenicity among known chemical substances. As the SACs can catalyze the generation of massive superoxide radical anions from H_2O_2, they can be integrated with existing techniques to magnify the sensing signals. Yu's group synthesized ZIF-8-derived Fe SACs, which magnifies the colourimetric signal in LFIA for mycotoxin detection.[263] With the introduction of

TMB solution, the sensitivity further increases by 16 and 11 times for aflatoxin B1 and fumonisin B1, achieving low LODs of 2.8 and 13.9 pg mL^{-1}, respectively. Ouyang et al. proposed a ZIF-8-derived yolk–shell Co SAC, enhancing luminol–H_2O_2 ECL signal by ~ 3133.7 times to realize a low LOD of 0.44 pg mL^{-1} for aflatoxin B1.[264] EXAFS fitting confirmed the coordination number of Co being 5.31 ± 0.46, contributing to the atomic dispersion of Co–O(N)$_5$ moieties. They also applied Co/Fe SACs, synthesized by the same approach as a chemiluminescent immunoassay sensor, to detect cardiac troponin I (a protein) and achieve a linear range of 0.01–50 ng mL^{-1} and a LOD of 3.3 ng mL^{-1}.[265]

5.3.6 Enzymes. Enzymes such as butyrylcholinesterase (BChE), acetylcholinesterase (AChE), phosphatase, tyrosinase and thrombin are necessary proteins that accelerate chemical processes in the body such as digestion and liver function. The concentration of enzymes in the blood can help in the diagnosis of injuries and disorders. The enzyme concentrations are measured from their catalytic activity (units, U) as enzyme molecules are difficult to decompose. U represents the quantity of enzyme required to catalyze the transformation of 1 mol of substrate per minute under defined pH and temperature conditions.[221]

The first application of SACs to detect enzymes was reported in 2019 by Lin and Du's group.[266] A Fe–N–C SAC with peroxidase-mimetic activity was proposed for BChE sensing. The Fe–N$_x$ active sites are anchored by the porous carbon, which catalyses H_2O_2 and promotes the colouring reaction rate of the TMB–H_2O_2 solution. When BChE is highly active, the thiocholine (TCh) produced by the hydrolysis of substrate S-butyrylthiocholine iodide will block the Fe–N$_x$ coordination environments and inhibit the colouration of TMB-H_2O_2. As a result, the specific activity of Fe–N–C SACs (57.76 U mg^{-1}) is almost comparable to that of natural horseradish peroxidase (297 U mg^{-1}). As a proof-of-concept application, a paper bioassay integrated with a smartphone was manufactured by taking the G/(R + G + B) ratio as a factor, which resulted in a linear detection range of 2 to 40 U L^{-1} and a LOD of 1.7 U L^{-1}.

TCh is the hydrolysis product of acetylthiocholine in the presence of AChE; thus it can also be detected via Fe–N–C SACs in the H_2O_2-existing chromogenic reaction system.[267–269] This is because TCh can bind with Fe–N–C SACs and inhibit their peroxidase-like activity, which is responsible for oxidizing TMB and OPD to produce colourimetric and fluorescent signals. Based on this mechanism, the lowest LOD for AChE activity was 0.014 U L^{-1} with a linear range of 0.1–25 U L^{-1}.[268] Besides, as oxTMB also exhibits photothermal capacity when exposed to an 808 nm laser, the activity of AChE can be determined from the temperature signal using a near-infrared imaging camera within a minute.[218] However, the Fe–N–C SACs are still limited by their biocatalytic activity and selectivity. A boron-doped Fe–N–C SAC with FeN$_4$–2B coordination environments can detect AChE in the range of 0.8–100 mU (Fig. 27a).[195] The B doping increases the coordination number, oxidation valence and distance between Fe–N, which leads a ~ 4-fold increase in specific activity (Fig. 27b) and sufficient specificity in the
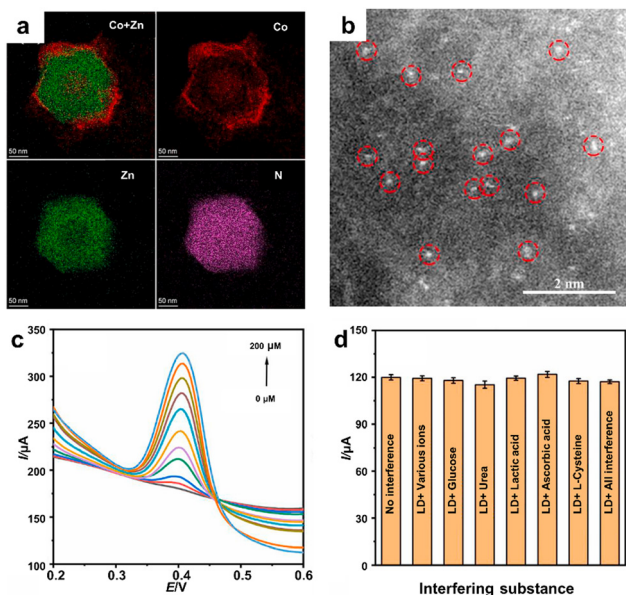

Fig. 26 (a) EDS mapping and (b) HAADF-STEM image of the Co–SAC. (c) DPVs of the Co SAC-based sensor when adding different concentrations of levodopa in 0.1 M PB. (d) Sensing current signals of the Co SAC-based sensor to levodopa with different interfering substances. Reproduced from ref. 261 with permission from Elsevier B. V., copyright 2020.
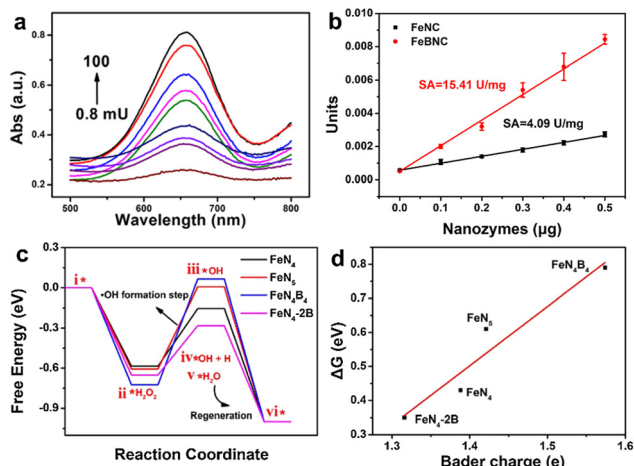
Fig. 27 (a) UV-vis spectra in the FeBNC SACs/H_2O_2/TMB system when adding 0.8–100 mU AChE. (b) The specific activities of FeBNC and FeNC SACs (U mg^{-1}). (c) Free energies of FeN_4, FeN_5, FeN_4B_4, and FeN_4-2B in the H_2O_2 reduction process with an acidic environment. (d) Linear correlation between the charges of Fe atoms on various coordination and the energy barriers of ·OH production. Reproduced from ref. 195 with permission from Elsevier Ltd, copyright 2020.

presence of some possible interferences. DFT calculation demonstrates that heteroatoms such as B atoms with smaller electronegativity (2.04, where N is 3.04 and C is 2.55) are able to regulate the electronic structures of centre Fe atoms in Fe–N–C SACs, thereby decreasing the energy barriers of active intermediates (·OH) (Fig. 27c and d).

Phosphatase, which includes acid phosphatase (ACP) and alkaline phosphatase (ALP), is a natural enzyme found in many organisms that catalyzes the hydrolysis of phosphate groups in various biological substrates such as protein, nucleic acid, and alkaloid. Furthermore, phosphatase is a biochemical indicator found in serum that can be used to diagnose disease. Abnormal phosphatase activity is linked to liver disease, bone disease, endocrine disease, and diabetes. AA is the hydrolysis product of ascorbic acid 2-phosphate in the existence of ACP or ALP, and can also inhibit the oxidation of TMB. Therefore, ACP and ALP can be detected based on Fe–N–C SACs *via* similar colourimetric sensing.[57,270,271] The lowest LOD of ACP and ALP detected by SACs was 0.0059 and 0.02 U L^{-1}, with a linear range of 0.001–10.0 and 0.1–1.5 U L^{-1}, respectively.[57,270]

Tyrosinase is a binuclear copper oxidase that can be oxidized and polymerized to produce melanin. It is regarded as an essential biomarker, but its selectivity for detection is still a challenge. Based on the fluorescence method, Cu SAs anchored on bovine haemoglobin (BHb)-template gadolinium nanoparticles (Cu,Gd@BHb NPs) were applied for tyrosinase detection.[272] These Cu,Gd@BHb NPs have the advantages of Cu^{2+}, Gd^{3+}, and BHb, where Cu^{2+} and BHb are used to enhance the peroxidase catalytic activity, while Gd^{3+} is utilized to induce abundant oxygen vacancy defects and load additional oxygen molecules onto NPs. Two fluorescence sensing strategies were developed: Strategy I detected tyrosinase with a LOD of 0.20 U mL^{-1} *via* fluorescence resonance energy transfer (FRET)

between the fluorescein isothiocyanate (FITC) and generated polydopamine dots. Strategy II was based on the elimination of the inner-filter effect (IEF) between FITC, phenol, and 4-aminoantipyrine, realizing a LOD of 0.05 U mL^{-1}. These two strategies exhibited high selectivity to tyrosinase among the other 18 enzymes and proteins. In addition, paper microchips were fabricated based on strategy II for detecting tyrosinase based on RGB values using a smartphone. It identified tyrosinase in serum samples with a linear range of 0.40–1.97 U mL^{-1} and a LOD of 0.12 ± 0.11 U mL^{-1}.

5.3.7 Cancer and tumour biomarkers. Biomarkers play important roles in cancer and tumour detection, early diagnosis, monitoring, and therapy. There are many kinds of cancer and tumour biomarkers, including nucleic acid, protein, enzyme, *etc.* The enzyme-linked immunosorbent assay was a well-established method for detecting these biomarkers by effectively amplifying signals and enhancing sensitivity. Based on the enzyme cascade reaction, Zhu's group developed a series of colourimetric,[273,274] chemiluminescence,[275] and electrochemiluminescence[276] sensors to detect prostate-specific antigen (PSA) and carcinoembryonic antigen (CEA), two internationally acknowledged biomarkers for the clinical monitoring of prostatic and broad-spectrum cancer, respectively. They combined GOx with Fe SA confined platinum clusters (Fe_{SA}–Pt_C SACs) to amplify the cascade sensing signals, which can detect PSA with a LOD of 1.8 pg mL^{-1} (Fig. 28a and b).[273] Compared to single Fe_{SA} SACs (19.3 U mg^{-1}) and Pt_C Fe_{SA}–Pt_C SACs (12.4 U mg^{-1}), Fe_{SA}–Pt_C SACs have superior activity (87.7 U mg^{-1}). The principle of this cascade signal amplification can be deduced as follows: PSA is bound with monoclonal antibodies and recognized by labelling monoclonal antibodies (ZIF-8@GOx). When glucose is added, GOx catalyzes the glucose and produces H_2O_2, which then
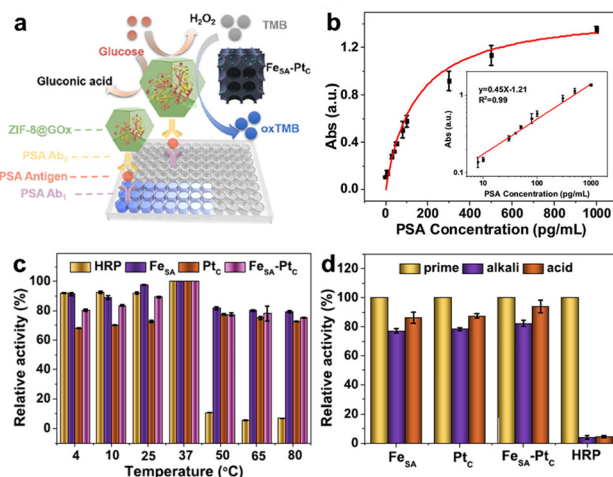

Fig. 28 (a) Schematic illustration of the cascade sensing PSA by FeSA–Pt_C-ZIF-8/GOx enzyme-linked immunosorbent assay. (b) The relationship between absorbance signals of Fe_{SA}–Pt_C SACs and the PSA concentration. Inset: linear correlation. Influence of (c) temperature and (d) acidic and alkaline environments on the POD-like activity of the SACs and HRP. Reproduced from ref. 273 with permission from American Chemical Society, copyright 2021.

oxidizes TMB in the presence of FeSA–PtC SACs and changes the colour of the solution. Compared to HRP, the FeSA–PtC SACs exhibit higher tolerance to increasing temperature and strongly acidic and alkaline environments, which can be applied for diagnosing prostate cancer in clinical practice (Fig. 28c and d). Following a similar sensing strategy, a tetracoordinate G-heme SACs with active sites of Fe–N realized CEA sensing with a LOD of 0.55 pg mL^{-1}.[274]

In order to further improve the sensitivity of SACs to biomarkers, a strategy is to adjust the substrate structure of SACs. The hollow structure can effectively separate catalytic sites, improve mass transfer, speed up reaction rate and improve catalyst selectivity. For instance, hollow Pt SACs (HCdS–Pt$_1$) were fabricated by anchoring Pt SAs on the surface of hollow cadmium sulfide via a SiO$_2$-template strategy.[277] The spectroscopic and photoelectrochemical tests revealed that HCdS–Pt$_1$ has superior photoactivity compared to HCdS and HCdS–PtNPs. A photoelectrochemical cascade sensing platform was created by cascading HCdS–Pt$_1$ with high-biorecognition DNA flowers enclosed by HRP and GOx to count exosomes (biomarkers to identify early-stage tumours) with a LOD of 157 particles μL^{-1}.

To identify and detect cancer cells more efficiently, another strategy is to enhance the dispersion of SACs in aqueous solutions and recognition ability. Feng's group engineered single-stranded DNA onto Fe–N–C SACs to enhance their aqueous dispersion and recognition ability.[278] As Fe–N–C SACs were synthesized by high-temperature pyrolysis of Fe-doped ZIF-8, they are hydrophobic and can be bound to DNA bases containing hydrophobic rings. Such binding is more stable than the π–π stacking and hydrogen bonding between the DNA bases and the GO carbon skeletons, allowing for easier adsorption of adenine and thymine with basic groups. A cancer cell (HepG2) colourimetric biosensor was then developed based on the principle that Fe–N–C SACs recognized cancer cells and catalyzed the oxidation of TMB to develop a colour change in the presence of H$_2$O$_2$. The sensor showed good selectivity for HepG2 and a wide linear detection range of 100–200 000 cells. Following a similar performance-improving strategy, Su's group designed a SA Au-doped MXene sensor to detect miRNA-187 in triple-negative breast cancer tumour tissues via ECL signals.[279] The difference is that the hydroxyl radicals produced from H$_2$O$_2$ on SACs enhance the ECL rather than colourimetric signals. Due to the electronic metal–support interaction, the heterostructure of Au SAs in the MXene support is significantly delocalized, resulting in a decreased energy barrier for the H$_2$O$_2$ breakdown into hydroxyl radicals. Simultaneously, nanoscale TiO$_2$ transported electrons for MXene, which is able to generate strong ECL signals, enabling an ultra-low LOD of 15.6 fM.

5.3.8 Others. There are also numerous inorganic and proteins in cells, blood, and organs that are significant clinical biochemical examination indicators. For instance, NO, as an endogenously produced signaling molecule, plays a variety of critical roles in biological systems and is linked to the pathogenesis of some diseases.[280] However, It is a chemically active species and has a short half-life of 6 s in physiological solutions. In order to in situ quickly detect NO in living cells, a miniaturized probe of penetrating a single cell is necessary.[281] Ni SAs anchored on N-doped hollow carbon spheres were developed and loaded on a flexible polydimethylsiloxane substrate to form a stretchable sensor, which can realize real-time NO monitoring in living cells (human umbilical vein endothelial cells) with a LOD of 1.8 nM (Fig. 29a).[37] FT-IR spectroscopy demonstrated that the adsorption of NO on Ni SAs belongs to the top and not to the bridged type. It indicates that Ni SAs can maintain their structure after adsorption of NO, and the sensor can well suppress the interference of nitrite (NO$_2^-$) after modification of Nafion. Besides, the deformation resistance/ original resistance changes very slightly after the sensor is stretched by 50%, indicating its strong mechanical stability and potential in biosensing applications (Fig. 29b and c).

Recent research shows that the concentrations of fractional exhaled NO (FeNO) are statistically different between COVID-19 patients and healthy individuals. To achieve portable and rapid NO detection, Deng's group selected the salen-derived Ni SACs with the lowest free energy for the determining step in the electrocatalytic oxidation of NO via DFT calculations (Fig. 29d– f).[282] Fabricated using screen printing technology (Fig. 29g), the Ni SAC-based sensor provided a low-cost NO detection method in a range of 0.3–180 ppb (covering the range of FeNO for humans), allowing for the primary screening of COVID-19 patients (Fig. 29h–j).

Additionally, SACs also show the potential in detecting other proteins, lipids, and even bacteria. For example, Co SACs can significantly increase the luminol CL emission by accelerating the deposition of H$_2$O$_2$ to produce a significant quantity of singlet oxygen.[265] As a sensitive CL probe, it is utilized to detect biological recognition processes like cardiac troponin I. Ni SACs can also serve as a sensitive ECL probe as they can generate abundant ROS without exogenous co-reactants.[283] Functionalized by highly hydrophilic PEG 2000, the aqueous dispersible Ni SACs can detect Staphylococcus aureus with a low LOD of 25 CFU mL^{-1} and a wide linear range of 73–73 × 10^6 CFU mL^{-1}. Another case is that the cholesterol of lipids can be detected using non-covalent nanoassembled Zn/Mo dual SACs based on polyoxometalates via ultraviolet/visible absorption spectra and can be kept for a year without performance degradation.[230]

6 Conclusions and outlook

In the past five years, the exploration of single-atom catalysts in design, synthesis and electronic structure has greatly promoted the development of sensors. The research discussed in this review provides a brief overview of the progress of single-atom catalyst-based sensors during the last few years. First, the working principles of the existing single-atom catalyst-based sensor are summarized, and the significant contribution of the single atom's intrinsic properties to increasing the sensitivity and selectivity of the sensor is methodically discussed. Second, preparation strategies of single-atom catalysts for sensor
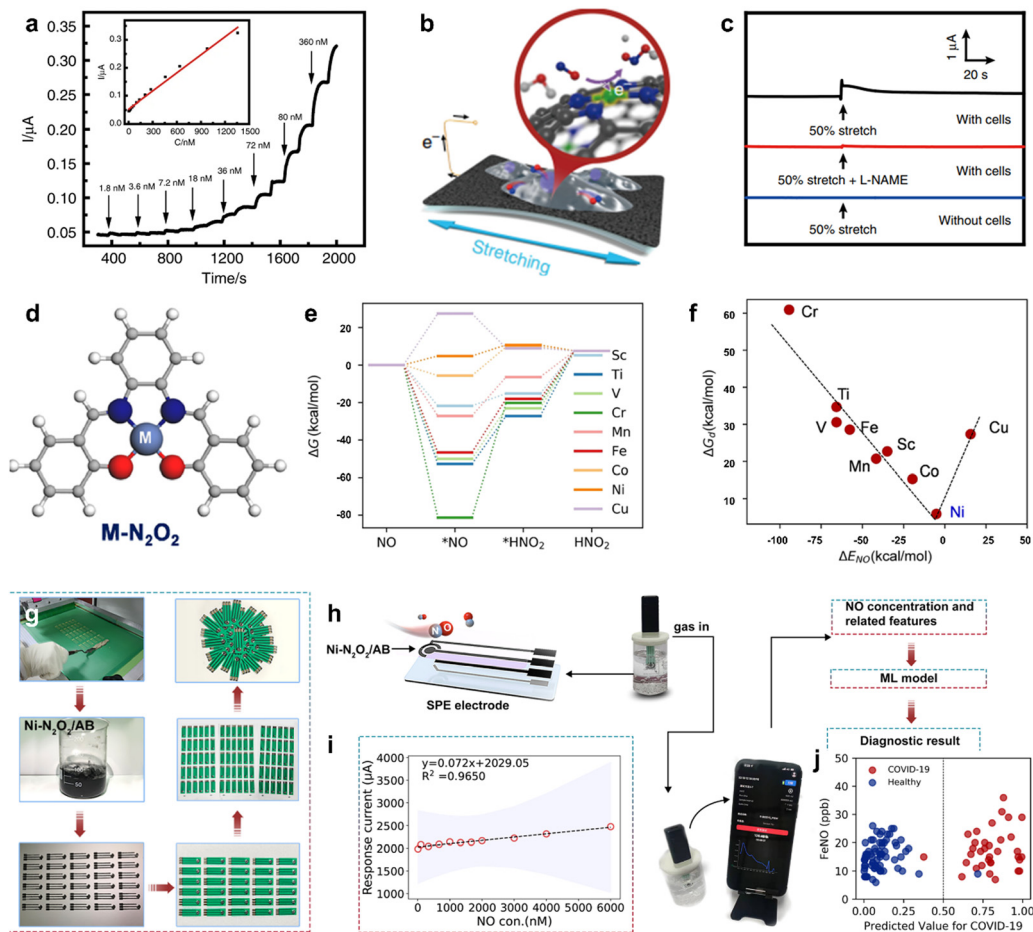
Fig. 29 (a) Chronoamperometric patterns of Ni SAC-based stretchable sensors when adding NO at 0.80 V. Inset: linear calibration. (b) Schematic illustration of the stretched Ni SAC-based sensor. (c) Real-time detection of NO produced from human umbilical vein endothelial cells when the sensor was subjected to 50% stretch moduli. Reproduced from ref. 37 with permission from Springer Nature, copyright 2020. (d) Schematic illustration of salen-derived SACs. M = Sc, Ti, V, Cr, Fe, Mn, Co, Ni, and Cu. (e) Free energy diagram of NO electrocatalytic oxidation on salen-derived SACs. (f) Relationship between the free energy of the rate-determining step (ΔG_d) and the binding energy of NO on the SACs (ΔE_{NO}). (g) Fabrication steps of the Ni SAC-based sensors *via* paper-printing. (h) Working principle of the FeNO detection analyzer based on Ni SACs. (i) The linear correlation between the NO concentration and response current signals using a FeNO detection analyzer. (j) FeNO produced by COVID-19 patients and healthy subjects and the value predicted by machine learning. When the value is larger than 0.50, the subjects are suspected to be COVID-19 patients. Reproduced from ref. 282 with permission from American Chemical Society, copyright 2022.

applications are presented. On this foundation, a wide range of examples, including the structure, location, coordination environments, and electronic structure of various single-atom catalysts for sensing gases, liquids, and biomolecules, are presented in detail. We suggest the following challenges for upcoming single-atom catalysts-based sensors:

(1) Analysis challenges. High sensitivity, strong selectivity and superb stability are the long-term goals of sensors. Although ideal sensing performance can be achieved in the laboratory, single-atom catalysts are still in the early stages of research in the face of a wide variety of application scenarios and analytes. Particularly, the inherently high surface energy of single metal atoms lead to their agglomeration into nanoparticles or clusters after long-term operation, especially with high metal loading, decreasing the sensitivity, selectivity and stability of the sensor. New strategies, including defect engineering or spatial confinement methods to anchor single

atoms, are expected to stabilize the synthesized single-atom sites to address these obstacles. At the same time, the origin of strong selectivity exhibited by single-atom catalysts is often unclear. This is unfavourable for designing more single-atom catalysts for sensors. *In situ* analysis technologies (*e.g.*, infrared spectroscopy, Raman spectroscopy, and XPS) are powerful in evaluating the catalytic conversion process of small molecules on the surface of catalyst, enabling the identification of the products or intermediates that are adsorbed and converted at the atomic sites, thereby improving selectivity *via* regulating reaction pathways and products.

(2) Technical challenges. The development of single-atom catalysts' synthesis strategies and characterization technologies has increased regulation over the sensing materials, including size, site, engineering defects, doping and functionalization. However, challenges still remain in the areas of single-atom loading, coordination environment control and batch

preparation. For instance, the anchored single atoms are usually in the micropores (<2 nm). The amount of such micropores has a significant impact on the loading capacity of the single atoms and the mass transfer of the analytes. Therefore, enriching the pore structure is also essential to raise the catalyst's efficiency.

Although single-atom catalysts have 100% atom utilization, their non-uniformity limits their application. The widely used catalysts with particles can be controlled uniformly in slurry. However, there might be an obvious difference between mass-produced electrodes modified using single-atom catalyst slurry, making it hard to meet the strict industrial production standards. Consequently, developing simpler and more reliable methods for the large-scale production of uniform single-atom catalysts is a challenge that needs more attention.

(3) Engineering and business challenges. Whether the industry would accept single-atom catalysts for their low manufacturing costs and high productivity is still a question. Typically, the preparation of a single-atom catalyst requires a series of process steps including a wet chemical process. The complexity and total relative cost of the equipment necessary in the preparation process must be taken into account, along with whether the waste liquid or waste gas created in this process can fulfil the industrial production standards. Thus, simplifying the single-atom catalysts' preparation process, incorporating chemical production processes and increasing yield are required for practical production.

It is also encouraging to note that the present industrialization of sensors differs from the conventional one due to less repetitive attempts of catalysts. It is expected to be accelerated by big data technology. On the one hand, single-atom catalysts' synthesis and structure can be guided and optimized by using machine learning techniques. On the other hand, artificial intelligence technology can make sensor arrays smarter to identify unknown targets.

Additionally, the advancement of micro-electromechanical systems or even nano-electromechanical system technology will offer a more promising way for enabling single-atom catalyst-based sensors to get smaller, consume less power consumption and cost less.

(4) Future health and safety challenges. The future development of single-atom catalyst-based sensors will also be impacted by ignored external considerations such as health and safety. For instance, if sensors based on single-atom catalysts are used for wearability, *in vivo* detection, agricultural detection, *etc.*, the users will be unavoidably concerned about the toxicity of nanomaterials. Developers must therefore ensure that the single-atom catalysts themselves are environmentally friendly in various application scenarios.

In general, the development of single-atom catalysts undoubtedly brings significant progress to sensors in terms of superior sensing performance, compact size, and affordable price, enabling the discovery of promising applications in the analysis of gases, liquids, and small biological molecules. Despite the fact that sensing research on single-atom catalysts is still in its infancy and faces challenges, the unique atom utilization and rich site diversity of single-atom catalysts are expected to solidify their position in the sensor field and be extensively used in the commercial market in the coming years.

Author contributions

The manuscript was written through the contributions of all authors. Z.H. Li and E.Z. Tian conceived the project and wrote the manuscript. S.L. Wang, M.Y. Ye, S.J. Li and Z.Y. Wang collected and sorted out data. Z. Ma, G.Y. Jiang and C. Tang edited and proofread the manuscript. Z.H. Li, K.H. Liu and J.K. Jiang supervised the project. All authors have approved the final version of the manuscript.

Conflicts of interest

There are no conflicts to declare.

Acknowledgements

Notes and references

1 M. Mayer and A. J. Baeumner, *Chem. Rev.*, 2019, **119**, 7996–8027.
2 L. Wang, Z. Lou, K. Jiang and G. Shen, *Adv. Intell. Syst.*, 2019, **1**, 1900040.
3 S. L. Ullo and G. R. Sinha, *Sensors*, 2020, **20**, 3113.
4 R. S. Andre, L. A. Mercante, M. H. M. Facure, R. C. Sanfelice, L. Fugikawa-Santos, T. M. Swager and D. S. Correa, *ACS Sens.*, 2022, **7**, 2104–2131.
5 A. Lewis and P. Edwards, *Nature*, 2016, **535**, 29–31.
6 J. van den Broek, S. Abegg, S. E. Pratsinis and A. T. Güntner, *Nat. Commun.*, 2019, **10**, 4220.
7 J. K. Norskov, *Rep. Prog. Phys.*, 1990, **53**, 1253–1295.
8 J. K. Norskov, *Prog. Surf. Sci.*, 1991, **38**, 103–144.
9 C. Lu, R. Fang and X. Chen, *Adv. Mater.*, 2020, **32**, 1906548.
10 X. Wu, H. Zhang, S. Zuo, J. Dong, Y. Li, J. Zhang and Y. Han, *Nano-Micro Lett.*, 2021, **13**, 136.
11 Y. Li, Y. Zhou, C. Shang, M. Yousaf, Z. Guo and S. Guo, *Acc. Mater. Res.*, 2022, **3**, 1160–1172.
12 H. Zhang, X. F. Lu, Z.-P. Wu and X. W. D. Lou, *ACS Cent. Sci.*, 2020, **6**, 1288–1301.
13 Y. Guo, M. Wang, Q. Zhu, D. Xiao and D. Ma, *Nat. Catal.*, 2022, **5**, 766–776.
14 A. Beniya and S. Higashi, *Nat. Catal.*, 2019, **2**, 590–602.

15 B. Qiao, A. Wang, X. Yang, L. F. Allard, Z. Jiang, Y. Cui, J. Liu, J. Li and T. Zhang, *Nat. Chem.*, 2011, **3**, 634–641.

16 X.-F. Yang, A. Wang, B. Qiao, J. Li, J. Liu and T. Zhang, *Acc. Chem. Res.*, 2013, **46**, 1740–1748.

17 N. Cheng, L. Zhang, K. Doyle-Davis and X. Sun, *Electrochem. Energy Rev.*, 2019, **2**, 539–573.

18 J. Shan, C. Ye, Y. Jiang, M. Jaroniec, Y. Zheng and S.-Z. Qiao, *Sci. Adv.*, 2022, **8**, eabo0762.

19 Z.-H. Xue, D. Luan, H. Zhang and X. W. Lou, *Joule*, 2022, **6**, 92–133.

20 A. Wang, J. Li and T. Zhang, *Nat. Rev. Chem.*, 2018, **2**, 65–81.

21 T. Zhang, A. G. Walsh, J. Yu and P. Zhang, *Chem. Soc. Rev.*, 2021, **50**, 569–588.

22 T. Chu, C. Rong, L. Zhou, X. Mao, B. Zhang and F. Xuan, *Adv. Mater.*, 2023, **35**, 2206783.

23 H. Zhang, G. Liu, L. Shi and J. Ye, *Adv. Energy Mater.*, 2018, **8**, 1701343.

24 R. Lang, X. Du, Y. Huang, X. Jiang, Q. Zhang, Y. Guo, K. Liu, B. Qiao, A. Wang and T. Zhang, *Chem. Rev.*, 2020, **120**, 11986–12043.

25 S. Mitchell and J. Pérez-Ramírez, *Nat. Rev. Mater.*, 2021, **6**, 969–985.

26 Q. Rong, B. Xiao, J. Zeng, R. Yu, B. Zi, G. Zhang, Z. Zhu, J. Zhang, J. Wu and Q. Liu, *ACS Sens.*, 2022, **7**, 199–206.

27 L. Jiao and H.-L. Jiang, *Chem*, 2019, **5**, 786–804.

28 C. Pan, F. Wu, J. Mao, W. Wu, G. Zhao, W. Ji, W. Ma, P. Yu and L. Mao, *J. Am. Chem. Soc.*, 2022, **144**, 14678–14686.

29 C. Liu, J. Qian, Y. Ye, H. Zhou, C.-J. Sun, C. Sheehan, Z. Zhang, G. Wan, Y.-S. Liu, J. Guo, S. Li, H. Shin, S. Hwang, T. B. Gunnoe, W. A. Goddard and S. Zhang, *Nat. Catal.*, 2021, **4**, 36–45.

30 Z. Jin, P. Li, Y. Meng, Z. Fang, D. Xiao and G. Yu, *Nat. Catal.*, 2021, **4**, 615–622.

31 J. Xi, H. S. Jung, Y. Xu, F. Xiao, J. W. Bae and S. Wang, *Adv. Funct. Mater.*, 2021, **31**, 2008318.

32 K. Rajeshwar and J. G. Ibanez, *Environmental electrochemistry: Fundamentals and applications in pollution sensors and abatement*, Elsevier, 1997.

33 R. Umapathi, S. M. Ghoreishian, S. Sonwal, G. M. Rani and Y. S. Huh, *Coord. Chem. Rev.*, 2022, **453**, 214305.

34 L. Jiao, W. Xu, Y. Wu, H. Wang, L. Hu, W. Gu and C. Zhu, *Anal. Chem.*, 2023, **95**, 433–443.

35 W. Qu, C. Chen, Z. Tang, H. Wen, L. Hu, D. Xia, S. Tian, H. Zhao, C. He and D. Shu, *Coord. Chem. Rev.*, 2023, **474**, 214855.

36 J. Wu, Y. Wu, L. Lu, D. Zhang and X. Wang, *Talanta Open*, 2021, **4**, 100075.

37 M. Zhou, Y. Jiang, G. Wang, W. Wu, W. Chen, P. Yu, Y. Lin, J. Mao and L. Mao, *Nat. Commun.*, 2020, **11**, 3188.

38 N. J. Ronkainen, H. B. Halsall and W. R. Heineman, *Chem. Soc. Rev.*, 2010, **39**, 1747–1763.

39 L. Yao, S. Gao, S. Liu, Y. Bi, R. Wang, H. Qu, Y. Wu, Y. Mao and L. Zheng, *ACS Appl. Mater. Interfaces*, 2020, **12**, 6268–6275.

40 J.-H. Lee, *Nat. Electron.*, 2020, **3**, 239–240.

41 Z. Xue, J.-J. Zheng, Y. Nishiyama, M.-S. Yao, Y. Aoyama, Z. Fan, P. Wang, T. Kajiwara, Y. Kubota, S. Horike, K.-I. Otake and S. Kitagawa, *Angew. Chem., Int. Ed.*, 2023, **62**, e202215234.

42 D.-H. Kim, S. Chong, C. Park, J. Ahn, J.-S. Jang, J. Kim and I.-D. Kim, *Adv. Mater.*, 2022, **34**, 2105869.

43 W.-T. Koo, J.-S. Jang and I.-D. Kim, *Chem*, 2019, **5**, 1938–1963.

44 J. Cao, Q. Chen, X. Wang, Q. Zhang, H.-D. Yu, X. Huang and W. Huang, *Research*, 2021, **2021**, 9863038.

45 X.-L. Ye, S.-J. Lin, J.-W. Zhang, H.-J. Jiang, L.-A. Cao, Y.-Y. Wen, M.-S. Yao, W.-H. Li, G.-E. Wang and G. Xu, *ACS Sens.*, 2021, **6**, 1103–1110.

46 N. Daelman, M. Capdevila-Cortada and N. López, *Nat. Mater.*, 2019, **18**, 1215–1221.

47 M. Xiong, Z. Gao and Y. Qin, *ACS Catal.*, 2021, **11**, 3159–3172.

48 G. M. Fernandes, W. R. Silva, D. N. Barreto, R. S. Lamarca, P. C. F. Lima Gomes, J. Flávio da, S. Petruci and A. D. Batista, *Anal. Chim. Acta*, 2020, **1135**, 187–203.

49 Q. H. Nguyen and M. I. Kim, *TrAC, Trends Anal. Chem.*, 2020, **132**, 116038.

50 D. Jiang, D. Ni, Z. T. Rosenkrans, P. Huang, X. Yan and W. Cai, *Chem. Soc. Rev.*, 2019, **48**, 3683–3704.

51 Y. Song, W. Wei and X. Qu, *Adv. Mater.*, 2011, **23**, 4215–4236.

52 L. Gao, J. Zhuang, L. Nie, J. Zhang, Y. Zhang, N. Gu, T. Wang, J. Feng, D. Yang, S. Perrett and X. Yan, *Nat. Nanotechnol.*, 2007, **2**, 577–583.

53 Q. Mu, Y. Sun, A. Guo, X. Xu, B. Qin and A. Cai, *J. Hazard. Mater.*, 2021, **402**, 123939.

54 K. Fan, J. Xi, L. Fan, P. Wang, C. Zhu, Y. Tang, X. Xu, M. Liang, B. Jiang, X. Yan and L. Gao, *Nat. Commun.*, 2018, **9**, 1440.

55 Y. Wang, Y.-J. Tang and K. Zhou, *J. Am. Chem. Soc.*, 2019, **141**, 14115–14119.

56 L. Jiao, H. Yan, Y. Wu, W. Gu, C. Zhu, D. Du and Y. Lin, *Angew. Chem., Int. Ed.*, 2020, **59**, 2565–2576.

57 Z. Li, F. Liu, Y. Jiang, P. Ni, C. Zhang, B. Wang, C. Chen and Y. Lu, *Nano Res.*, 2022, **15**, 4411–4420.

58 J. Wu, W. Liu, J. Ge, H. Zhang and P. Wang, *Chem. Soc. Rev.*, 2011, **40**, 3483–3495.

59 Y. Fan, S. Liu, Y. Yi, H. Rong and J. Zhang, *ACS Nano*, 2021, **15**, 2005–2037.

60 S. Qian, Z. Wang, Z. Zuo, X. Wang, Q. Wang and X. Yuan, *Coord. Chem. Rev.*, 2022, **451**, 214268.

61 G.-L. Yang, X.-L. Jiang, H. Xu and B. Zhao, *Small*, 2021, **17**, 2005327.

62 J.-C. G. Buenzli, *Coord. Chem. Rev.*, 2015, **293**, 19–47.

63 Y. Shu, Q. Ye, T. Dai, Q. Xu and X. Hu, *ACS Sens.*, 2021, **6**, 641–658.

64 S. Bao, H. Yu, G. Gao, H. Zhu, D. Wang, P. Zhu and G. Wang, *Nano Res.*, 2022, **15**, 3594–3605.

65 F. A. Bushira, S. A. Kitte, C. Xu, H. Li, L. Zheng, P. Wang and Y. Jin, *Anal. Chem.*, 2021, **93**, 9949–9957.

66 S. P. Usha, H. Manoharan, R. Deshmukh, R. Álvarez-Diduk, E. Calucho, V. V. R. Sai and A. Merkoçi, *Chem. Soc. Rev.*, 2021, **50**, 13012–13089.

67 Q. Wang, D. Zhang, Y. Chen, W.-F. Fu and X.-J. Lv, *ACS Sustainable Chem. Eng.*, 2019, **7**, 6430–6443.

68 J.-H. Zhang, W. Yang, M. Zhang, H.-J. Wang, R. Si, D.-C. Zhong and T.-B. Lu, *Nano Energy*, 2021, **80**, 105542.

69 W. Gu, H. Wang, L. Jiao, Y. Wu, Y. Chen, L. Hu, J. Gong, D. Du and C. Zhu, *Angew. Chem., Int. Ed.*, 2020, **59**, 3534–3538.

70 G. Maduraiveeran and W. Jin, *Trends Environ. Anal. Chem.*, 2017, **13**, 10–23.

71 G. Korotcenkov and B. K. Cho, *Sens. Actuators, B*, 2013, **188**, 709–728.

72 X. Ge, P. Zhou, Q. Zhang, Z. Xia, S. Chen, P. Gao, Z. Zhang, L. Gu and S. Guo, *Angew. Chem., Int. Ed.*, 2020, **59**, 232–236.

73 P.-H. Li, M. Yang, Z.-Y. Song, S.-H. Chen, X.-Y. Xiao, C.-H. Lin and X.-J. Huang, *Anal. Chem.*, 2021, **93**, 15115–15123.

74 K. Koga, *ACS Appl. Mater. Interfaces*, 2020, **12**, 20806–20823.

75 H. Bagheri, A. Hajian, M. Rezaei and A. Shirzadmehr, *J. Hazard. Mater.*, 2017, **324**, 762–772.

76 P.-H. Li, M. Yang, Y.-X. Li, Z.-Y. Song, J.-H. Liu, C.-H. Lin, J. Zeng and X.-J. Huang, *Anal. Chem.*, 2020, **92**, 6128–6135.

77 P. H. Li, Z. Y. Song, X. Y. Xiao, B. Liang, M. Yang, S. H. Chen, W. Q. Liu and X. J. Huang, *J. Hazard. Mater.*, 2023, **442**, 130122.

78 Z. Li, Y. Jiang, C. Liu, Z. Wang, Z. Cao, Y. Yuan, M. Li, Y. Wang, D. Fang, Z. Guo, D. Wang, G. Zhang and J. Jiang, *Environ. Sci.: Nano*, 2018, **5**, 1834–1843.

79 Y. Wang, Z. Zhang, G. Jia, L. Zheng, J. Zhao and X. Cui, *Chem. Commun.*, 2019, **55**, 5271–5274.

80 J. Yang, W. Li, D. Wang and Y. Li, *Small Struct.*, 2021, **2**, 2000051.

81 L. Sun, B. Wang and Y. Wang, *ACS Appl. Mater. Interfaces*, 2020, **12**, 21808–21817.

82 Y. Zhao, H. Zhou, X. Zhu, Y. Qu, C. Xiong, Z. Xue, Q. Zhang, X. Liu, F. Zhou, X. Mou, W. Wang, M. Chen, Y. Xiong, X. Lin, Y. Lin, W. Chen, H.-J. Wane, Z. Jiang, L. Zheng, T. Yao, J. Dong, S. Wei, W. Huang, L. Gu, J. Luo, Y. Li and Y. Wu, *Nat. Catal.*, 2021, **4**, 134–143.

83 Y. Yang, Y. Qian, H. Li, Z. Zhang, Y. Mu, D. Do, B. Zhou, J. Dong, W. Yan, Y. Qin, L. Fang, R. Feng, J. Zhou, P. Zhang, J. Dong, G. Yu, Y. Liu, X. Zhang and X. Fan, *Sci. Adv.*, 2020, **6**, eaba6586.

84 Z. Li, H. He, H. Cao, S. Sun, W. Diao, D. Gao, P. Lu, S. Zhang, Z. Guo, M. Li, R. Liu, D. Ren, C. Liu, Y. Zhang, Z. Yang, J. Jiang and G. Zhang, *Appl. Catal., B*, 2019, **240**, 112–121.

85 K. Mori, T. Murakami and H. Yamashita, *ACS Appl. Nano Mater.*, 2020, **3**, 10209–10217.

86 F. Wu, C. Pan, C.-T. He, Y. Han, W. Ma, H. Wei, W. Ji, W. Chen, J. Mao, P. Yu, D. Wang, L. Mao and Y. Li, *J. Am. Chem. Soc.*, 2020, **142**, 16861–16867.

87 H. Zhang, X. Zhang, Q. Sun, Q. He, H. Ji and X. He, *Chem. Eng. J.*, 2023, **455**, 140808.

88 C. Tang, Y. Jiao, B. Shi, J.-N. Liu, Z. Xie, X. Chen, Q. Zhang and S.-Z. Qiao, *Angew. Chem., Int. Ed.*, 2020, **59**, 9171–9176.

89 B. Liu, Q. Zhu, Y. Pan, F. Huang, L. Tang, C. Liu, Z. Cheng, P. Wang, J. Ma and M. Ding, *ACS Sens.*, 2022, **7**, 1533–1543.

90 S. Iqbal, B. Safdar, I. Hussain, K. Zhang and C. Chatzichristodoulou, *Adv. Energy Mater.*, 2023, 2203913, DOI: **10.1002/aenm.202203913**.

91 B. B. Sarma, J. Jelic, D. Neukum, D. E. Doronkin, X. Huang, F. Studt and J.-D. Grunwaldt, *J. Phys. Chem. C*, 2023, **127**, 3032–3046.

92 S. Wei, A. Li, J.-C. Liu, Z. Li, W. Chen, Y. Gong, Q. Zhang, W.-C. Cheong, Y. Wang, L. Zheng, H. Xiao, C. Chen, D. Wang, Q. Peng, L. Gu, X. Han, J. Li and Y. Li, *Nat. Nanotechnol.*, 2018, **13**, 856–861.

93 X. Bai, X. Zhao, Y. Zhang, C. Ling, Y. Zhou, J. Wang and Y. Liu, *J. Am. Chem. Soc.*, 2022, **144**, 17140–17148.

94 J. Yang, H. Qi, A. Li, X. Liu, X. Yang, S. Zhang, Q. Zhao, Q. Jiang, Y. Su, L. Zhang, J.-F. Li, Z.-Q. Tian, W. Liu, A. Wang and T. Zhang, *J. Am. Chem. Soc.*, 2022, **144**, 12062–12071.

95 B. Pattengale, Y. Huang, X. Yan, S. Yang, S. Younan, W. Hu, Z. Li, S. Lee, X. Pan, J. Gu and J. Huang, *Nat. Commun.*, 2020, **11**, 4114.

96 J.-C. Liu, Y. Tang, Y.-G. Wang, T. Zhang and J. Li, *Natl. Sci. Rev.*, 2018, **5**, 638–641.

97 H.-Y. Zhuo, X. Zhang, J.-X. Liang, Q. Yu, H. Xiao and J. Li, *Chem. Rev.*, 2020, **120**, 12315–12341.

98 J. Zhang, F. Lv, Z. Li, G. Jiang, M. Tan, M. Yuan, Q. Zhang, Y. Cao, H. Zheng, L. Zhang, C. Tang, W. Fu, C. Liu, K. Liu, L. Gu, J. Jiang, G. Zhang and S. Guo, *Adv. Mater.*, 2022, **34**, 2105276.

99 Q. Chen, Y. Liu, Y. Lu, Y. Hou, X. Zhang, W. Shi and Y. Huang, *J. Hazard. Mater.*, 2022, **422**, 126929.

100 Y. Hu, H. Li, Z. Li, B. Li, S. Wang, Y. Yao and C. Yu, *Green Chem.*, 2021, **23**, 8754–8794.

101 H. Li, L. Wang, Y. Dai, Z. Pu, Z. Lao, Y. Chen, M. Wang, X. Zheng, J. Zhu, W. Zhang, R. Si, C. Ma and J. Zeng, *Nat. Nanotechnol.*, 2018, **13**, 411–417.

102 J. Wu, H. Zhou, Q. Li, M. Chen, J. Wan, N. Zhang, L. Xiong, S. Li, B. Y. Xia, G. Feng, M. Liu and L. Huang, *Adv. Energy Mater.*, 2019, **9**, 1900149.

103 L. Zhao, Y. Zhang, L.-B. Huang, X.-Z. Liu, Q.-H. Zhang, C. He, Z.-Y. Wu, L.-J. Zhang, J. Wu, W. Yang, L. Gu, J.-S. Hu and L.-J. Wan, *Nat. Commun.*, 2019, **10**, 1278.

104 Q. Wang, X. Huang, Z. L. Zhao, M. Wang, B. Xiang, J. Li, Z. Feng, H. Xu and M. Gu, *J. Am. Chem. Soc.*, 2020, **142**, 7425–7433.

105 X. Hai, S. Xi, S. Mitchell, K. Harrath, H. Xu, D. F. Akl, D. Kong, J. Li, Z. Li, T. Sun, H. Yang, Y. Cui, C. Su, X. Zhao, J. Li, J. Perez-Ramirez and J. Lu, *Nat. Nanotechnol.*, 2022, **17**, 174–181.

106 C. Xia, Y. Qiu, Y. Xia, P. Zhu, G. King, X. Zhang, Z. Wu, J. Y. Kim, D. A. Cullen, D. Zheng, P. Li, M. Shakouri, E. Heredia, P. Cui, H. N. Alshareef, Y. Hu and H. Wang, *Nat. Chem.*, 2021, **13**, 887–894.

107 Y.-N. Gong, L. Jiao, Y. Qian, C.-Y. Pan, L. Zheng, X. Cai, B. Liu, S.-H. Yu and H.-L. Jiang, *Angew. Chem., Int. Ed.*, 2020, **59**, 2705–2709.

108 Y. Wang, A. Cho, G. Jia, X. Cui, J. Shin, I. Nam, K.-J. Noh, B. J. Park, R. Huang and J. W. Han, *Angew. Chem., Int. Ed.*, 2023, **62**, e202300119.

109 Z. Zhang, C. Feng, C. Liu, M. Zuo, L. Qin, X. Yan, Y. Xing, H. Li, R. Si, S. Zhou and J. Zeng, *Nat. Commun.*, 2020, **11**, 1215.

110 S. Zhao, G. Chen, G. Zhou, L.-C. Yin, J.-P. Veder, B. Johannessen, M. Saunders, S.-Z. Yang, R. D. Marco, C. Liu and S. P. Jiang, *Adv. Funct. Mater.*, 2020, **30**, 1906157.

111 H. Shin, J. Ko, C. Park, D.-H. Kim, J. Ahn, J.-S. Jang, Y. H. Kim, S.-H. Cho, H. Baik and I.-D. Kim, *Adv. Funct. Mater.*, 2022, **32**, 2110485.

112 H. Li, M. Sun, H. Gu, J. Huang, G. Wang, R. Tan, R. Wu, X. Zhang, S. Liu, L. Zheng, W. Chen and Z. Chen, *Small*, 2023, 2207036, DOI: 10.1002/smll.202207036.

113 F. Yang, X. Mao, M. Ma, C. Jiang, P. Zhang, J. Wang, Q. Deng, Z. Zeng and S. Deng, *Carbon*, 2020, **168**, 528–535.

114 H. Yang, L. Shang, Q. Zhang, R. Shi, G. I. N. Waterhouse, L. Gu and T. Zhang, *Nat. Commun.*, 2019, **10**, 4585.

115 X. He, Y. Deng, Y. Zhang, Q. He, D. Xiao, M. Peng, Y. Zhao, H. Zhang, R. Luo, T. Gan, H. Ji and D. Ma, *Cell Rep. Phys. Sci.*, 2020, **1**, 100004.

116 T. Gan, Q. He, H. Zhang, H. Xiao, Y. Liu, Y. Zhang, X. He and H. Ji, *Chem. Eng. J.*, 2020, **389**, 124490.

117 G.-F. Han, F. Li, A. I. Rykov, Y.-K. Im, S.-Y. Yu, J.-P. Jeon, S.-J. Kim, W. Zhou, R. Ge, Z. Ao, T. J. Shin, J. Wang, H. Y. Jeong and J.-B. Baek, *Nat. Nanotechnol.*, 2022, **17**, 403–407.

118 Y. Li, S. Wang, X.-S. Wang, Y. He, Q. Wang, Y. Li, M. Li, G. Yang, J. Yi, H. Lin, D. Huang, L. Li, H. Chen and J. Ye, *J. Am. Chem. Soc.*, 2020, **142**, 19259–19267.

119 F. Xie, X. Cui, X. Zhi, D. Yao, B. Johannessen, T. Lin, J. Tang, T. B. F. Woodfield, L. Gu and S.-Z. Qiao, *Nat. Synth.*, 2023, **2**, 129–139.

120 C.-X. Zhao, J.-N. Liu, J. Wang, C. Wang, X. Guo, X.-Y. Li, X. Chen, L. Song, B.-Q. Li and Q. Zhang, *Sci. Adv.*, 2022, **8**, eabn5091.

121 Z. Li, B. Li and C. Yu, *Adv. Mater.*, 2023, e2211221, DOI: 10.1002/adma.202211221,.

122 Z. Li, B. Li, Y. Hu, X. Liao, H. Yu and C. Yu, *Small Struct.*, 2022, **3**, 2200041.

123 W. Che, T. Tao and J.-B. Baek, *J. Mater. Chem. A*, 2022, **10**, 10297–10325.

124 J. Fu, J. Dong, R. Si, K. Sun, J. Zhang, M. Li, N. Yu, B. Zhang, M. G. Humphrey, Q. Fu and J. Huang, *ACS Catal.*, 2021, **11**, 1952–1961.

125 G. Xiao, R. Lu, J. Liu, X. Liao, Z. Wang and Y. Zhao, *Nano Res.*, 2022, **15**, 3073–3081.

126 Y. Hu, Z. Li, B. Li and C. Yu, *Small*, 2022, **18**, 2203589.

127 W. Guo, Z. Wang, X. Wang and Y. Wu, *Adv. Mater.*, 2021, **33**, 2004287.

128 H. C. Kolb, M. G. Finn and K. B. Sharpless, *Angew. Chem., Int. Ed.*, 2001, **40**, 2004–2021.

129 H. Zhang, W. Cheng, D. Luan and X. W. Lou, *Angew. Chem., Int. Ed.*, 2021, **60**, 13177–13196.

130 T. L. Guidotti, *Environ. Res.*, 1978, **15**, 443–472.

131 Z. Xue, M. Yan, X. Yu, Y. Tong, H. Zhou, Y. Zhao, Z. Wang, Y. Zhang, C. Xiong, J. Yang, X. Hong, J. Luo, Y. Lin, W. Huang, Y. Li and Y. Wu, *Chem*, 2020, **6**, 3364–3373.

132 R. Tian, S. Wang, X. Hu, J.-G. Zheng, P. Ji, J. Lin, J. Zhang, M. Xu, J. Bao, S. Zuo, H. Zhang, W. Zhang, J. Wang and L. Yu, *J. Mater. Chem. A*, 2020, **8**, 23784–23794.

133 W. M. Chen, P. P. Li, J. Yu, P. X. Cui, X. H. Yu, W. G. Song and C. Y. Cao, *Nano Res.*, 2022, **15**, 9544–9553.

134 X. Geng, S. Li, L. Mawella-Vithanage, T. Ma, M. Kilani, B. Wang, L. Ma, C. C. Hewa-Rahinduwage, A. Shafikova, E. Nikolla, G. Mao, S. L. Brock, L. Zhang and L. Luo, *Nat. Commun.*, 2021, **12**, 4895.

135 S. Y. Choi, Y. Kim, H.-S. Chung, A. R. Kim, J.-D. Kwon, J. Park, Y. L. Kim, S.-H. Kwon, M. G. Hahm and B. Cho, *ACS Appl. Mater. Interfaces*, 2017, **9**, 3817–3823.

136 B. Liu, L. Zhang, Y. Luo, L. Gao and G. Duan, *Small*, 2021, **17**, 2105643.

137 R. Zhang, Z. Deng, L. Shi, M. Kumar, J. Chang, S. Wang, X. Fang, W. Tong and G. Meng, *ACS Appl. Mater. Interfaces*, 2022, **14**, 24536–24545.

138 Z. Xue, C. Wang, Y. Tong, M. Yan, J. Zhang, X. Han, X. Hong, Y. Li and Y. Wu, *CCS Chem.*, 2022, **4**, 3842–3851.

139 Y. Li, Y. Yang, K. Li, Y. Wang, P. Ning and X. Sun, *Chem. Phys. Lett.*, 2021, **769**, 138338.

140 R. Tian, P. Ji, Z. Luo, J. Li and J. Sun, *New J. Chem.*, 2021, **45**, 10240–10247.

141 L. Liu, P. Zhou, X. Su, Y. Liu, Y. Sun, H. Yang, H. Fu, X. Qu, S. Liu and S. Zheng, *Sens. Actuators, B*, 2022, **351**, 130983.

142 T. Yokoyama, S. Terada, S. Yagi, A. Imanishi, S. Takenaka, Y. Kitajima and T. Ohta, *Surf. Sci.*, 1995, **324**, 25–34.

143 N. K. Das and W. A. Saidi, *J. Chem. Phys.*, 2017, **146**, 154701.

144 F. Gu, Y. Cui, D. Han, S. Hong, M. Flytzani-Stephanopoulos and Z. Wang, *Appl. Catal., B*, 2019, **256**, 117809.

145 Y. Xu, W. Zheng, X. Liu, L. Zhang, L. Zheng, C. Yang, N. Pinna and J. Zhang, *Mater. Horiz.*, 2020, **7**, 1519–1527.

146 J. Zeng, Q. Rong, B. Xiao, R. Yu, B. Zi, X. Kuang, X. Deng, Y. Ma, J. Zhang, J. Wu and Q. Liu, *J. Mater. Chem. A*, 2021, **9**, 8704–8710.

147 J. Xiang, Y. Su, L. Zhang, S. Hong, Z. Wang, D. Han and F. Gu, *ACS Appl. Mater. Interfaces*, 2022, **14**, 13440–13449.

148 F. B. Gu, Y. Su, S. Hong, J. F. Wang, P. H. Wang, D. M. Han, Z. H. Wang, Z. H. Qiao and Y. L. Hu, *Sens. Actuators, B*, 2022, **372**, 132632.

149 B. Zong, Q. Xu and S. Mao, *ACS Sens.*, 2022, **7**, 1874–1882.

150 T. T. Dai, Z. Yan, M. Li, Y. L. Han, Z. H. Deng, S. M. Wang, R. Y. Wang, X. H. Xu, L. Shi, W. Tong, J. Bao, Z. H. Qiao, L. Li and G. Meng, *Small Methods*, 2022, **6**, 2200728.

151 S.-X. L. Luo, C.-J. Lin, K. H. Ku, K. Yoshinaga and T. M. Swager, *ACS Nano*, 2020, **14**, 7297–7307.

152 United States Department of Labor., Permissible Exposure Limits – Annotated Tables, https://www.osha.gov/annotated-pels/table-z-1, (accessed March 1, 2022).

153 F. Gu, C. Luo, D. Han, S. Hong and Z. Wang, *Sens. Actuators, B*, 2019, **297**, 126772.

154 F. Gu, M. Di, D. Han, S. Hong and Z. Wang, *ACS Sens.*, 2020, **5**, 2611–2619.

155 H. Shin, W.-G. Jung, D.-H. Kim, J.-S. Jang, Y. H. Kim, W.-T. Koo, J. Bae, C. Park, S.-H. Cho, B. J. Kim and I.-D. Kim, *ACS Nano*, 2020, **14**, 11394–11405.

156 M. Yan, X. Gao, X. Han, D. Zhou, Y. Lin, W. Chen, Z. Xue and Y. Wu, *Small Struct.*, 2023, 2200248, DOI: 10.1002/sstr.202200248.

157 J. Qiu, X. Hu, L. Shi, J. Fan, X. Min, W. Zhang and J. Wang, *Sens. Actuators, B*, 2021, **329**, 129221.

158 Q. Li, Z. Li, Q. Zhang, L. Zheng, W. Yan, X. Liang, L. Gu, C. Chen, D. Wang, Q. Peng and Y. Li, *Nano Res.*, 2021, **14**, 1435–1442.

159 I. Y. Habib, A. A. Tajuddin, H. A. Noor, C. M. Lim, A. H. Mahadi and N. T. R. N. Kumara, *Sci. Rep.*, 2019, **9**, 9207.

160 H. W. Kim, M. B. Ross, N. Kornienko, L. Zhang, J. Guo, P. Yang and B. D. McCloskey, *Nat. Catal.*, 2018, **1**, 282–290.

161 X. Shi, S. Siahrostami, G.-L. Li, Y. Zhang, P. Chakthranont, F. Studt, T. F. Jaramillo, X. Zheng and J. K. Nørskov, *Nat. Commun.*, 2017, **8**, 701.

162 R. A. B. Silva, R. H. O. Montes, E. M. Richter and R. A. A. Munoz, *Food Chem.*, 2012, **133**, 200–204.

163 Q. Chen, T. Lin, J. Huang, Y. Chen, L. Guo and F. Fu, *Anal. Methods*, 2018, **10**, 504–507.

164 R. Liu, S. Li, X. Yu, G. Zhang, S. Zhang, J. Yao, B. Keita, L. Nadjo and L. Zhi, *Small*, 2012, **8**, 1398–1406.

165 K. Jiang, S. Back, A. J. Akey, C. Xia, Y. Hu, W. Liang, D. Schaak, E. Stavitski, J. K. Nørskov, S. Siahrostami and H. Wang, *Nat. Commun.*, 2019, **10**, 3997.

166 L. Wang, H. Shen, S. Gao, X. Mamat and G. Hu, *J. Electrochem. Soc.*, 2018, **165**, H348–H352.

167 J. Li, C. Wu, C. Yuan, Z. Shi, K. Zhang, Z. Zou, L. Xiong, J. Chen, Y. Jiang, W. Sun, K. Tang, H. Yang and C. M. Li, *Anal. Chem.*, 2022, **94**, 14109–14117.

168 Z. Li, G. Jiang, Y. Wang, M. Tan, Y. Cao, E. Tian, L. Zhang, X. Chen, M. Zhao, Y. Jiang, Y. Luo, Y. Zheng, Z. Ma, D. Wang, W. Fu, K. Liu, C. Tang and J. Jiang, *Environ. Sci.: Nano*, 2022, **9**, 1759–1769.

169 Z. Li, R. Liu, C. Tang, Z. Wang, X. Chen, Y. Jiang, C. Wang, Y. Yuan, W. Wang, D. Wang, S. Chen, X. Zhang, Q. Zhang and J. Jiang, *Small*, 2020, **16**, 1902860.

170 Y. Shu, Z. Li, Y. Yang, J. Tan, Z. Liu, Y. Shi, C. Ye and Q. Gao, *ACS Appl. Nano Mater.*, 2021, **4**, 7954–7962.

171 Y. Hu, C. Bai, M. Li, M. Hojamberdiev, D. Geng and X. Li, *J. Mater. Chem. A*, 2022, **10**, 3190–3200.

172 X. Gao, W. Ma, J. Mao, C.-T. He, W. Ji, Z. Chen, W. Chen, W. Wu, P. Yu and L. Mao, *Chem. Sci.*, 2021, **12**, 15045–15053.

173 Z. Lin, L. Zheng, W. Yao, S. Liu, Y. Bu, Q. Zeng, X. Zhang, H. Deng, X. Lin and W. Chen, *J. Mater. Chem. B*, 2020, **8**, 8599–8606.

174 Y. Zuo, C. Liu, L. Ding, R. Qiao, J. Tian, C. Liu, Q. Wang, G. Xue, Y. You, Q. Guo, J. Wang, Y. Fu, K. Liu, X. Zhou, H. Hong, M. Wu, X. Lu, R. Yang, G. Zhang, D. Yu, E. Wang, X. Bai, F. Ding and K. Liu, *Nat. Commun.*, 2022, **13**, 1007.

175 Y. Luo, D. Wu, Z. Li, X.-Y. Li, Y. Wu, S.-P. Feng, C. Menon, H. Chen and P. K. Chu, *SmartMat*, 2022, **3**, 491–502.

176 K. H. Vardhan, P. S. Kumar and R. C. Panda, *J. Mol. Liq.*, 2019, **290**, 111197.

177 J. O. Duruibe, M. O. C. Ogwuegbu and J. N. Egwurugwu, *Int. J. Phys. Sci.*, 2007, **2**, 112–118.

178 Y. Li, P. Bai, Y. Yan, W. Yan, W. Shi and R. Xu, *Microporous Mesoporous Mater.*, 2019, **273**, 203–211.

179 R. Li, X. He, R. Javed, J. Cai, H. Cao, X. Liu, Q. Chen, D. Ye and H. Zhao, *Sci. Total Environ*, 2022, **834**, 155428.

180 M. Ferrandon, A. J. Kropf, D. J. Myers, K. Artyushkova, U. Kramm, P. Bogdanoff, G. Wu, C. M. Johnston and P. Zelenay, *J. Phys. Chem. C*, 2012, **116**, 16001–16013.

181 Y. Mao, S. Gao, L. Yao, L. Wang, H. Qu, Y. Wu, Y. Chen and L. Zheng, *J. Hazard. Mater.*, 2021, **408**, 124898.

182 G. C. Song, Q. Zhang, S. Liang, Y. Yao, M. L. Feng, Z. Majid, X. Y. He, K. L. Huang, J. C. Li and N. Cheng, *J. Mater. Chem. C*, 2022, **10**, 15656–15663.

183 G. Song, J.-C. Li, Z. Majid, W. Xu, X. He, Z. Yao, Y. Luo, K. Huang and N. Cheng, *Food Chem.*, 2022, **390**, 133127.

184 X. Li, S. C. Ding, Z. Y. Lyu, P. Tieu, M. Y. Wang, Z. X. Feng, X. Q. Pan, Y. Zhou, X. H. Niu, D. Du, W. L. Zhu and Y. H. Lin, *Small*, 2022, **18**, 2203001.

185 J. Podgorski and M. Berg, *Science*, 2020, **368**, 845–850.

186 Y. Kong, T. Wu, D. Wu, Y. Zhang, Y. Wang, B. Du and Q. Wei, *Anal. Methods*, 2018, **10**, 4784–4792.

187 W.-Y. Zhou, S.-S. Li, X.-Y. Xiao, S.-H. Chen, J.-H. Liu and X.-J. Huang, *Chem. Commun.*, 2018, **54**, 9329–9332.

188 Y.-Y. Li, Z.-Y. Song, X.-Y. Xiao, L.-K. Zhang, H.-Q. Huang, W.-Q. Liu and X.-J. Huang, *J. Hazard. Mater.*, 2022, **435**, 129009.

189 V. A. DeLeo, *Dermatitis*, 2006, **17**, 53–55.

190 G. K. Sidhu, S. Singh, V. Kumar, D. S. Dhanjal, S. Datta and J. Singh, *Crit. Rev. Environ. Sci. Technol.*, 2019, **49**, 1135–1187.

191 Z. Zeng, B. Song, R. Xiao, G. Zeng, J. Gong, M. Chen, P. Xu, P. Zhang, M. Shen and H. Yi, *Environ. Int.*, 2019, **126**, 598–610.

192 T. Chen, D. Zhou, S. Hou, Y. Li, Y. Liu, M. Zhang, G. Zhang and H. Xu, *Anal. Chem.*, 2022, **94**, 15270–15279.

193 L. Jiao, J. Wu, H. Zhong, Y. Zhang, W. Xu, Y. Wu, Y. Chen, H. Yan, Q. Zhang, W. Gu, L. Gu, S. P. Beckman, L. Huang and C. Zhu, *ACS Catal.*, 2020, **10**, 6422–6429.

194 J. Ge, L. Yang, Z. Li, Y. Wan, D. Mao, R. Deng, Q. Zhou, Y. Yang and W. Tan, *J. Hazard. Mater.*, 2022, **436**, 129199.

195 L. Jiao, W. Xu, Y. Zhang, Y. Wu, W. Gu, X. Ge, B. Chen, C. Zhu and S. Guo, *Nano Today*, 2020, **35**, 100971.

196 L. Jiao, Y. Kang, Y. Chen, N. Wu, Y. Wu, W. Xu, X. Wei, H. Wang, W. Gu, L. Zheng, W. Song and C. Zhu, *Nano Today*, 2021, **40**, 101261.

197 G. Song, J. Zhang, H. Huang, X. Wang, X. He, Y. Luo, J.-C. Li, K. Huang and N. Cheng, *Food Chem.*, 2022, **387**, 132896.

198 Z. Lyu, S. C. Ding, P. Tieu, L. Z. Fang, X. Li, T. Li, X. Q. Pan, M. H. Engelhard, X. F. Ruan, D. Du, S. Q. Li and Y. H. Lin, *Research*, 2022, **2022**, 9823290.

199 S. Luo, J. Q. Gao, Y. Chen, H. Ouyang, L. Wang and Z. F. Fu, *Talanta*, 2022, **250**, 123732.

200 S. Luo, J. Q. Gao, J. X. Xian, H. Ouyang, L. Wang and Z. F. Fu, *Anal. Chem.*, 2022, **94**, 13533–13539.

201 J. X. Xian, S. Luo, J. X. Xue, L. X. Zhang, Z. F. Fu and H. Ouyang, *Anal. Chem.*, 2022, **94**, 11449–11456.

202 X. Luo, Z. Luo, X. Wei, L. Jiao, Q. Fang, H. Wang, J. Wang, W. Gu, L. Hu and C. Zhu, *Anal. Chem.*, 2022, **94**, 1390–1396.

203 Y. Qin, J. Wen, X. Wang, L. Jiao, X. Wei, H. Wang, J. Li, M. Liu, L. Zheng, L. Hu, W. Gu and C. Zhu, *ACS Nano*, 2022, **16**, 2997–3007.

204 L. N. Vandenberg, R. Hauser, M. Marcus, N. Olea and W. V. Welshons, *Reprod. Toxicol.*, 2007, **24**, 139–177.

205 J. R. Rochester, *Reprod. Toxicol.*, 2013, **42**, 132–155.

206 M. Li, X. Peng, X. Liu, H. Wang, S. Zhang and G. Hu, *RSC Adv.*, 2021, **11**, 28988–28995.

207 M. Feng, Q. Zhang, X. Chen, D. Deng, X. Xie and X. Yang, *Biosens. Bioelectron.*, 2022, **210**, 114294.

208 X. Chen, M. Feng, X. Xie, Y. Zhang, J. Zhang and X. Yang, *Talanta*, 2022, **246**, 123487.

209 G. Kang, W. D. Liu, F. N. Liu, Z. Li, X. Y. Dong, C. X. Chen and Y. Z. Lu, *Chem. Eng. J.*, 2022, **449**, 137855.

210 W. Cong, P. Song, Y. Zhang, S. Yang, W. Liu, T. Zhang, J. Zhou, M. Wang and X. Liu, *J. Hazard. Mater.*, 2022, **437**, 129327.

211 D. Li, C. Li, H. Wang, J. Li, Y. Zhao, X. Jiang, G. Wen, A. Liang and Z. Jiang, *Microchim. Acta*, 2021, **188**, 175.

212 K. Magulova and A. Priceputu, *Environ. Pollut.*, 2016, **217**, 82–84.

213 J. Liu, X. Wang, F. Ma, X. Yang, Y. Liu, X. Zhang, S. Guo, Z. Wang, S. Yang and R. Zhao, *Chem. Eng. J.*, 2022, **435**, 134966.

214 S. Ding, Z. Lyu, L. Fang, T. Li, W. Zhu, S. Li, X. Li, J.-C. Li, D. Du and Y. Lin, *Small*, 2021, **17**, 2100664.

215 Z. Lyu, S. Ding, M. Wang, X. Pan, Z. Feng, H. Tian, C. Zhu, D. Du and Y. Lin, *Nano-Micro Lett.*, 2021, **13**, 146.

216 L. Wang, J. Xue, J. Chang, C. Yu, H. Dai, Z. Yao, J. Zhou, G. Sun and W. Huang, *J. Mater. Sci.*, 2021, **56**, 13579–13589.

217 Y. Fan, X. Gan, H. Zhao, Z. Zeng, W. You and X. Quan, *Chem. Eng. J.*, 2022, **427**, 131572.

218 L. L. Lu, X. H. Hu, R. J. Zeng, Q. Y. Lin, X. Huang, M. J. Li and D. P. Tang, *Anal. Chim. Acta*, 2022, **1229**, 340383.

219 Y. Wu, J. Wu, L. Jiao, W. Xu, H. Wang, X. Wei, W. Gu, G. Ren, N. Zhang, Q. Zhang, L. Huang, L. Gu and C. Zhu, *Anal. Chem.*, 2020, **92**, 3373–3379.

220 Y. Lin, F. Wang, J. Yu, X. Zhang and G.-P. Lu, *J. Hazard. Mater.*, 2022, **425**, 127763.

221 S. M. Roberts and A. J. Gibb, in *Introduction to Biological and Small Molecule Drug Research and Development*, ed. R. Ganellin, S. Roberts and R. Jefferis, Elsevier, Oxford, 2013, pp. 1–55, DOI: 10.1016/B978-0-12-397176-0.00001-7.

222 B. Halliwell, *J. Neurochem.*, 2006, **97**, 1634–1658.

223 S. G. Rhee, *Science*, 2006, **312**, 1882–1883.

224 B. Dou, J. Yang, R. Yuan and Y. Xiang, *Anal. Chem.*, 2018, **90**, 5945–5950.

225 L. Jiao, W. Xu, H. Yan, Y. Wu, C. Liu, D. Du, Y. Lin and C. Zhu, *Anal. Chem.*, 2019, **91**, 11994–11999.

226 Y. Liang, P. Zhao, J. L. Zheng, Y. Y. Chen, Y. Y. Liu, J. Zheng, X. G. Luo, D. Q. Huo and C. J. Hou, *ACS Appl. Nano Mater.*, 2022, **5**, 11852–11863.

227 X. Wei, S. Song, W. Song, W. Xu, L. Jiao, X. Luo, N. Wu, H. Yan, X. Wang, W. Gu, L. Zheng and C. Zhu, *Anal. Chem.*, 2021, **93**, 5334–5342.

228 Y. Liu, J. Yan, Y. Huang, Z. Sun, H. Zhang, L. Fu, X. Li and Y. Jin, *Front. Bioeng. Biotechnol.*, 2022, **9**, 790849.

229 N. Cheng, J.-C. Li, D. Liu, Y. Lin and D. Du, *Small*, 2019, **15**, 1901485.

230 C.-B. Ma, Y. Xu, L. Wu, Q. Wang, J.-J. Zheng, G. Ren, X. Wang, X. Gao, M. Zhou, M. Wang and H. Wei, *Angew. Chem., Int. Ed.*, 2022, **61**, e202116170.

231 Z. Zou, Z. Z. Shi, J. G. Wu, C. Wu, Q. X. Zeng, Y. Y. Zhang, G. D. Zhou, X. S. Wu, J. Li, H. Chen, H. B. Yang and C. M. Li, *Anal. Chem.*, 2021, **93**, 10789–10797.

232 S. Raha and B. H. Robinson, *Trends Biochem. Sci.*, 2000, **25**, 502–508.

233 S. Prasad, S. C. Gupta and A. K. Tyagi, *Cancer Lett.*, 2017, **387**, 95–105.

234 C. Zuccarella-Hackl, R. von Känel, L. Thomas, M. Hauser, U. Kuebler, H. R. Widmer and P. H. Wirtz, *Psychosom. Med.*, 2016, **78**, 750–757.

235 X. Wu, Y. Sun, T. He, Y. Zhang, G.-J. Zhang, Q. Liu and S. Chen, *Langmuir*, 2021, **37**, 11309–11315.

236 Y. Song, T. He, Y. Zhang, C. Yin, Y. Chen, Q. Liu, Y. Zhang and S. Chen, *J. Electroanal. Chem.*, 2022, **906**, 116024.

237 B. Long, Y. Zhao, P. Cao, W. Wei, Y. Mo, J. Liu, C.-J. Sun, X. Guo, C. Shan and M.-H. Zeng, *Anal. Chem.*, 2022, **94**, 1919–1924.

238 B. Long, P. Cao, Y. Zhao, Q. Fu, Y. Mo, Y. Zhai, J. Liu, X. Lyu, T. Li, X. Guo, C. Shan and M. Zeng, *Nano Res.*, 2023, **16**, 318–324.

239 H. Yan, L. Jiao, H. Wang, Y. Zhu, Y. Chen, L. Shuai, M. Gu, M. Qiu, W. Gu and C. Zhu, *Sens. Actuators, B*, 2021, **343**, 130108.

240 Q. H. Nguyen, D. H. Lee, P. T. Nguyen, P. G. Le and M. I. Kim, *Chem. Eng. J.*, 2023, **454**, 140541.

241 X. Luo, M. Yan, W. Song, Q. Fang, X. Wei, L. Jiao, W. Xu, Y. Kang, H. Wang, N. Wu, W. Gu, L. Zheng, L. Hu and C. Zhu, *Adv. Funct. Mater.*, 2021, **31**, 2101193.

242 X. Zhou, M. Wang, J. Chen, X. Xie and X. Su, *Anal. Chim. Acta*, 2020, **1128**, 72–79.

243 F. X. Hu, T. Hu, S. Chen, D. Wang, Q. Rao, Y. Liu, F. Dai, C. Guo, H. B. Yang and C. M. Li, *Nano-Micro Lett.*, 2021, **13**, 7.

244 Q. Wang, X. Wen and J. Kong, *Crit. Rev. Anal. Chem.*, 2020, **50**, 359–375.

245 X. Liu and J. Liu, *View*, 2021, **2**, 20200102.

246 Y. Lei, D. Butler, M. C. Lucking, F. Zhang, T. Xia, K. Fujisawa, T. Granzier-Nakajima, R. Cruz-Silva, M. Endo, H. Terrones, M. Terrones and A. Ebrahimi, *Sci. Adv.*, 2020, **6**, eabc4250.

247 X. Sun, C. Chen, C. Xiong, C. Zhang, X. Zheng, J. Wang, X. Gao, Z.-Q. Yu and Y. Wu, *Nano Res.*, 2023, **16**, 917–924.

248 X. Xie, D. P. Wang, C. Guo, Y. Liu, Q. Rao, F. Lou, Q. Li, Y. Dong, Q. Li, H. B. Yang and F. X. Hu, *Anal. Chem.*, 2021, **93**, 4916–4923.

249 F. A. Bushira, S. A. Kitte, H. Li, L. Zheng, P. Wang and Y. Jin, *J. Electroanal. Chem.*, 2022, **904**, 115956.

250 P. Calabresi, B. Picconi, L. Parnetti and M. Di Filippo, *Lancet Neurol.*, 2006, **5**, 974–983.

251 J. Luo, K. Mills, S. le Cessie, R. Noordam and D. van Heemst, *Ageing Res. Rev.*, 2020, **57**, 100982.

252 R. González de Vega, M. L. Fernández-Sánchez, J. C. Fernández, F. V. Álvarez Menéndez and A. Sanz-Medel, *J. Trace Elem. Med. Biol.*, 2016, **37**, 44–49.

253 N. Allocati, M. Masulli, C. Di Ilio and L. Federici, *Oncogenesis*, 2018, **7**, 8.

254 J. Zhang, Z. Li, H. Li, G. Dai, F. Luo, Z. Chu, X. Geng, F. Zhang and Q. Wang, *Nanoscale Res. Lett.*, 2022, **17**, 54.

255 L. Sun, Y. Yan, S. Chen, Z. Zhou, W. Tao, C. Li, Y. Feng and F. Wang, *Anal. Bioanal. Chem.*, 2022, **414**, 1857–1865.

256 L. Shen, M. A. Khan, X. Wu, J. Cai, T. Lu, T. Ning, Z. Liu, W. Lu, D. Ye, H. Zhao and J. Zhang, *Biosens. Bioelectron.*, 2022, **205**, 114097.

257 W. Gu, X. Wang, J. Wen, S. Cao, L. Jiao, Y. Wu, X. Wei, L. Zheng, L. Hu, L. Zhang and C. Zhu, *Anal. Chem.*, 2021, **93**, 8663–8670.

258 C. I. Ghanem, M. J. Pérez, J. E. Manautou and A. D. Mottino, *Pharmacol. Res.*, 2016, **109**, 119–131.

259 W. Wu, L. Huang, X. Zhu, J. Chen, D. Chao, M. Li, S. Wu and S. Dong, *Chem. Sci.*, 2022, **13**, 4566–4572.

260 A. J. Espay, F. Morgante, A. Merola, A. Fasano, L. Marsili, S. H. Fox, E. Bezard, B. Picconi, P. Calabresi and A. E. Lang, *Ann. Neurol.*, 2018, **84**, 797–811.

261 W. Liang, M. Gao, Y. Li, Y. Tong and B.-C. Ye, *Talanta*, 2021, **225**, 122042.

262 L. Q. Liu, F. F. Li, T. T. Liu, S. H. Chen and M. X. Zhang, *J. Electroanal. Chem.*, 2022, **921**, 116701.

263 X. F. Cai, F. Ma, J. Jiang, X. L. Yang, Z. W. Zhang, Z. L. Jian, M. J. Liang, P. W. Li and L. Yu, *J. Hazard. Mater.*, 2023, **441**, 129853.

264 H. Ouyang, J. Xian, J. Gao, L. Zhang, W. Wang and Z. Fu, *Anal. Chem.*, 2022, **94**, 3400–3407.

265 H. Ouyang, L. Zhang, S. Jiang, W. Wang, C. Zhu and Z. Fu, *Chem Eur. J.*, 2020, **26**, 7583–7588.

266 X. Niu, Q. Shi, W. Zhu, D. Liu, H. Tian, S. Fu, N. Cheng, S. Li, J. N. Smith, D. Du and Y. Lin, *Biosens. Bioelectron.*, 2019, **142**, 111495.

267 D. Zhang, Q. Han, W. Liu, K. Xu, M. Shao, Y. Li, P. Du, Z. Zhang, B. Liu, L. Zhang and X. Lu, *ACS Appl. Nano Mater.*, 2022, **5**, 1958–1965.

268 Y. Wu, L. Jiao, X. Luo, W. Xu, X. Wei, H. Wang, H. Yan, W. Gu, B. Z. Xu, D. Du, Y. Lin and C. Zhu, *Small*, 2019, **15**, 1903108.

269 M. Wang, L. Liu, X. Xie, X. Zhou, Z. Lin and X. Su, *Sens. Actuators, B*, 2020, **313**, 128023.

270 Q. Chen, S. Li, Y. Liu, X. Zhang, Y. Tang, H. Chai and Y. Huang, *Sens. Actuators, B*, 2020, **305**, 127511.

271 X. Xie, Y. Wang, X. Zhou, J. Chen, M. Wang and X. Su, *Analyst*, 2021, **146**, 896–903.

272 S. Li, D. Liu, B. Wu, H. Sun, X. Liu, H. Zhang, N. Ding and L. Wu, *Talanta*, 2022, **239**, 123088.

273 Y. Chen, L. Jiao, H. Yan, W. Xu, Y. Wu, L. Zheng, W. Gu and C. Zhu, *Anal. Chem.*, 2021, **93**, 12353–12359.

274 W. Xu, W. Song, Y. Kang, L. Jiao, Y. Wu, Y. Chen, X. Cai, L. Zheng, W. Gu and C. Zhu, *Anal. Chem.*, 2021, **93**, 12758–12766.

275 Z. Wu, C. Wang, Z. Luo, Y. Qin, X. Wang, J. Wen, L. Hu, W. Gu and C. Zhu, *Anal. Chem.*, 2022, **94**, 6866–6873.

276 W. Gu, X. Wang, M. Xi, X. Wei, L. Jiao, Y. Qin, J. Huang, X. Cui, L. Zheng, L. Hu and C. Zhu, *Anal. Chem.*, 2022, **94**, 9459–9465.

277 R. Zeng, W. Wang, G. Cai, Z. Huang, J. Tao, D. Tang and C. Zhu, *Nano Energy*, 2020, **74**, 104931.

278 L. Sun, C. Li, Y. Yan, Y. Yu, H. Zhao, Z. Zhou, F. Wang and Y. Feng, *Anal. Chim. Acta*, 2021, **1180**, 338856.

279 Y. X. Nie, P. L. Wang, Q. Ma and X. G. Su, *Anal. Chem.*, 2022, **94**, 11016–11022.

280 O. S. Kotsiou and K. I. Gourgoulianis, *Ann. Allergy, Asthma, Immunol.*, 2018, **120**, 340.

281 J. Li, J. Xie, L. Gao and C. M. Li, *ACS Appl. Mater. Interfaces*, 2015, **7**, 2726–2734.

282 W. Zhou, Y. Tan, J. Ma, X. Wang, L. Yang, Z. Li, C. C. Liu, H. Wu, L. Sun and W. Q. Deng, *ACS Sens.*, 2022, **7**, 3422–3429.

283 Y. C. Ma, Y. Zhang, J. Q. Gao, H. Ouyang, Y. He and Z. F. Fu, *Anal. Chem.*, 2022, **94**, 14047–14053.

284 J. Jiang, Q. Cai and M. Deng, *Front. Chem.*, 2022, **9**, 812983.